THEORETICAL AND EXPERIMENTAL INVESTIGATION OF BULK GLASS FORMING ABILITY IN BULK AMORPHOUS ALLOY SYSTEMS

A THESIS SUBMITTED TO
THE GRADUATE SCHOOL OF NATURAL AND APPLIED SCIENCES
OF
MIDDLE EAST TECHNICAL UNIVERSITY

BY

CAN AYAS

IN PARTIAL FULFILLMENT OF THE REQUIREMENTS
FOR
THE DEGREE OF MASTER OF SCIENCE
IN
METALLURGICAL AND MATERIALS ENGINEERING

JANUARY 2005

Approval of the Graduate School of Natural and Applied Science

_____

Prof. Dr. Canan Özgen

Director

I certify that this thesis satisfies all the requirements as a thesis for the degree of Master of Science.

_____

Prof. Dr. Tayfur Öztürk

Head of Department

This is to certify that we have read this thesis and that in our opinion it is fully adequate, in scope and quality, as a thesis for the degree of Master of Science.

Prof. Dr. Vedat Akdeniz	Prof. Dr. Amdulla O. Mekhrabov
Co-Supervisor	Supervisor

Examining Committee Members

Prof. Dr. Şakir Erkoç	(METU, PHYS) _____
Prof. Dr. Amdulla O. Mekhrabov	(METU, METE) _____
Prof. Dr. Vedat Akdeniz	(METU, METE) _____
Prof. Dr. Macit Özenbaş	(METU, METE) _____
Assoc. Prof. Dr. C. Hakan Gür	(METU, METE) _____

I hereby declare that all information in this document has been obtained and presented in accordance with academic rules and ethical conduct. I also declare that, as required by these rules and conduct, I have fully cited and referenced all material and results that are not original to this work.

Name, Surname: Can Ayas

Signature :

ABSTRACT

THEORETICAL AND EXPERIMENTAL INVESTIGATION OF BULK GLASS FORMING ABILITY IN BULK AMORPHOUS ALLOY SYSTEMS

Ayas, Can

M.S., Department of Metallurgical and Materials Engineering

Supervisor: Prof. Dr. Amdulla Mekhrabov

Co-Supervisor: Prof. Dr. Vedat Akdeniz

January 2005, 154 pages

In this study molecular dynamics simulation program in NVT ensemble using Velocity Verlet integration was written in order to investigate the glass forming ability of two metallic systems. The Zn-Mg system, one of the frontiers of simple metal-metal metallic glasses and Fe-B, inquiring attention due to presence of many bulk glass forming alloy systems evolved from this binary with different alloying element additions.

In addition to this, atomistic calculations on the basis of ordering were carried out for both Zn-Mg and Fe-B systems. Ordering energy values are calculated using electronic theory of alloys in pseudopotential approximation and elements which increase the ordering energy between atoms were determined. The elements which increase the ordering energy most were selected as candidate elements in order to design bulk amorphous alloy systems.

In the experimental branch of the study centrifugal casting experiments were done in order to see the validity of atomistic calculations. Industrial low grade ferroboron was used as the master alloy and pure element additions were performed in order to constitute selected compositions. $Fe_{62}B_{21}Mo_5W_2Zr_6$ alloy was successfully vitrified in bulk form using nearly conventional centrifugal casting processing. Specimens produced were characterized using SEM, XRD, and DSC in order to detect the amorphous structure and also the crystalline counterpart of the structure when the cooling rate is lower. Sequential peritectic and eutectic reaction pattern was found to be important for metallic glasses which can be vitrified in bulk forms with nearly conventional solidification methods.

Keywords: Fe based alloys, Zn based alloys, Glass Forming Ability, Metallic Glasses, Molecular Dynamics, Ordering, Centrifugal Casting

ÖZ

İRİ HACİMLİ METALİK CAMLARDA CAM OLUŞTURMA YETENEĞİNİN TEORİK VE DENEYSEL YÖNTEMLERLE İNCELENMESİ

Ayas, Can

Yüksek Lisans, Metalurji ve Malzeme Mühendisliği Bölümü
Tez Yöneticisi: Prof. Dr. Amdulla Mekhrabov
Ortak Tez Yöneticisi: Prof. Dr. Vedat Akdeniz
Ocak 2005, 154 sayfa

Bu çalışmada Zn-Mg be Fe-B metalik alaşımlarında bu sistemlerin cam oluşturma yeteneğini incelemek için NVT bileşiminde Velocity Verlet integrali kullanılarak moleküler dinamik simulasyonu programı yazılmıştır. Zn-Mg alaşımı metal-metal olarak üretilmiş ilk amorf alaşımlardan biri olduğu için çalışmaya dahil edilirken, Fe-B sistemi ise değişik alaşım elementleri eklenmesiyle birçok iri ve hacimli metalik cam alaşımı oluşturması nedeniyle incelenmiştir.

Çalışma kapsamında ayrıca atomistik yaklaşım kullanılarak atomsal düzenlenme Zn-Mg ve Fe-B sistemleri için incelenmiştir. Atomlar arası düzenlenme enerjileri alaşımların elektronik teorisinin pseudopotansiyel yaklaşımında kullanılmasıyla hesaplanmıştır. Belirtilen sistemlerde atomlar arası düzenlenme enerjisini en çok arttıran elementler, iri hacimli amorf alaşımlar tasarlamak için aday elementler olarak tayin edilmiştir.

Çalışmanın deneysel kısmında atomistik hesaplamalarının geçerliliğini saptama amacıyla santrifüjlü döküm deneyleri yapılmıştır. Alaşım hazırlama safhasında endüstriyel ferrobor ve saf elementler kullanılarak seçilen kompozisyonlar oluşturulmuştur. $Fe_{62}B_{21}Mo_5W_2Zr_6$ alaşımı konvansiyonel benzereri döküm yöntemiyle iri ve hacimli olarak amorf yapıda başarıyla üretilmiştir. Üretilen alaşımlar, taramalı elektron mikroskobu, x-ışınları kırınımı ve thermal analiz yöntemleriyle karakterize edilmiş ve amorf faz oluşumu tespit edilmiştir. Ayrıca alaşımların daha yavaş soğuma hızlarında oluşturdukları kristal yapılarda incelenmiştir. Ardışık peritektik ve ötektik reaksiyonların iri ve hacimli cam oluşturma kabiliyeti açısından önemli olduğu saptanmıştır.

Anahtar Kelimeler: Fe bazlı alaşımlar, Zn bazlı alaşımlar, Metalik Cam, Cam Oluşturma Yeteneği, Moleküler Dinamik, Atomlar arası düzenlenme, Satrifüjlü Döküm.

ACKNOWLEDGMENTS

I express my deepest gratitude to my supervisor Prof. Dr. Amdulla Mekhrabov and Prof. Dr. Vedat Akdeniz for their guidance, criticism, encouragements, patience and insight throughout the research.

I am deeply grateful to my family for their love, encouragement and endless belief on me through out my life.

I express my thanks to my lab friends Ali Abdelal, Hülya Arslan, Emrah Erdiller, Selen Gürbüz and İlkay Saltoğlu for their various help and critics throughout the study. I would also like to express my gratitude to my friend Fatih Şen for the valuable discussions.

Special thanks to Nigel Robinson for reviewing the manuscripts, and to Ahmet Peynircioğlu for his precious accompany in endless night shifts.

I would like to express my thanks to Cem Taşan for keeping me in the track and always being at next door to share his synergy.

I am deeply indebted to Özlem Esma Güngör not only for her various help and critics but more importantly for touching my soul from the deepest and illuminating inspiration in every second we share.

This study was supported by the Scientific Research Projects Fund of Graduate School of Engineering, Grant No: BAP-2003-07-02-00-57.

TABLE OF CONTENTS

LIST OF TABLES

LIST OF FIGURES

LIST OF SYMBOLS

T_g	Glass Transition Temperature
T_x	Crystallization Temperature
σ_y	Yield Strength
E	Young's Modulus
ΔT_x	Supercooled Liquid Region
η	Viscosity
C_p	Heat Capacity
R_c	Critical Cooling Rate
T_{rg}	Reduced Glass Transition Temperature
T_l	Liquidus Temperature
T_m	Solidus Temperature
ΔG	Gibbs Free Energy of Crystallization
ΔH	Enthalpy of Fusion
ΔS	Entropy of Fusion
ΔT_r	Reduced Undercooling
I_v	Homogenous Nucleation Frequency
k_n	Kinetic Constant
$\eta(T)$	Temperature Dependent Shear Viscosity

$\mathbf{T_r}$	Reduced Temperature
$\boldsymbol{\alpha}$	Dimensionless Parameter Related to Liquid/Crystal Interfacial Energy
$\boldsymbol{\beta}$	Dimensionless Parameter Related to Molar Entropy of Fusion
$\boldsymbol{\sigma}$	Molar Entropy of Fusion
$\mathbf{N}$	Avogadro Number
$\mathbf{V}$	Molar Volume of the Crystal
$\mathbf{R}$	Gas Constant
$\boldsymbol{\gamma}$	γ Criteria For GFA
$\boldsymbol{\Sigma_{str}}$	Total Crystal Energy
$\mathbf{U_0}$	Volume Dependent Electronic Contribution to Total Energy
$\mathbf{U_{bs}}$	Structure Dependent Electronic Contribution to Total Energy
$\mathbf{U_{lattice}}$	Coulomb Repulsion Between The Ion Cores
$\mathbf{g_n}$	Reciprocal Lattice Vector
$\mathbf{q}$	Ordinary Position Vector
$\mathbf{k}$	Wave Vector
$\boldsymbol{\Omega}$	Volume of the Crystal
$\kappa\left(\vec{q}\right)$	Lindhard's Function
ξ	Ewald Parameter
$\mathbf{V_{cr}(q)}$	Crystal Potential
$\boldsymbol{\omega_{ij}}$	Ordering Energy

$\mathbf{W_i^0\ (q)}$	Form Factor of an Unscreened Pseudopotential of i ions
$\mathbf{F_{\alpha\beta}(q)}$	Characteristic Function of Partial Ordering Energy
$\mathbf{S(q)}$	Structure Factor
$\mathbf{L(q,q_k)}$	Lagrangian Function
$\mathbf{H(r_i,p_i)}$	Hamiltonian Function
$\mathbf{m_i}$	Mass of Particle i
$\mathbf{r_i}$	Position of Particle i
$\mathbf{p_i}$	Momentum of Particle i
$\mathbf{v_i}$	Velocity of Particle i
$\mathbf{a_i}$	Acceleration of Particle i
$\mathbf{k_b}$	Boltzman Constant
$\mathbf{U}$	Total Potential Energy of a System
$\mathbf{\Delta t}$	Time Step
$\mathbf{\beta}$	Rescaling Factor
$\mathbf{\varepsilon_{(q)}}$	Dielectric Constant
$\mathbf{\alpha}$	Dimensionless Entropy
$\mathbf{H_v}$	Vickers Hardness

CHAPTER I

INTRODUCTION

Metallic glasses are amorphous metallic alloys with no long range order in the distribution of atoms. Non-crystalline atomic configuration of metallic glasses may arise from the non-equilibrium solidification of metallic melt. Upon rapid solidification disordered atomic positions of the liquid are frozen while the equilibrium reactions namely nucleation and growth of the crystals are at least partially inhibited.

Metallic glasses can be formed by various different routes, such as solidification from the liquid or vapor phases, deposition from a chemical solution or an electrolyte and by high energy ion or neutron bombardment of crystalline materials [1]. Mechanically alloying and severe deformation techniques have also become an important production method for metallic glasses. However at present rapid solidification techniques turn out to be the major production technique in which intensive research is being conducted.

The technological importance of metallic glasses arises from the unique properties due to the disordered structure. There are unique magnetic, mechanical, electrical and corrosion behaviors which result from this amorphous structure. For example, they can show soft magnetic characteristics, they are exceptionally hard and have extremely high tensile strengths and in some alloys the coefficient of thermal expansion can be made zero; they may also have electrical resistivities which are three to four times higher than those of conventional iron or iron-nickel alloys; and finally some of the amorphous alloys are exceptionally corrosion resistant [1].

Metallic glasses although having very promising physical properties, haven't yet gained the wide commercial interest which they deserve. This arises from the sophisticated techniques needed for their production. High quenching rates adequate for vitrification impose geometrical constraints on the dimensions of the samples produced. At least one dimension of the sample should not exceed a critical value in order to remove heat rapidly upon cooling in limited time which allows limited diffusion.

Glass forming ability (GFA) is the term used to specify the ease of glass formation upon cooling form the melt. In this manner metallic systems have rather poor glass forming abilities relative to oxide glasses.

The driving force for the development of this subject mostly became minimizing the critical cooling rate and maximizing the sample thicknesses glass forming metallic systems. With this criterion it is aimed to discover alloys systems with high GFA, which can vitrify with nearly conventional casting methods. Recently new amorphous multi-component alloys with much lower critical cooling rates ranging from 0.100 K/s to several hundreds K/s have been explored. Simultaneously, the maximum sample thickness for glass formation (t_{max}) increases drastically from several millimeters to about one hundred millimeters. It is to be noticed that the lowest R_c and largest t_{max} are almost comparable to those for ordinary oxide glasses. Amorphous alloys with sizes greater than millimeter scale are called bulk amorphous alloys or bulk metallic glasses (BMG). In addition, current bulk amorphous alloy systems are multi component with the number of constituents four or higher and usually availability and cost of at least one component becomes a reason for hindering the wide commercialization of the products.

Another scope of the active research on the subject is discovering the fundamental physical parameters underlying the high glass formation of some

alloy systems. Semi-empirical criteria for high glass forming ability is proposed by Inoue, however more general and theoretical rules should be established for glass forming ability. Structural and thermal properties of metallic glasses are also very important to develop theories of glass formation. Experimental techniques to gain insight into glassy structure are employed widely such as high resolution microscopy, diffraction techniques and thermal analysis. Besides the huge experimental work reported in literature; computer simulations are also conducted for this purpose. With the development of more powerful computers, simulation studies up to several thousand atoms can now be run. Computer simulation emerged as a new tool to design and develop new bulk amorphous alloys with the light of condensed state physics and computational material science. With the advancement of this research tool, computer simulations can replace more expensive and time consuming traditional trial and error methods to explore new bulk amorphous alloy systems.

The aim of this thesis is to design new bulk amorphous alloy compositions for Zn-Mg and Fe-B systems by utilizing theoretical calculations, writing a general molecular dynamics code for simulation studies of binary and ternary alloy systems, simulating the amorphous phase formation and evaluation of GFA. In the experimental part of the study it is aimed to synthesize bulk amorphous alloys in Fe-B system by centrifugal casting according to the predictions made.

The literature survey of the subject and theory of glass formation is explained in chapter two. In chapter three basics of pseudopotential theory and molecular dynamics which forms the methodology of the simulation work is explained. In chapter four theoretical calculations, simulations and casting experiments carried out are given. Results obtained are given and discussed in chapter five, and conclusions drawn are given in chapter six.

CHAPTER II

LITERATURE SURVEY

2.1 DESCRIPTION OF METALLIC GLASSES

The amorphous phase may form within some metallic/intermetallic alloys during solidification, where the cooling rates are high enough to suppress crystallization in the melt and therefore at a critical temperature (glass transition temperature, T_g) the liquid like structure of the melt is frozen into the solid state without gaining the long range symmetry of the crystal. Although long range order is absent there is experimental evidence that short range order exists in amorphous metallic alloys [2]. Upon annealing in an amorphous phase, it is known that crystal nuclei start to form and grow at a temperature which is called the crystallization temperature (T_x). The temperature gap between the T_x and T_g is defined as the supercooled liquid region, which is an indicator of the stability of the amorphous phase to crystallization.

2.2 HISTORICAL DEVELOPMENT OF METALLIC GLASSES

Metallic glasses and practical methods for processing these materials have been developed over the past four decades. Historically, the first report in which a range of amorphous metallic alloys were claimed to have been made was by Kramer [3]. This was based on vapor deposition. Somewhat later Brenner et al. [4] claimed to have made amorphous metallic alloys by electrodepositing nickel-phosphorus alloys. They observed only one broad diffuse peak in the X-ray scattering pattern in non-magnetic high phosphorus alloys. Such alloys have been in use for many years as hard, wear and corrosion resistant coatings [1].

It was 1960 when Pol Duwez [5] at the California Institute of Technology produced the first ribbons of metallic glasses, which had unusual mechanical strength, magnetic behavior, and resistance to wear and corrosion that set them apart from conventional crystalline materials. The processing method involved chilling molten metal at rates in excess of 1,000,000 C^0 per second, which was called splat quenching. The first alloy system vitrified was a binary gold silicon alloy.

Almost simultaneously Miroshnichenko and Salli [6] in the USSR reported on a similar device for preparing amorphous alloys. In this technique the liquid alloy drop is propelled on to a cold surface where it spreads into a thin film and is thus rapidly solidified. Duwez actually propelled the liquid drop, whereas Miroshnichenko and Salli propelled the two opposing pistons together with the drop in between [1].

Production of a continuous long-length of ribbon was first reported by Pond and Maddin [7]. This opened a new era in the subject, as the possibility of large scale production has opened up and the interest of the scientific community is increased on metallic glasses [1].

At the same time, Chen and Turnbull [8] were able to make amorphous spheres of ternary Pd-Si-X with X= Ag, Cu, or Au. The alloy $Pd_{77.5}Cu_6Si_{16.5}$ could be made glassy and with the diameter of 0.5 mm and existence of glass transition was demonstrated [9]. Chen [10] also made investigations about the formation and stability of $(Pd_{1-x}M_x)_{0.835}Si_{0.165}$, $(Pd_{1-x}T_x)_{1-xp}P_{xp}$ and $(Pt_{1-x}Ni_x)_{1-xp}P_{xp}$, compositions. Here T = Ni, Co, Fe and M = Rh, Au, Ag, Cu. It was able to attain 1 mm as the critical casting size [11].

In the beginning of the 1980's Turnbull et al. [12] studied on the Pd-Ni-P system which is the first system vitrified in bulk form. Glassy ingots of $Pd_{40}Ni_{40}P_{20}$ are

produced with a diameter of 5mm. Turnbull further increased the thickness of the ingot to 1 cm by eliminating the heterogeneous nucleation sites by flux treatment of boron oxide.

During the late 1990's Inoue group investigated the use of rare-earth materials with Al and ferrous metals. While studying rapid solidification in this system, they found exceptional glass forming ability in La-AL-Ni and La-Al-Cu alloys [13]. Cylindrical samples with diameters up to 5 mm or sheets with similar thicknesses were made fully amorphous by casting $La_{55}Al_{25}Ni_{20}$ (or later $La_{55}Al_{25}Ni_{10}Cu_{10}$ up to 9 mm) into copper molds.

In 1991 the same group developed glassy Mg-Cu-Y and Mg-Ni-Y alloys with the largest glass forming ability obtained in $Mg_{65}Cu_{25}Y_{10}$ [14]. At the same time Inoue group developed a family of Zr based Zr-Al-Ni-Cu alloys having a high glass forming ability and thermal stability against crystallization [15]. The critical casting thickness in these alloys ranged up to 155 mm and the supercooled region was extended to 127 K^0 for alloy $Zr_{65}Al_{7.5}Ni_{10}Cu_{17.5}$ [9].

With the significant success achieved by Inoue group, bulk amorphous alloys became a popular research area. Johnson developed new compositions that could be processed without rapid cooling in bulk or three-dimensional form (bulk forms are more than 20 times thicker than the roughly 40-micrometer ribbons), suitable for casting or possibly molding into complex shapes for precision parts, without the costs or wastes associated with machining. $Zr_{41.2}Ti_{13.8}Cu_{12.5}Ni_{10}Be_{22.5}$ has been developed by Peker and Johnson [16] and named as Vitreloy 1.

Typical bulk amorphous alloys explored in the 1990's are tabulated with the calendar years by Inoue and is given in Table 2.1 below:

Table 2.1 Typical bulk glassy alloy systems reported together with the calendar years when the first paper or patent of each alloy system was published [17].

1.Nonferrous alloy systems	
Mg-Ln-M (Ln= lanthanide metal M= Ni Cu Zn)	1988
Ln-Al-TM TM= VI-VIII group transition metal	1989
La-Ga-TM	1989
Zr-Al-TM	1990
Ti-Zr-TM	1993
Zr-Ti-TM-Be	1993
Zr-(Ti,Nb,Pd)-Al-TM	1995
Pd-Cu-Ni-P	1996
Pd-Ni-Fe-P	1996
Pd-Cu-B-Si	1997
Ti-Ni-Cu-Sn	1998
Cu-(Zr,Hf)-Ti	2001
2. Ferrous alloy systems	
Fe-(Al-Ga)-(P,C,B,Si,Ge)	1995
Fe-(Nb,Mo)-(Al,Ga)-(P,B,Si)	1995
Co-(Al,Ga)-(P,B,Si)	1996
Fe-(Zr,Hf,Nb)-B	1996
Co-(Zr,Hf,Nb)-B	1996
Ni-(Zr,Hf,Nb)-B	1996
Fe-Co-Ln-B	1998
Fe-(Nb,Cr,Mo)-(C,B)	1999
Ni-(Nb,Cr,Mo)-(P,B)	1999
Co-Ta-B	1999
Fe-Ga-(P,B)	2000
Ni-Zr-Ti-Sn-Si	2001

In order to visualize the rapid development in finding alloy systems with high glass forming ability, the casting thickness of several important amorphous alloys are given together with their date of discovery in Figure 2.1

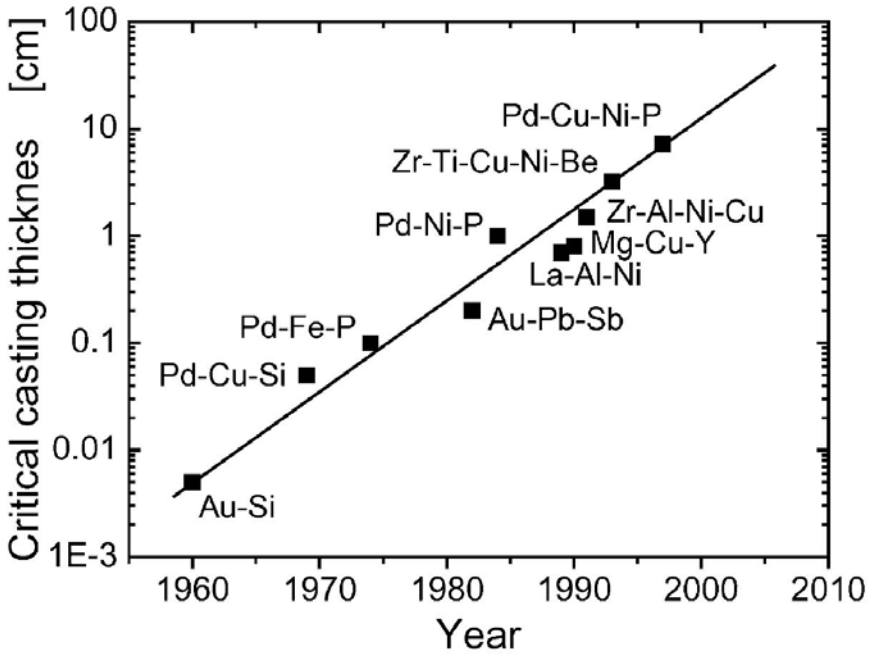

Figure 2.1 Critical casting thickness of conventional glasses, for glass formation as a function of the year corresponding alloy has been discovered [9].

2.3 AMORPHOUS NANOCRYSTALLINE MATERIALS

BMGs also attracted attention as precursors to produce nanophase composites, which render even better properties than monolithic metallic glasses. By applying appropriate thermal treatment, controlled crystallization is attained. The amorphous alloys crystallize into nanometer-sized crystallites (or quasicrystallites) embedded in an amorphous matrix [18].

During devitrification, stability of the remaining amorphous phase can be further increased; if solute enrichment is observed at crystallization, by segregation of solute element with low atomic diffusivity at the nanocrystal/amorphous interface. Segregation also suppresses the growth reaction of nanocrystals. The

final nanostructure is strongly dependent on the number of homogeneous nucleation sites in the as-quenched glass. However, it has also been suggested a possible control of heterogeneous nucleation mechanism by additional elements occurring by formation of clusters or by the presence of quenched in nuclei. [18] In addition to these, Inoue [19] also proposed that multistage crystallization is also crucial for the formation of amorphous nanocrystalline materials.

2.4 PROPERTIES AND APPLICATIONS OF METALLIC GLASSES

The superior properties of metallic glasses arise from the absence of crystallanity in the microstructure. In an amorphous microstructure, crystalline defects cannot be present because of the nature of the amorphous state. The absence of dislocations and grain boundaries renders different mechanical and magnetic properties due to different mechanisms compared with the crystalline counterparts of the amorphous alloys. Grain boundaries are the weak spots with less atomic packing, where fractures can form corrosion starts. Misaligned planes of atoms under sufficient stress and heat slip over each other easily, allowing dislocations to move. As a result crystalline materials have a much lower strength than their theoretical values [20].

Lack of grain boundaries is also one of the factors that make some amorphous alloys more resistant towards corrosion; grain boundaries allow the diffusion of oxygen due to their open structure. Another factor is that the amorphous phase in many alloys is stabilized by B, P or Si. These elements are strong oxide formers and may be the source for passivation in the same way as chromium in stainless steel provides a protective layer against corrosion for the iron.

Pang and coworkers [21] experimentally verified that $Fe_{43}Cr_{16}Mo_{16}C_{15}B_{10}$ and $Fe_{43}Cr_{16}Mo_{16}C_{10}B_5P_{10}$ bulk glassy alloys exhibit passive behavior within extremely corrosive environments, indicating that they have high corrosion resistance. Corrosion resistance is higher for phosphorus containing alloys.

Atomic disorder is also the reason for high electrical resistance of amorphous alloys, which is useful for suppressing eddy currents in high frequency magnetic reversal applications [22].

2.4.1 Mechanical Properties

The mechanical properties of metallic glasses are in many cases superior to their crystalline counterparts. In tensile loading, the elastic strain limit of metallic glasses, ε_l, is 2% higher than that of common crystalline metallic alloys where ε_l can reach 41%. Thus, the yield strength of amorphous alloys is relatively high in tension and compression. In Vitreloy1 [9] ($Zr_{41.2}Ti_{13.8}Cu_{12.5}Ni_{10}Be_{22.5}$), for example, the tensile yield strength, σ_y is 1.9 GPa and Young's modulus E, is 96 GPa. Upon yielding, metallic glasses often show plastic flow in absence of work-hardening and a tendency towards work-softening leads to shear localization. Under tensile conditions, the localization of plastic flow into shear bands limits dramatically the overall plasticity, so that metallic glass specimens usually fail catastrophically on one dominant shear band. This adverse property was recently mitigated by the development of composites containing ductile crystals in a bulk metallic glass matrix. Nanocomposites with improved plasticity ranging up to 2.5% in compression was obtained by the annealing of glassy precursor alloys in the vicinity of T_x to allow some limited crystallization.

In another approach, researchers obtained a reinforced composite consisting of ductile micrometer sized crystals in a glassy matrix via in situ processing, i.e., without additional annealing steps. The production of a composition in the

neighborhood of Vit1 ($Zr_{56.2}Ti_{13.8}Nb_5Cu_7Ni_{5.5}Be_{12.5}$) led to the precipitation of a high-temperature, micrometer-sized β-ZrTi (bcc) phase upon cooling, which shifted the composition of the remaining liquid close to that of Vitrealoy1. As a consequence the remaining liquid solidified as a bulk metallic glass. The element Nb was added to stabilize the ductile bcc phase over the β-ZrTi (hcp) phase. The resulting two-phase microstructure effectively modifies shear band formation and propagation. A high density of multiple shear bands evolves upon loading, which results in a significant increase of ductility both in tension and compression, toughness, and impact resistance compared to the monolithic glass. The overall (tensile and compressive) plastic strain of this in situ composite is about 5%. The tensile ductility is of particular importance for the use of bulk metallic glasses as structural engineering materials [9].

2.4.2 Magnetic Properties

The unique properties of amorphous alloys stem from the lack of long-range atomic order. The alloys do not exhibit magnetocrystalline anisotropy, thus some of the alloys are extremely magnetically soft. The absence of grain boundaries, which could otherwise pin the domain walls, also contributes to a low coercivity [22].

Based on the three empirical rules for achievement of high glass forming ability new bulk amorphous alloys with ferromagnetism at room temperature have been developed. Soft ferromagnetic bulk amorphous alloys have been synthesized in multicomponent Fe-(Al,Ga)-(P,C,B,Si), Co-Cr-(Al-Ga)-(P,B,C), Fe-(Co,Ni)-(Zr,Nb,Ta)-B, and Co-Fe-(Zr,Nb,Ta,)-B systems [23].

2.4.3 Applications of Metallic Glasses

Metallic Glasses with promising properties can have a wide range of technological applications. The combination of high strength, elasticity, hardness and wear resistance has opened markets in a diverse spectrum of products. Particularly important application fields are machinery/structural materials, magnetic materials, acoustic materials, somatologic materials, optical machinery materials, sporting good materials and electrode materials. Zr-Al-Ni-Cu and Zr-Ti-Al-Ni-Cu alloys have already been commercialized as golf club materials [24]. Cell phone cases, surgical instruments, implants for bone replacement and other medical devices are other application areas [9].

2.5 METHODS OTHER THAN RAPID SOLIDIFICATION FOR THE PRODUCTION OF METALLIC GLASSES

The production of bulk amorphous alloys by consolidation of amorphous powders has promising and important practical applications in the near-net-shape fabrication of components. This flexible processing method substantially eases the limitations in sample shape and size. The properties of the consolidated amorphous product depend on the density and the bonding state that exists between the powder particles, as well as the strength and ductility of the alloy.

The fabrication of bulk amorphous alloys with high strength by a warm extrusion method requires full densification by flow under high pressure at temperatures that are below the crystallization temperature (T_x), yet above the glass transition temperature (T_g). Moreover, strong bonding between the powder particles should occur by breaking of the surface films (e.g., oxide or nitride) during deformation of the powders. These conditions imply that the amorphous alloy should have a wide super-cooled liquid region ($\Delta T_x = T_x - T_g$) and high glass forming ability for full densification without crystallization during extrusion [25].

In the supercooled liquid state, a metallic glass can be deformed under Newtonian flow, where the viscosity is independent of the strain rate. At higher strain rates, viscosity tends to decrease linearly and the deformation mode changes from a homogeneous mode, where all volume elements contribute to total strain, to an inhomogeneous mode, where strain is localized and deformation occurs in thin, discrete shear bands. In the inhomogeneous mode, plastic flow in the shear bands is high, but its contribution to global plasticity is very small. By maintaining appropriate strain rates and thermal conditions, bulk metallic glasses may be homogeneously deformed in their supercooled liquid state by conventional plastic forming techniques such as warm extrusion and compression molding. Sordelet et al. [25] examined the warm extrusion behavior and devitrification tendencies of gas atomized $Cu_{47}Ti_{34}Zr_{11}Ni_8$ powders in their supercooled liquid state. Amorphous powders are produced by gas atomization, where the cooling rate can be very high for small atomized drops. Several warm extrusion experiments have been conducted and successful consolidations predominantly to amorphous alloys are reported [26].

Lee et al. [26] also reported, a fully amorphous $Ni_{59}Zr_{20}Ti_{16}Si_2Sn_3$ alloy successfully synthesized by warm extrusion. The extrusion temperature of 848 K was selected from the T–T–T curve for the onset of crystallization of the amorphous powders. The Ni based amorphous alloy exhibited high strength about 2 GPa, whereas the as cast $Ni_{59}Zr_{20}Ti_{16}Si_2Sn_3$ alloy has a strength of 2.2 GPa.

Another route for forming amorphous powders is mechanical alloying, where solid state amorphitization from the crystal powders is attained by ball milling. Transition from crystalline to amorphous phase is observed when a sufficiently high energy level is reached and kinetic conditions prevent the establishment of equilibrium [27, 28].

2.6 THEORY OF METALLIC GLASS FORMATION

2.6.1 Glass Forming Ability

Liquid state is characterized by the absence of long-range order. When a metal or alloy melts, the three dimensional lattice arrangements of atoms are destroyed, and in the liquid the atoms vibrate about positions that are constantly and rapidly interdiffusing. During melting, the crystal and liquid phases are in equilibrium and for pure metals, the volume, enthalpy, and entropy undergo discontinuous change; the enthalpy and entropy increase, the volume usually does also, except where the atomic packing in the crystal is relatively open, as for semimetals. Melting is therefore a first order phase transformation [29].

A liquid, at temperatures above the melting point, is in a state of internal equilibrium and its structures and properties are independent of its thermal history. It is characterized by the inability to resist shear stress [29]. On cooling, for the solidification phase transformation to occur liquid must undercool below the equilibrium crystallization temperature, due to an energy barrier to the formation of nuclei. The degree of undercooling that occurs depends upon several factors, including the initial viscosity of the liquid, the rate at which the viscosity increases with decreasing temperature, the temperature dependence of the free energy difference between the undercooled liquid and crystal phase, the interfacial energy between the melt and crystal, the volume density and the efficiency of heterogeneous nucleating particles and the imposed cooling rate. Liquid transition metals such as iron, nickel and cobalt, in which the heterogeneous nucleants have been largely removed with a flux, can be undercooled in bulk by more than 200 K under slow cooling conditions. However, the growth rates for crystals in metallic melts are very rapid once nucleated and where the rate of heat removal to the surroundings is small, rapid recalescence occurs [29].

For the formation of an amorphous phase by rapid solidification of the melt, suppression of the nucleation and growth crystalline phases in the supercooled region is required.

If a liquid metal is rapidly cooled below its melting temperature, the influence of heterogeneous nucleants is increasingly delayed with the decrease of atomic mobility, and as the cooling rate is increased, the undercooling is increased and the recalecense decreased. Thus the temperature range over which crystallization proceeds becomes increasingly depressed, leading to structural modifications [1]. The structure of alloys rapidly quenched from liquid state is always unusual in some respect, even if the phases present are crystallographically the same as in the equilibrium alloys. For example, binary alloys in which a complete series of solid solutions exists, can be obtained with the highest degree of homogeneity. With rapid cooling the refinement of microstructural features occur. Quenching from liquid state also results in high concentration defects; the technique has been used to study vacancy concentrations in quenched aluminum. However, the most interesting application of the technique is by far, the synthesis of new alloy phases which cannot be obtained neither under equilibrium conditions nor by quenching from the solid state. These new phases can be classified into three types; solid solutions extending beyond the equilibrium concentrations, metastable crystalline phases and amorphous phases [30]. Amorphous phase is formed when the cooling rate is sufficiently high, to suppress crystallization because of insignificant growth or in the extreme nucleation. In this case, shear viscosity (η) decreases continuously while in crystallization there is a discontinuous jump in the viscosity value. The dependence of η to temperature can be seen in Fig. 2.2.

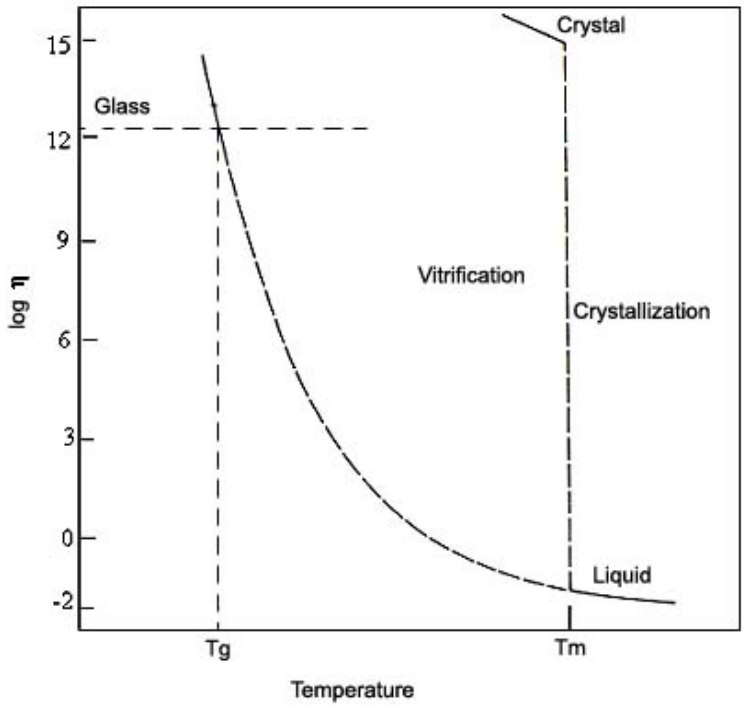

Figure 2.2 Change in the viscosity of a material upon crystallization and amorphous phase formation [29].

Although the driving force for nucleation is continually increasing, this is opposed by rapidly decreasing mobility which at very high undercoolings, dominates. Eventually, the atomic configuration of the liquid departs from equilibrium and then shortly thereafter becomes homogeneously frozen, at the so called glass transition temperature. This structural freezing to the glass state is by convention, considered to occur when η is about 10^{13} poise [29].

Glass transition is characterized by significant loss of modulus and volume upon heating. Glass transition is not one temperature but a relatively narrow range (10 degrees). Tg is not precisely measured, but is a very important characteristic. Glass transition is a second order transformation which means at Tg the

temperature dependence of the volume and enthalpy decreases discontinuously, Cp value decreases significantly due to the freezing of the structure. The difference between the Cp values of crystal and vitrified liquid diminishes.

Glass formation occurs easily in some familiar cases of non-metallic materials such as silicate glasses. In these the nature of atomic bonding severely limits the capability of atomic or molecular rearrangement necessary for maintaining thermodynamic equilibrium upon cooling. Thus the melt solidifies to a glass, even at low rates of cooling, often less than 10^{-2} K/s. Metallic melts in contrast, have non-directional bonding, so the atomic rearrangements occur very rapidly, even at high degrees of cooling below their equilibrium freezing temperatures. Hence, very high cooling rates (>10^5 K/s) must generally be imposed to form metallic glasses [29].

Glass Forming ability (GFA) is the term used as a measure of the ease with which an alloy melt can be undercooled below the glass transition temperature during solidification. The most straightforward indicators of GFA are critical cooling rate (R_c), and maximum casting thickness. Alloys with high GFA have a lower R_c and greater maximum casting thickness. Although these indicators are fundamental, they do not tell much about the potential of a system to be vitrified into amorphous form. More advanced indicators of GFA are therefore needed. Reduced glass transition temperature (T_{rg}) which is defined as, T_g/T_l, is a widely used as an indicator of GFA.

When the interval between T_g and T_l decreases, the value of T_{rg} increases, so that the probability of being able to cool through the interval between T_l and T_g without crystallization is enhanced, therefore the GFA is increased. As the alloying concentration is increased, T_g generally varies insignificantly, while T_l often decreases more substantially. The ratio T_g/T_l also arises from the requirement that the viscosity must be large at temperatures between the melting

point and T_g. The viscosity at T_g being constant, the higher the ratio of T_g/T_l, The higher will be the viscosity at the nose of the TTT or CCT curves and hence smaller will be the R_c for glass formation [9]. Maximum casting thickness, R_c and T_{rg} data plotted for different alloys are given in Fig. 2.3.

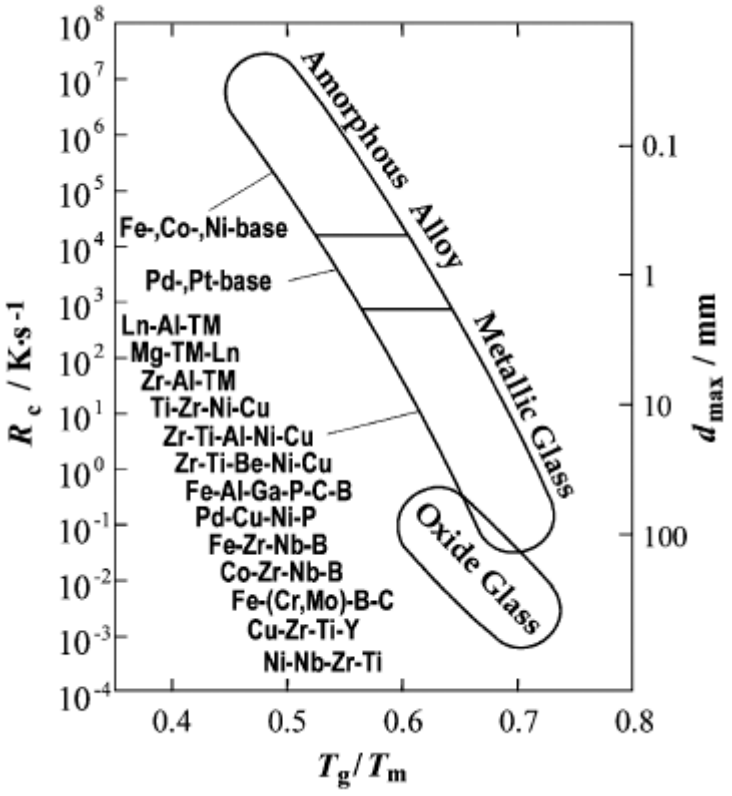

Figure 2.3 Relationship between the critical cooling rate, maximum casting thickness and reduced glass transition temperature for ordinary amorphous alloys, bulk amorphous alloys and oxide glasses [23].

The alloy systems, for which the glass formation occurs most readily, are those that manifest either one or more deep eutectics, or a step and substantial decrease

in liquidus (T_l) with increasing percentage of solute, to a plateau over which T_l is low in comparison with the melting point of the host metal [29].

Although there are many T_{rg} values reported in the literature, they are calculated using both T_g/T_l and T_g/T_m interchangeably by the researchers. According to Lu et. al. [31] the T_g/T_l parameter is more consistent to indicate GFA, while T_g/T_m can have a less strong correlation with GFA. In their study, various bulk glass forming alloys based on Zr, La, Mg, Pd and rare-earth elements are produced; using thermal analysis their T_g, T_m (solidus temperature) and T_l (liquidus temperature) values are determined. Accordingly, when T_{rg} is calculated based on T_g/T_m, while T_{rg} is constantly increasing the critical cooling rate first shows a decreasing trend, followed by an incremental trend. However, when T_{rg} is calculated based on T_g/T_l an increase in the T_{rg} is always accompanied by a decrease in the critical cooling rate. This arises mainly from the higher dependency of T_l to composition while T_g and T_m are less composition dependent. For Mg based alloys this behavior is shown in Fig. 2.4.

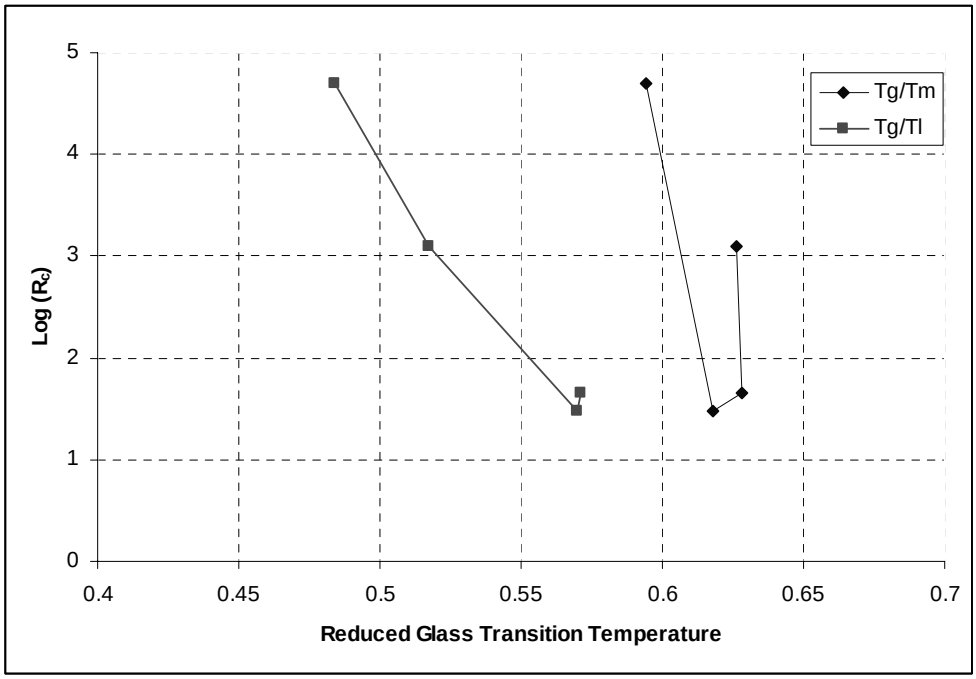

Figure 2.4 Critical cooling rate as a function of T_g/T_m and T_g/T_l [31].

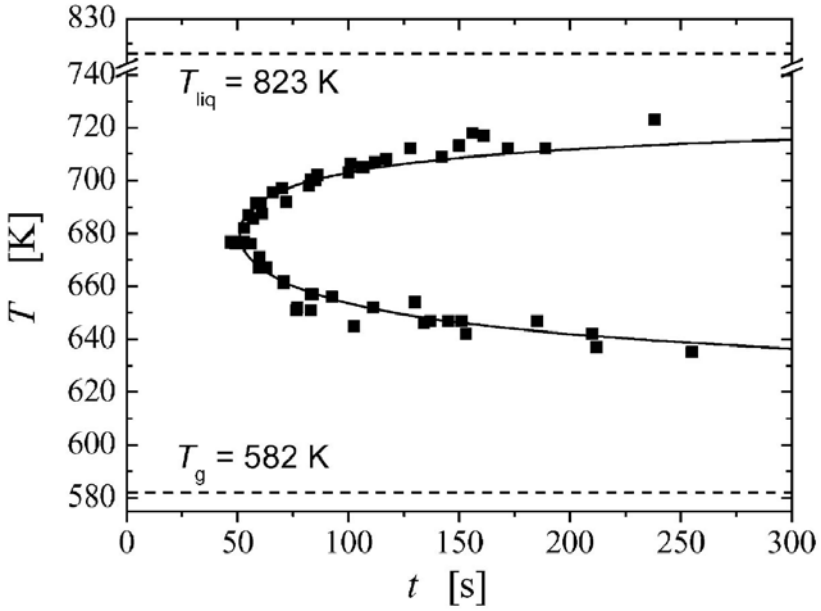

Figure 2.5 Time-transformation-temperature (TTT) graph of $Pd_{40}Cu_{30}Ni_{10}P_{20}$ [9].

Experimental studies that have been carried out construct time-transformation-temperature (TTT) graphs. Remarkably sluggish crystallization kinetics in the undercooled liquid permitted detailed studies of liquid properties via measuring different transformation times for different temperatures. A complete TTT diagram for $Pd_{40}Cu_{30}Ni_{10}P_{20}$ system is given in Fig. 2.5. The TTT diagram has a nose at 680 K and the transformation time is 50 seconds. The critical cooling rate of the alloy was measured to be 0.33 K/s [9].

Metallic glass formation is inevitably a non-equilibrium reaction. From the thermodynamical point of view, the stable structure for metallic alloys is the crystalline structure at low temperatures and atmospheric pressure.

Various models have been proposed to describe glass forming ability. These models can be grouped into three categories which are thermodynamic, kinetic, and structural. However the discussions in all models are interrelated.

2.6.2 Thermodynamic Model

According to the thermodynamic model, high glass forming systems should have low Gibbs free energy for the transformation of liquid to crystal phase. The lower the ΔG, the lower will be the driving force for the liquid to crystallize. In the relation $\Delta G = (\Delta H - T.\Delta S)$ for Gibbs free energy, the low ΔG value is obtained in the combination of low ΔH and high ΔS values. Here ΔH and ΔS are enthalpy of fusion and entropy of fusion respectively. The large ΔS is expected to be obtained in multicomponent alloy systems because ΔS is proportional to the number of microscopic states. The free energy, at a constant temperature, also decreases in the cases of low chemical potential caused by the low enthalpy and high reduced glass transition temperature as well as of high interface energy between liquid and solid phases. Based on these thermodynamical aspects, it can be said that multiplication of alloy components leading to the increase in ΔS causes an

increase in the degree of dense random packing which is favorable for the decrease in ΔH and increase in solid/liquid interface energy [23].

The amorphous phase is stabilized with respect to the liquid phase below the T_g, so that the amorphous phase has a lower energetic state than the liquid phase, which is measurable by thermal methods such as differential scanning calorimetry (DSC). In a typical DSC trace like Fig. 2.6 it can be observed that enthalpy decreases with glass transition and energetically relaxes compared to supercooled liquid [32].

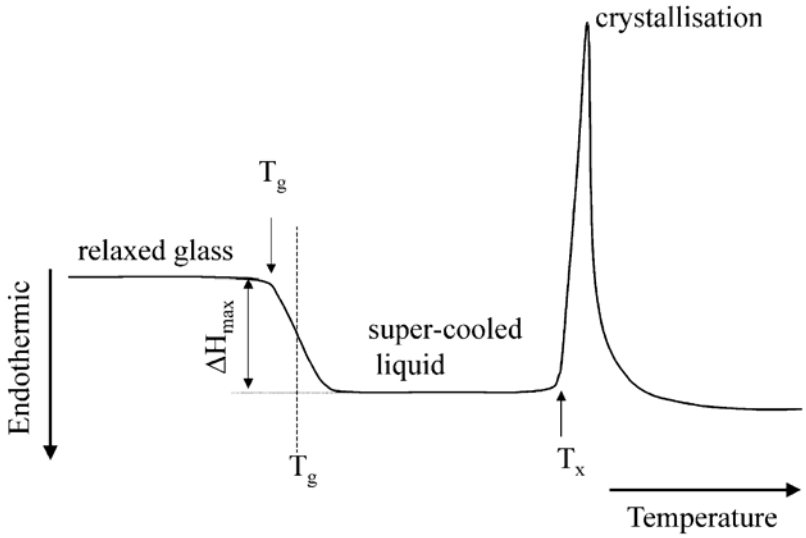

Figure 2.6 A Typical DSC trace of a glassy alloy [32].

2.6.3 Kinetic Model

In the kinetic model a quantitative rationalization of glass forming ability is most usefully approached in terms of kinetics of crystallization, since interest is on the avoidance of crystallization [29].

Turnbull [33] investigated the process of crystal nucleation. The bulk free energy change associated with transformation of the undercooled liquid to the crystal phase, ΔG_v, is given by the linear approximation $\Delta G_v = \Delta H_f \Delta T_r$, where the ΔH_f is the molar enthalpy of fusion and ΔT_r the reduced undercooling, $(T_l-T)/T_l$. The homogeneous nucleation frequency I_v was shown to be given by [33]:

$$I_v = \frac{k_n}{\eta(T)} \exp\left[-16\pi\alpha^3\beta / 3T_r\Delta T_r^2\right] \tag{2.1}$$

where k_n is a kinetic constant, $\eta(T)$ is the temperature dependent shear viscosity, T_r is reduced temperature (T/T_l) and α and β are dimensionless parameters related, respectively, to the liquid/crystal interfacial energy σ and to molar entropy of fusion.

$$\alpha = (NV^2)^{1/3}\sigma / \Delta H_f \tag{2.2}$$

$$\beta = \Delta S_f / R \tag{2.3}$$

N is the Avogadro number and V the molar volume of the crystal. It is evident from equation 2.3 that, as the magnitude of $\alpha\beta^{1/3}$ increases, I_v decreases very steeply, for a given temperature and melt viscosity.

For metallic melts, in common with other simple materials, experimental derivations of σ indicate $\sigma\beta^{1/3}$ is around 0.5; this is consistent with their resistance to homogeneous nucleation up to large undercoolings. An approximately constant value of $\sigma\beta^{1/3}$ being assumed, the principle variable governing I_v and its temperature dependence then becomes the function of $\eta(T)$. Since $\eta(T_l)$ is constant for alloy melts, at typically a few centipoises, the reduced temperature becomes the controlling factor. As ΔT_r increases, I_v initially increases steeply reflecting the increasing driving force, until eventually, it peaks and undergoes a sharp decrease as the increasing η becomes dominating factor at large ΔT_r values. As T_{rg} increased, η increases more rapidly with increasing ΔT_r and (T_v-T_r) peak is

rapidly lowered and shifted to the higher T_r. Thus it becomes easier to avoid nucleation [29].

2.6.4 Structural Model

It is well-established that as the size and valence differences between component atoms increase, thus the electronegativity difference increases; the atomic interaction, expressed by negative excess enthalpy and free enthalpy of mixing also increases. Strong unlike atom interaction (ordering) leads to the formation of stable intermetallic compound phases from eutectic reactions occurring at low temperatures [29]. Upon solidification, ordered phases encounter growth problems due to the complex structure arising from preferred heterocoordination. This phenomenon increases the glass forming ability.

Also according to Inoue [24], the combination of the significant difference in atomic sizes and negative heats of mixing is expected to cause an increase in random packing density in the supercooled liquid which enables the achievement of high liquid/solid interfacial energy as well as the difficulty of atomic rearrangements leading to the decreases in atomic diffusivity and viscosity.

2.6.5 Semiempirical Criteria

According to Inoue [17] alloy systems with high glass forming ability obey the following three empirical rules:

1. Multicomponent systems containing more than three elements
2. Significant difference in atomic size ratios above 12 % among the three main constituent elements.
3. Negative heats of mixing among the main constituent elements.

According to confusion principle larger number of components in an alloy system destabilizes competing crystalline phases which may form during cooling. This effect frustrates the tendency of the alloy to crystallize by making the melt more stable relative to crystalline phases [34]. The widely differing atomic radii and the high number of different elements confuse the atoms so they don't know where to go to form crystal as they cool.

According to the data obtained for multicomponent amorphous alloys, it has been stated that the amorphous alloys can have higher degrees of dense randomly packed atomic configurations, which are different from those of the corresponding crystalline phases, and the homogeneous atomic configuration of the multicomponents on long-range scale [18].

2.6.6 Atomic Size Distribution Plot

Although there is a large amount of information about criterions of glass forming ability, the task of exploring new alloy systems is still based on manual labor intensive trial and error methods, where quite a number of compositions can be rendered experimentally. In order to narrow the composition choice for research Senkov at al. [35] investigated compositions and atomic radii of constituents in amorphous alloys. Most amorphous metallic alloys have a characteristic dependence of concentrations of alloying elements on their relative atomic radii, where relative radius is defined as radius of solute atom divided by the radius of the solvent atom.

For a bulk amorphous alloy system, where the critical cooling rate is less than 10^3 K/s, usually the solvent element has the highest atomic size. Concentration decreases for the solutes with lower atomic radii, exhibits a minimum and then starts to increase for the elements with the smallest atomic radii. When the concentration vs. atomic size (so called atomic size distribution) is plotted this

behavior is characterized with a concave upward shape. For ordinary amorphous alloys with marginal glass forming ability a concave downward shape is observed where the solvent atom has an intermediate size. Atomic size distributions of two ordinary and bulk amorphous alloys are given in Fig. 2.7.

These characteristic atomic size distributions show correlation with the reported low molar volume and high atomic packing of bulk amorphous alloys [35]. Concave upward shape provides a more close packing compared with the concave downward behavior. It has been shown that a more compact structure has a higher viscosity and lower diffusivity, which leads to a more difficult nucleation and crystallization process which enhances glass forming ability significantly [36].

A model has been developed in order to explain the concave upward shape of the atomic size distribution in bulk amorphous alloys. Accordingly, when all the alloying additions are smaller than the solvent element, some of them are located at the substitutional sites while others at the interstitial sites. Substitutional and interstitial atoms attract each other because of the different strain fields they produce around them. This attraction produces short-ranged ordered clusters which may stabilize the amorphous structure [36].

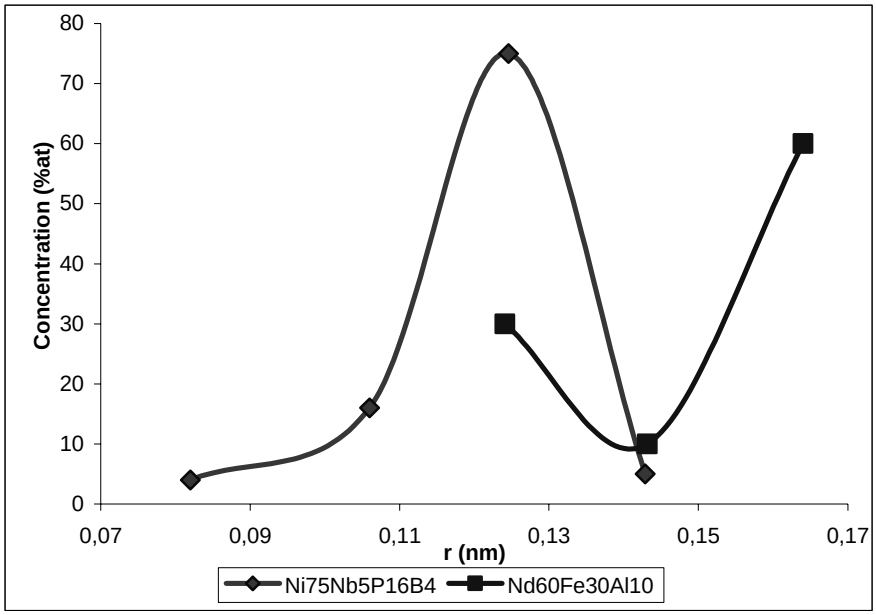

Figure 2.7 Atomic size distribution of $Ni_{75}Nb_5P_{16}B_4$ with a critical cooling rate around 10^4-10^6 K/s, and $Nd_{60}Fe_{30}Al_{10}$ with a critical cooling rate of around 10-1000 K/s [35].

2.6.7 γ Criteria for Glass Forming Ability

ΔT_x, and T_{rg} are used as indicators of GFA. However in different alloy systems they sometimes show contradicting results and therefore reliability of these indicators are in question. Lu et. al. [37] analyzed factors that associate with GFA from the perspectives of devitrification and amorphitization to propose a new simple indicator of GFA.

A wide supercooled region ($\Delta T_x=T_x-T_g$) for an amorphous alloy with low tendency of crystallization indicates the stability of the amorphous phase relative to its crystalline counterpart upon reheating. However, for different alloy systems this should be normalized with T_g in order to become comparative in different systems.

$$\frac{T_x - T_g}{T_g} = \frac{T_x}{T_g} - 1 \tag{2.4}$$

From the above relation it can be comprehended that GFA is proportional with the factor T_x/T_g .

From the perspective of amorphitization using non-isothermal crystallization kinetics it is found that T_x/T_l ratio increases with the increasing viscosity of the supercooled liquid, fusion entropy and activation energy of viscous flow and with decreasing T_l. The dependence of the T_x/T_l ratio on the magnitudes of liquid parameters is similar to those of critical cooling rate R_c. Therefore T_x/T_l ratio becomes a reasonable indicator of high GFA.

$$GFA\alpha\left(\frac{T_x}{T_g}, \frac{T_x}{T_l}\right)\alpha\left(\frac{T_g}{T_x}, \frac{T_l}{T_x}\right)^{-1} \tag{2.5}$$

In order to come up with a simpler criterion, the sum of the two ratios can be taken to yield a new indicator for GFA designated by the symbol γ.

$$\gamma = \left(\frac{T_g}{T_x} + \frac{T_l}{T_x}\right)^{-1} = \frac{T_x}{T_g + T_l} \tag{2.6}$$

Regardless of the alloy system, the relationship between γ and the critical cooling rate R_c, as well as critical section thickness t_{max} has been formulated as follows:

$$R_c = 5.1 * 10^{21} \exp(-117.19\gamma) \tag{2.7}$$

$$t_{\max} = 2.80 * 10^{-7} \exp(41.70\gamma) \tag{2.8}$$

2.6.8 Bulk Glass Forming Ability (BGFA)

Recently Akdeniz et al. [38] investigated the bulk glass formation in accordance with solidification behavior. It has been proposed that alloys having eutectic peritectic reaction sequence are quite favorable for achieving rather high BGFA. Characteristic DSC pattern, involving high temperature peritectic and subsequent eutectic exothermic peaks are observed for this kind of alloys. When a high temperature peritectic reaction produces a facet forming complex intermetallic phase, on further cooling, this phase becomes one of the constituents of coupled growth of subsequent eutectic reaction. The coupled zone becomes skewed towards faceted phase and irregular eutectic formation occurs for equilibrium cooling rates. However, upon rapid solidification, if the growth rate exceeds the limiting growth rate of eutectic transition to amorphous phase instead of irregular eutectic is observed

2.6.9 Structure of Amorphous Alloys

In order to understand the local atomic structure of amorphous alloys, the parent liquid structure may be investigated. When a metallic melt is vitrified the liquid structure is frozen however some structural relaxation occurs. Any model constructed to describe atomic structure should be in accordance with radial distribution function (RDF) which is the most valuable empirical data related with the atomic structure for amorphous alloys. In RDF, the number of atoms at a given distance r from a specified atom centre is compared with the number of atoms at the same distance in an ideal gas at the same density. RDF can be constructed from X-ray or neutron scattering experiments using Fourier transforms to invert the structure factor from $\vec{q}$ space to real space.

Bernal [40] proposed a model depending on constituent atoms having high coordination numbers, with surrounding atoms generally in contact. In the

proposed model the atoms were considered as hard spheres and their local structure was determined by the restrictions on space filling consequent upon the inability of two atoms to approach more closely than one diameter. The structural unit of Bernal's model was several small polyhedra. Gaskell adopted chemical ordering and proposed trigonal prisms as the fundamental unit of structure. Within this respect structure of metal-metalloid glasses were attempted to be explained [39].

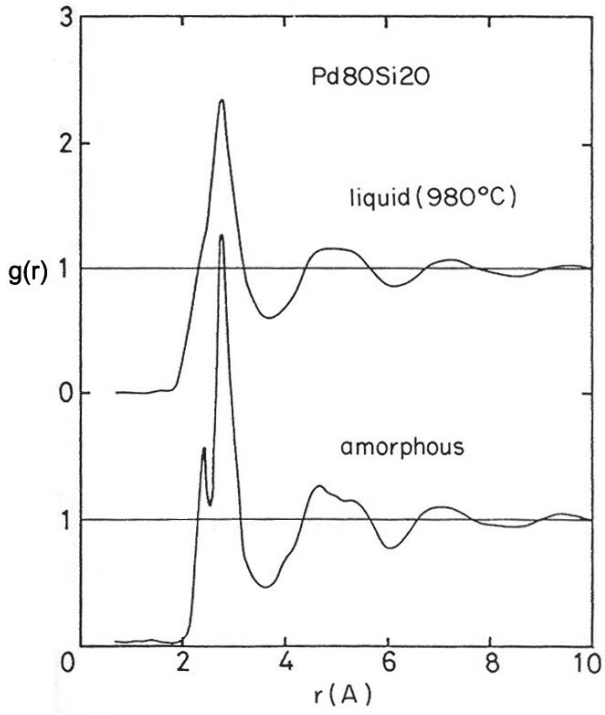

Figure 2.8 Total RDFs of liquid and amorphous $Pd_{80}Si_{20}$ alloy [41].

While modeling studies are continuously developing experimental RDFs can be directly analyzed to interpret the local atomic configuration. Most of the binary metallic glass shows a characteristic distinction from their liquid structure in RDF plots, namely the splitting of the second peak. Also the sharpening of the peaks is observed when liquid melt is vitrified. RDF of $Pd_{80}Si_{20}$ alloy is given in Fig. 2.8 as an example. Compared to the liquid, the atoms in the amorphous state are

relatively restricted movement. The basic arrangement of atoms in amorphous state and liquid are similar, in which atoms are randomly distributed in nearly closed packed structure and the mean free path is short and comparable to the atomic size. This implies that the positional correlation of atoms is relatively strong within the near neighbor region. However, the average atomic configuration in the liquid is more homogeneous than that of the amorphous state because the atomic vibration is high. In other words, the atomic configuration in the amorphous state shows a slight inhomogenity, which frequently gives a deformed sharp pattern with second peak splitting in RDF [42].

When the BMGs, emerged in the 1990's are concerned the structure discussions should be revisited. BMG were found to have a new type of glassy structure with higher dense random packing. The densities of BMG's are very near to their crystalline counterparts, where the departure is more for ordinary metallic glasses. [43]. Also the characteristic RDF pattern of ordinary metallic glasses are not observed for BMGs.

Inoue [24] classified BMGs into three types namely metal-metal type alloys, metal-metalloid type alloys and Pd-metalloid type alloys. The different types of atomic structures are given in Fig. 2.9.

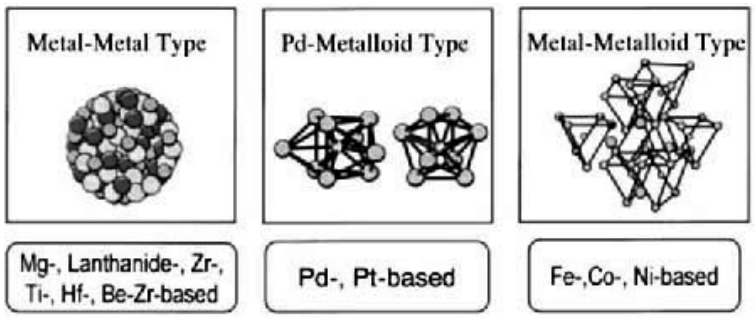

Figure 2.9. Three types of BMGs and their atomic structures [34].

In metal-metal type alloys, TEM studies reveal that glass consists of icosahedral clusters. When annealing is carried out in supercooled liquid range, the first crystallization phase becomes the icosahedral quasicrystallines. At higher temperatures transformation to stable crystalline phases occurs.

The structure provides a reasonable explanation of supreme GFA of BMGs. For the ordinary metallic glasses, where the atomic structure of the amorphous phase similar to the corresponding crystalline phase, the vitrification occurs at high cooling rates. However, in alloy systems with BGFA at relatively low cooling rates, still nucleation and growth of crystalline phases can be inhibited. Upon cooling crystallization of BMGs need a substantial redistribution of the component elements across the icosahedral liquid. The high dense randomly packed structure of the BMG in its supercooled state results in extremely low atomic mobility. Therefore, atomic redistribution becomes a harder task. Icosahedral clusters having five-fold rotational symmetry are incompatible with the translational symmetry of normal crystalline phases and this fundamental structural discontinuity across the amorphous and crystalline phases suppress the nucleation and growth. [34]

For metal-metaloid glasses, a network of atomic configurations consisting of trigonal prisms which are connected with each other through glue atoms are commonly found. The structural investigation shows that Pd–Cu–Ni–P BMGs consist of two large clustered units of a trigonal prism capped with three half-octahedra for the Pd–Ni–P and a tetragonal dodecahedron for the Pd–Cu–P region [34].

2.7 MOLECULAR DYNAMICS IN ACCORDANCE WITH GFA

Molecular dynamics simulation method is one of the most powerful simulation techniques to understand macroscopic material properties from an atomic description of the system. A detailed explanation of the method is presented in Chapter III. This powerful tool is starting to be more intimate with GFA; in order to get insight about both amorphous metallic structure and theory of glass formation. However, in order to mimic the rapid solidification process, description of interatomic interactions in an alloy system is crucial. Ab-initio MD calculations where quantum mechanical analyses employed for interaction at atomic scale is still computationally expensive even with the modern powerful computers. Therefore, the number of atoms that can be treated with this approach is quite few. Different interaction potentials have been developed and parameterized utilizing empirical and semi-empirical approaches.

Recently, Noya et.al. [44] studied constant temperature - constant therdynamical tension MD for Ni_3Al, NiAl, and $NiAl_3$ alloys with using embedded atom model (EAM). After melting the alloys at 2000 K, quenching with cooling rates 10^{13} K/s and 4.10^{13} revealed the amorphous structure for all compositions.

Wang et. al. [45] used constant temperature – constant pressure MD to explore the effect of atomic size mismatch on GFA. For this purpose starting from room temperature Au, Au-Ag and AuCu systems were heated a few hundred degrees above their melting temperature and quenched back to room temperature. Pure Au and Au-Ag alloy formed a crystalline phase at all quench rates chosen, while Au_3Cu became amorphous when quenched with a cooling rate of 4.10^{12} K/s. Au-Ag having similar atomic radii failed to form an amorphous phase. However Au-Cu having dissimilar atomic radii revealed a higher GFA.

Qi et. al. [46] performed NPT molecular dynamics for $PdNi_3$. After melting at 1700 K. Four different cooling rates were utilized; 1.10^{13} K/s, 6.10^{11} K/s, 5.10^{11} K/s and $1x10^{11}$ K/s in order to quench to room temperature. At high cooling rates, cooling lead to continuous change in volume. Such characteristics indicate amorphous phase formation. T_g of the alloy was determined as 950 K. In order to analyze the local structure, pair analysis was carried out for the glassy alloys and only a small percentage of fcc pairs were found indicating that fcc local orders are insignificant. Nevertheless, the predominance of local icosahedral features over crystalline short range packing was observed.

Kart et. al. [47] investigated diffusion properties of $Pd_{0.8}Ag_{0.2}$ alloy with NPT MD. Sutton Chen potentials were used. Diffusion constant of the glassy alloy was calculated using mean square distance. Accordingly it is found that upon heating linear increase in the diffusion is found while an exponential decrease is observed on cooling.

Wang et. al. [42] performed constant temperature – constant pressure MD to explore the effect of quenching rates on medium range order (MRO). The main feature of the MRO is the presence of a prepeak at structure factor. It occurs before the main peak which is associated with short range order (SRO). When heating is performed to Cu_3Ni alloy, at temperatures below 1700 K a prepeak is observed but above this temperature MRO ceases to exist. Effect of quenching is examined by monitoring total structure factor at different temperatures. It is observed that prepeak intensity increases with decreasing temperature, which means greater number of clusters of MRO. On the other hand prepeak position is unchanged which indicates, sizes of clusters are invariant but only the number is increased.

CHAPTER III

METHODOLOGY

3.1 PSEUDOPOTENTIAL APPROXIMATION AND ONE ELECTRON THEORY

3.1.1 The Principals of the One Electron Theory

Principally, any information about a crystal structure can be found by solving the Schrödinger's equation for a system of interacting nuclei and electrons that form the crystal structure. This however requires some simplifications in the Schrödinger's equations, since it is too complicated, without these simplifications to solve. The following simplifications are adopted to solve the problem in the basis of one electron theory:

- It is generally assumed that nuclei are too massive to follow the rapidly changing spatial distribution of the electrons. This is also named as "Adiabatic Approximation". Thus, this approximation divides Schrödinger's equation into two different equations; one for the electron and other for the nuclei.

- In the equation for the electrons, the individual motions of the electrons are considered separately, not as a whole. Each electron will be thought of as moving in the effective field of the (stationary) nuclei and all the other electrons. This approximation is called the "Effective field Approximation". Lastly, total electron wave function ψ, is expressed in the terms of individual electron wave functions ψ_i.

- Further approximations are made in the actual evaluation of the total function and in the consequent determination of the effective potential as seen by a single electron. This is called the "Pauli Exclusion Principle". Thus, all together leads to a system of one-electron Schrödinger equation in the Hartree-Fock approximation including both Coulomb and exchange interactions between the electrons.

3.1.2 Nearly-Free Electron Model

One electron theory can be taken as a basis for a more detailed model, 'Nearly Free Electron Model'. As stated by the electron theory, total crystal energy can be given as follows:

$$\Sigma_{str} = U_0 + U_{bs} + U_{lattice} \tag{3.1}$$

Here, the $U_{lattice}$ involves the Coulomb repulsion between the ion cores, the U_0 is the volume dependent electronic contribution and U_{bs} is the structure dependent electronic contribution to the total energy. The values for U_0 and U_{bs} can be calculated from the following equations:

$$U_0 = 2 * \frac{\Omega}{(2\pi)^3} * \int_{\substack{inside\ the\\ Fermi\\ sphere}} \left(K^2 + \left\langle \vec{K} \middle| V \middle| \vec{K} \right\rangle \right) d^3K \tag{3.2}$$

$$U_{bs} = -2 * \frac{\Omega}{(2\pi)^3} * \sum_q \left| S\left(\vec{q}\right) \right|^2 \int_{\substack{inside\ the\\ Fermi\\ sphere}} \frac{\left| \left\langle \vec{K} + \vec{q} \middle| V \middle| \vec{K} \right\rangle \right|^2}{\left(\vec{K} + \vec{q} \right)^2 - K^2} d^3K - U_{el}^{int} \tag{3.3}$$

The g_n vectors are replaced with the ordinary position vectors of q. The wave vector is designated as k, where Ω and V stands respectively for volume of the crystal and crystal potential.

Above, U_0 describes a 'free' electron gas with the inclusion of electron-electron interaction. Moreover, U_{bs} is associated with band characteristics and named as "Band Structure Energy". Lastly, when calculating E(k), the interaction energy of each electron pair contributes to the energy of each electron, meaning that the electron-electron interaction energy is counted twice, while calculating the total energy of the crystal. The term U_{el}^{int} is used in order to get rid of this additional energy calculated by subtracting it from the equation.

If the potential V is local, its form factor K is independent and can be taken out of the K integral that appears then in U_{bs}. This solution is known as Lindhard's function:

$$\chi\left(\vec{q}\right) = -2 * \frac{\Omega}{(2\pi)^3} * \frac{1}{N} * \int_{\substack{inside\ the\\ Fermi\\ sphere}} \frac{d^3k}{\left(\vec{k}+\vec{q}\right)^2 - \vec{k}^2} \tag{3.4}$$

If the Fermi surface is assumed spherical, then the Eq. (3.4) becomes:

$$\chi(q) = -\frac{Z}{4}\left(\frac{2}{3}E_F^{\circ}\right)^{-1}\left(1 + \frac{1-x^2}{2x}\ln\left|\frac{1+x}{1-x}\right|\right) \tag{3.5}$$

In Eq. (3.5), $x = k/2k_F$ and $E_F^0 = (3\pi^2 z/\Omega_0)^{2/3}$.

The electron-electron interaction energy U_{el}^{int} may be represented [48] as a result of interactions between the non-uniform part of the crystal electron density and the potential, which is the difference between the crystal potential ϑ^{cr} and the initial potential ϑ^{ion} of the system of ions. U_{el}^{int} can be expressed in terms of the form factor of V^{cr} (q), if a function, $\alpha(\vec{q}) = \vartheta^{ion}/\vartheta^{cr}$, is set up in order to characterize this potential.

$$U_{el}^{\text{int}} = \sum_q |S(q)|^2 |V(q)|^2 \chi(q)(1-\alpha(q)) \tag{3.6}$$

And;

$$U_{bs} = \sum_q |S(q)|^2 |V(q)|^2 \chi(q) - U_{el}^{\text{int}} = \sum_q |S(q)|^2 |V(q)|^2 \chi(q)\alpha(q) \tag{3.7}$$

Where $S(q) = \frac{1}{N}\sum_i e^{-iqt_i}$

Note that, no assumptions about the nature of potential except the locality of the potential or about the way in which the crystal potential is composed of the ionic potentials (that is, about the screening mechanism) has been made while deriving this equation. $\chi(q)$ is a function arising from perturbation theory whereas $\alpha(\vec{q})$ is the ratio of the original potential of the ions to the crystal potential.

A frequently used characteristic function Φ_{bs} (q) is defined as:

$$\Phi_{bs}(q) = \sum_q |V(q)|^2 \chi(q)\alpha(q) \tag{3.8}$$

Using the Eq. (3.9), U_{bs} can be rewritten as a sum, over the lattice sites, of Fourier transforms Φ_{bs} (R_i), where transforms can be defined as follows:

$$\Phi_{bs}(R) = 2\frac{\Omega}{(2\pi)^3}\int \Phi_{bs}(q) e^{iqR} d^3q \tag{3.9}$$

$\Phi_{bs}(R)$ may be thought of as the potential of the interaction between ions through the electron gas (the same electron is simultaneously attracted by all the ions, hence their mutual attraction). It is this interaction that must compensate for the direct Coulomb repulsion of the ions.

The total interatomic interaction potential has the form of

$$\Phi(R) = \frac{Z^2 e^2}{r} + \frac{2\Omega}{(2\pi)^3}\int \left[V^{str}(q)\right]^2 \chi(q)\varepsilon^*(q) e^{i\vec{q}\vec{r}} d^3q \tag{3.10}$$

When it is given that the systems volume is constant, Φ(R) in Eq. (3.10) describes the interaction between the atoms. In other words, it is the redistribution of the atoms within the crystal system.

3.1.3 Calculation of Ordering Energies and Pairwise Interatomic Interactions for Ternary Alloys

According to electronic theory of ternary alloys in the pseudopotential approximation, the partial ordering energies itself is [48-53]:

$$w_{\alpha\beta}(R_i) = V_{\alpha\alpha}(R_i) + V_{\beta\beta}(R_i) - 2V_{\alpha\beta}(R_i) \tag{3.11}$$

and it can be calculated as;

$$w_{\alpha\beta}(R_i) = \frac{2}{N}\sum_{q}^{2} F_p(q) e^{i\vec{q}\vec{R}_i} \tag{3.12}$$

or;

$$w_{\alpha\beta}(R_i) = \frac{\overline{\Omega}}{\pi^2}\int dq * q^2 F_p(q) \frac{\sin qR_i}{qR_i} \tag{3.13}$$

in which,

$$F_p(q) = \frac{\overline{\Omega}}{8\pi}\left|\Delta W^b(q)\right|^2 q^2 \frac{1-\varepsilon(q)}{\varepsilon^*(q)} + \frac{2\pi}{\overline{\Omega}}(\Delta Z)^2 \frac{1}{q^2}\exp\left(-q^2/4\xi\right) = F_{bs}(q) + F_{es}(q) \tag{3.14}$$

is characteristic function of partial ordering energy.

When $F_p(q)$ in Eq. (3.14) is adopted into the Eq. (3.13), $w_{\alpha\beta}(R_i)$ may be written as:

$$w_{\alpha\beta}(R_i) = \frac{\overline{\Omega}}{\pi^2}\int dq * q^2 \frac{\sin qR_i}{qR_i}\left\{\frac{\overline{\Omega}}{8\pi}q^2\frac{1-\varepsilon(q)}{\varepsilon^*(q)}\left|W_\beta^b(q)\right|^2 + \frac{2\pi}{q^2}\left(Z_\beta^*\right)^2 \exp\left(-q^2/4\xi\right)\right\}$$
$$-\frac{2\overline{\Omega}}{\pi^2}\int dq * q^2 \frac{\sin qR_i}{qR_i}\left\{\frac{\overline{\Omega}}{8\pi}q^2\frac{1-\varepsilon(q)}{\varepsilon^*(q)}W_\alpha^b(q)W_\beta^b(q) + \frac{2\pi}{q^2}Z_\alpha^* Z_\beta^* \exp\left(-q^2/4\xi\right)\right\}$$
$$+-\frac{\overline{\Omega}}{\pi^2}\int dq * q^2 \frac{\sin qR_i}{qR_i}\left\{\frac{\overline{\Omega}}{8\pi}q^2\frac{1-\varepsilon(q)}{\varepsilon^*(q)}\left|W_\alpha^b(q)\right|^2 + \frac{2\pi}{q^2}\left(Z_\alpha{}^*\right)^2 \exp\left(-q^2/4\xi\right)\right\}$$

(3.15)

Each integral in the last equation corresponds to the total effective interatomic interaction potential and depends on the interatomic separation in a quasi-oscillatory manner.

Interatomic interaction potentials between different ionic pairs in the alloys can be calculated in a similar way,

$$V_{\alpha\beta}(R_i) = \frac{\overline{\Omega}}{\pi^2}\int_0^\infty F_{\alpha\beta}^1 \frac{\sin qR_i}{qR_i}.q^2 dq \tag{3.16}$$

where,

$$F_{\alpha\beta}^1(q) = -\frac{\overline{\Omega}}{8\pi}\left|W_\alpha^\circ(q).W_\beta^\circ(q)\right|.q^2\frac{\varepsilon(q)-1}{\varepsilon^*(q)} + \frac{2\pi}{\overline{\Omega}.q^2}\left|Z_\alpha^*.Z_\beta^*\right|.\exp(-\frac{q^2}{4\xi}) \tag{3.17}$$

In the equations above $\overline{\Omega} = c_A\Omega_A + c_B\Omega_B + c_C\Omega_C$ is the average atomic volume of the alloy; ε(q) is the dielectric constant in the Hartree approximation; $\varepsilon^*(q)$ is the modified dielectric constant which takes into account the correlation and exchange effects; $W_\alpha^\circ(q)$ and $W_\beta^\circ(q)$ are the form factor of an unscreened pseudopotential of α and β ions respectively; $Z_\alpha^*(Z_\beta^*)$ is the effective valency of the α(β) component atoms; ξ is the Ewald parameter.

Partial ordering energies, $w_{\alpha\beta}(R_i)$, and pairwise interatomic interaction potentials, $V_{\alpha\beta}(R_i)$, for any ternary alloy, can be calculated by the help of the above

equations from (3.12) to (3.17) as a function of interatomic distance, R_i when the form factor of unscreened pseudopotentials, $W°(q)$, and effective valances, Z^*, which are known for the ions involved, are provided.

3.2 COMPUTER SIMULATION

Computer simulation is a technique to represent the real world using a computer program by imitating internal processes in a system. A simulation study of a physical system requires a model which has the appearance and/or behavior of the system without the reality [54].

There are only a handful of non-trivial, exactly soluble problems in statistical mechanics. By this it is referred that a complete specification of microscopic properties of a system leads directly and perhaps easily, to a set of interesting results or macroscopic properties. Computer simulations have a valuable role to play in providing essentially exact results for problems in statistical mechanics which would otherwise only be soluble by approximate methods, or might be quite intractable [55].

Along with the rapid increase in computer performance, computer simulations are becoming a powerful investigation tool. With decreased time of running simulation programs, well defined characteristics of systems are computed, while in experimental methods, sometimes observing a single characteristic without screening other parameters can be quite a difficult task.

Computer simulation methods fill the gap between the theoretical and experimental methods. Eliminating the obligatory approximations in order to find analytical solutions, validity of theoretical models can be tested and specific parameters of a system can be computed without actually performing a physical experiment. Due to this connecting role and the way in which simulations are

conducted and analyzed, these techniques are often termed computer experiments. The relation between theoretical experimental and simulation techniques is given Fig. 3.1.

Computer simulation provides a direct route from microscopic details of a system such as the masses of the atoms, the interactions between them and molecular geometry etc., to macroscopic properties of experimental interest, such as the equation of state, transport coefficients, structural order parameters and so on. As well as being of academic interest, this type of information is technologically useful. It may be difficult or impossible to carry out experiments under extremes of temperature and pressure, while a computer simulation of the system would be perfectly feasible [55].

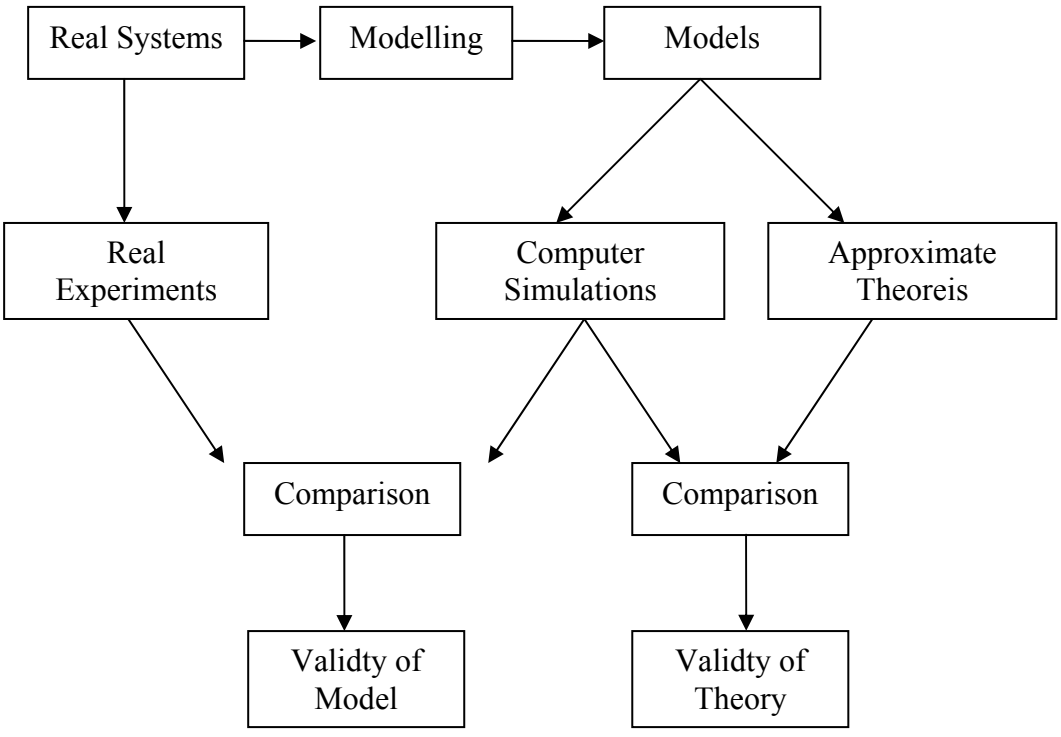

Figure 3.1 Connection between simulation, theoretical, and experimental techniques [55].

A wide variety of simulation techniques have been developed up to date. The most popular techniques used to study the molecular level details are Molecular dynamics and Monte Carlo methods.

3.2.1 Molecular Dynamics

Simplest definition for the molecular dynamics (MD) method can be; solution of classical equations of motion via numerical integration, to simulate the motion of particles in a many-body system, with a predetermined interatomic potential for a finite time. Solution of equation sets for all particles yield the trajectory of the system which is the momenta and positions of all particles at all times.

Although at first glance utilizing classical mechanics for the nuclear motion of atomic particles seems inappropriate, for quite a wide range of materials it renders a good approximation. If De Broglie's wavelength of the material is much smaller than the typical interspacing between particles ($\lambda << a$), classical mechanics can safely be used to describe the system. Only when light elements such as He, H_2 and/or low temperatures are involved; quantum effects should be taken into account [56, 57].

MD simulations have played a key role in advanced materials research. Generating the complete trajectory of a system allows one to study how atomistic processes determine macroscopic materials properties [58].

3.2.1.1 Equations of Motion

In order to discuss further features of MD, firstly equations of motion should be explored. Although there are several mathematical forms, Lagrangian equation seems perhaps the most fundamental.

$$\frac{d}{dt}(\partial L/\partial \dot{r}_i) - (\partial L/\partial r_i) = 0 \tag{3.18}$$

Lagrangian function is defined as follows

$$L(q, \dot{q}_k) = KE - U \tag{3.19}$$

where KE and U are kinetic and potential energies respectively. Using the classical definitions of kinetic energy, potential energy and equating the conservative force to negative gradient of potential function U, Eq. 3.18 deduces to Newton's second law.

$$m_i \ddot{r}_i = \nabla_{r_i} L = -\nabla_{r_i} L = f_i \tag{3.20}$$

where m_i is the mass of an atom i and f_i is the force on that atom. For a system with N atoms computation of the trajectory of a system with N atoms involves the solution of 3N second order differential equations [55].

Another way to formulate the classical equations of motion is Hamiltonian dynamics. Hamiltonian is the function of position and velocities whose value is constant in time, formally defined as,

$$H(r_i, p_i) = \frac{1}{2m}\sum_i p_i^{\,2} + U(r_i) \tag{3.21}$$

where p_i is the momentum of the atom i. Hamiltonian equations are as follows,

$$\frac{dp_i}{dt} = \frac{\partial H(r_i, p_i)}{\partial r_i} \qquad \text{and} \qquad \frac{dr_i}{dt} = \frac{\partial H(r_i, p_i)}{\partial p_i} \tag{3.22}$$

In order to work out the trajectory of a system with N atoms, this time solving 6N first order differential equations of type Eq. 3.22 is necessary. When the definition of momentum is substituted into Hamiltonian equations, it can be seen that the two sets of equations (Eq. 3.22 and Eq. 3.20) are identical [57,59].

3.2.1.2 Sampling From Ensembles

The main objective of the MD simulation is obtaining the macroscopic material properties from the information at microscopic level (trajectory) obtained during the simulation. The connection between macroscopic and microscopic level is established via statistical mechanics. With MD one can investigate thermodynamic and kinetic phenomenon.

Microscopic state is characterized by atomic positions and momenta of N atoms. Phase space is a 6N dimensional hyperspace where the positions and momenta of the entire system can be represented by a point, when the coordinate axes are components of position vectors and momentum vectors. As the positions and momenta change with time, the point moves describing a trajectory in the 6N dimensional phase space [59]. Therefore, with numerical integration of Newton's second law phase space trajectory is computed, which is the only information needed to describe macroscopic features.

A physical experiment is carried out with extremely large numbers of atoms, sampling an extremely large number of microscopic states. In statistical mechanics, averages corresponding to experimental observables are ensemble averages. An ensemble is a collection of all possible systems which have different microscopic states but have an identical macroscopic or thermodynamic state. An ensemble average is taken over a large number of replicas of the ensemble considered simultaneously. Ensemble average of any observable A which is expressed as a function of momenta (p) and position (r) is formally defined as:

$$\langle A \rangle_{ensemble} = \iint dp^N dr^N A(p^N, r^N) \rho(p^N, r^N) \tag{3.23}$$

$$\rho(p^N, r^N) = \frac{1}{Q} \exp\left[- H(p^N, r^N) / k_b T \right] \tag{3.24}$$

$$Q = \iint dp^N dr^N \exp\left[-H(p^N, r^N)/k_b T\right] \tag{3.25}$$

In the above equations ρ is the probability function, H is the Hamiltonian, k_B is the Boltzmann constant and Q is the partition function. From the complexity of integrals, it can be seen that ensemble averaging calculations are often extremely difficult. On the other hand, while calculating a trajectory in a molecular dynamics problem one can easily calculate the time average of an observable of interest [60].

$$\langle A \rangle_{time} = \lim_{t\to\infty} \frac{1}{t} \int_0^t A(p^N(t), r^N(t))dt \approx \frac{1}{M} \sum_{t=1}^{M} A(p^N, r^N) \tag{3.26}$$

At this stage ergodic hypothesis states that when a system is allowed to evolve for an infinite time it will navigate within all possible states and time average of the observable A will be equal to its ensemble average.

$$\langle A \rangle_{time} = \langle A \rangle_{ensemble} \tag{3.27}$$

In order to use ergodic hypothesis safely the number of time steps used in the simulation (M in Eq. 3.26) should be reasonable high, which is restricted by the computational performances of the hardware used.

3.2.1.3. Interatomic Potentials

At the microscopic level atoms interact with each other. Before performing a simulation interatomic potential must be set in analytical form. Most of the time in MD simulations for simplicity the potential is assumed to be pairwise additive, in which the interaction among N atoms is a sum of isolated two-body contributions.

$$U = \sum_i \sum_j u(r_{i,j}) \tag{3.28}$$

The simplest interactions between pairs of atoms are responsible for providing two principle features of interatomic force. Repulsion occurs at close range which is a resistance to compression, arising from the overlap of electron clouds and attraction over a range of separations in liquid and solid states for binding the atoms together. The potential form should be constructed carefully in order to model a system realistically [59, 61].

The best known and simplest interatomic potential is Lennard-Jones (LJ) potential which was originally formulated for Argon and is in the form:

$$u(r) = 4\varepsilon\left[\left(\frac{\sigma}{r}\right)^{12} - \left(\frac{\sigma}{r}\right)^{6}\right] \tag{3.29}$$

In Fig. 3.2. LJ potential vs. distance is given in reduced units. Eq. 3.24 is used with the argon parameters σ =3.4 and ε = 1.65. Equilibrium interseperation between the particles can also be deduced from the graph by finding the minimum value of potential.

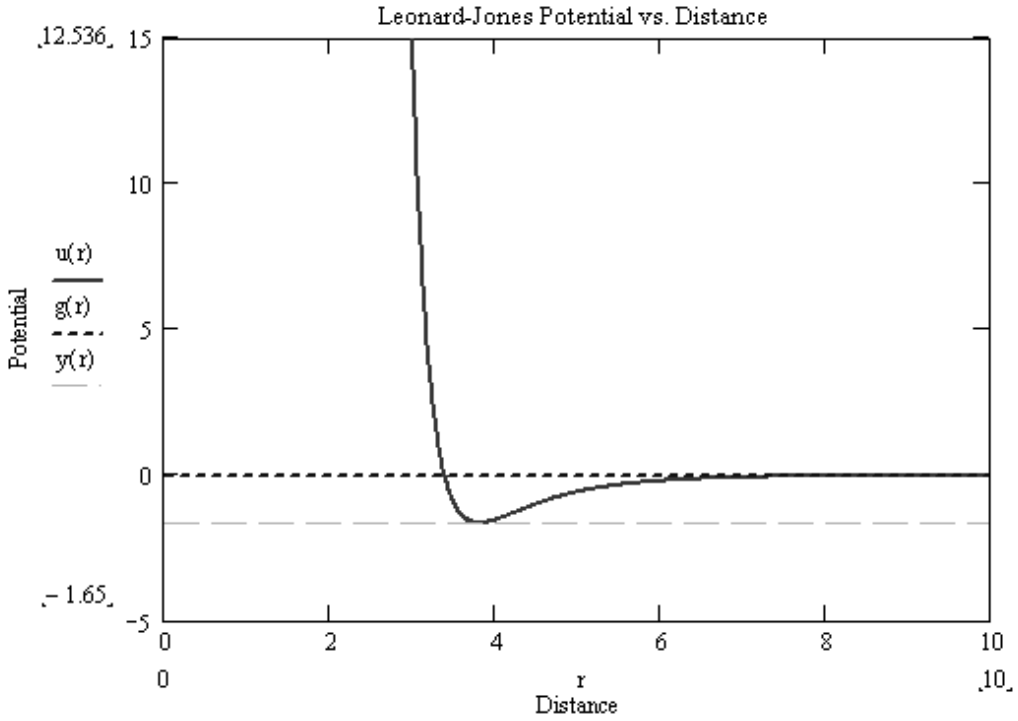

Figure 3.2 Interatomic potential vs. distance plot for argon.

3.2.1.4. Molecular dynamics program

A simple molecular dynamics program can be constructed by following the steps:

1. The initial parameters are specified in order to model the initial condition of the system (initial temperature, number of particles, density, and time step)
2. System is initialized, where the initial positions and initial velocities of atoms are defined.
3. Forces between the atoms are calculated.
4. Newton's laws of motion are integrated. This step and the previous one make the core of the simulation. They are repeated until the desired length of time.
5. After the completion of the central loop, computations of average quantities are carried out.

3.2.1.4.1 Initialization

In order to start a molecular dynamics simulation, initial positions and initial velocities should be assigned to all particles. The particle positions are usually chosen to be compatible with the structure that is aimed to simulate. In any event particles should not be positioned at positions that result in appreciable overlap of the atomic or molecular cores. This can be achieved by initially placing the particles periodic crystal lattice. However it is also possible to choose initial positions randomly but in this case a fictitious drag force should be included at the start of the simulation in order to dampen the high velocities due to intensive repulsive forces between too close atoms. This drag force is applied until all velocities come to tolerable values [62].

In general, the easiest way of obtaining an initial configuration with the desired configuration is to place particles a regular lattice. If temperature is high the system will melt and become a liquid or even gas. Otherwise it will remain solid. In addition to this, atomic movement can be easily traced when the starting point is a lattice.

The velocity component of each particle should also be attributed. This can be done by assigning random numbers to initial velocities from a meaningful interval. Standard random numbers are independent realization values of the random variable γ that is uniformly distributed in the interval $0 < x < 1$. Such numbers are necessary within molecular dynamics problems for assigning initial velocities. However, random variable γ is an ideal mathematical abstraction and trying to generate random numbers by deterministic methods is an exercise in futility. Nevertheless this effort is worthy to generate at least pseudo-random numbers with a prescribed formula that satisfy different requirements as if they were true random numbers [63].

There are several commonly used methods of pseudo-random number generation (PRNG), most of which are composed of recurrence relation and require a seed value. Linear congurentional randomizers are some of the most popular PRNGs. A linear congurentional generator is determined by [64]:

$$x_i = ax_{i-1} \bmod m \tag{3.30}$$

where x_i is the ith member of the sequence of pseudo-random numbers, x_0 being the seed, a is a multiplier, m is a nonzero modulus. As standard pseudo-random numbers, the fractions $\gamma_i = x_i/m$ are used [64]. The sequence is a periodic event where the period is maximum m. Therefore, large moduli are selected. In order to have an acceptable sequence, theoretical investigations are carried out for the decision of seed, a, m integer triplet [63].

After assigning random numbers, the velocities should be shifted such that total momentum of the system is equal to zero. Finally, the velocities should be scaled, where the velocities are adjusted such that the mean kinetic energy comes to a desired value. According to the kinetic theory:

$$k_b T = \frac{1}{dN} \sum_i m_i v_i^2 \tag{3.31}$$

where k_b is Boltzman constant, T is the absolute temperature, d is the degrees of freedom, N is the number of particles, m_i is the mass of atom i and v_i is the velocity vector of atom i. Thus by multiplying each velocity by an appropriate scaling factor, the initial temperature and mean initial kinetic energy can be adjusted.

3.2.1.4.2 Force Calculation

This is the most computationally expensive and time consuming part of the molecular dynamics simulation. Pairwise force calculations for each particle is

necessary. This means that for each time step calculation a total of N(N-1)/2 possible interactions should be considered. Dividing by two comes from Newton's third law. However because all kinds of interatomic potentials are converging to zero at high distances, the efficiency of the force calculations is increased considerably by assigning a cutoff distance for the force calculations. In this case interatomic potential at distances higher than a critical value (cutoff distance) are approximated to zero and this assumption does not contribute a significant error into overall calculations.

3.2.1.4.3 Integration

After the force calculations are completed the atomic positions are calculated in the integration step. Varying finite difference methods employing Taylor expansion series for numerical integration of Newton's equations are present in the literature. These methods, algorithms and comparisons between different methods can be found in related monograms [55, 59, 61]. Velocity Verlet algorithm which is used in this study is one of the integration methods where position and velocity vectors are calculated in the same time step. The related equations are:

$$r(t+\Delta t) = r(t) + v(t)\Delta t + 0.5a(t)\Delta t^2 \tag{3.32}$$

$$v(t+\Delta t) = v(t) + 0.5\big(a(t) + a(t+\Delta t)\big) \tag{3.33}$$

3.2.1.4.4 Boundary Conditions

In a sample of macroscopic size, only a very small fraction of the atoms are close enough to a wall to experience any deviation from the environment prevailing in the interior. However, in a computer simulation because the number of atoms is significantly small, surface effects are seriously high which makes the model far from resembling reality.

A system that is bounded but free of physical walls can be constructed by resorting to periodic boundary conditions. The introduction of periodic boundaries is equivalent to considering an infinite space filling array of identical copies of the simulation region. The two dimensional representation of the case is given in Fig. 3.3, the box labeled as E is the real simulation box where the other 8 boxes are the copies. There are two consequences of this periodicity. The first, is that an atom that leaves the simulation box through a particular bounding face immediately reenters through the opposite face. The second, is that atoms lying within a distance r_c of boundary interact with atoms in an adjacent copy of the system [61]. The second consequence, called the minimum image convention, is that sometimes a replicate image of an atom is used as an interaction partner for another atom. The position of any atom is checked and corrected if necessary according to periodic boundary conditions during integration. Minimum image convention is taken into account in force calculations when calculating the separation distance between any atom pairs.

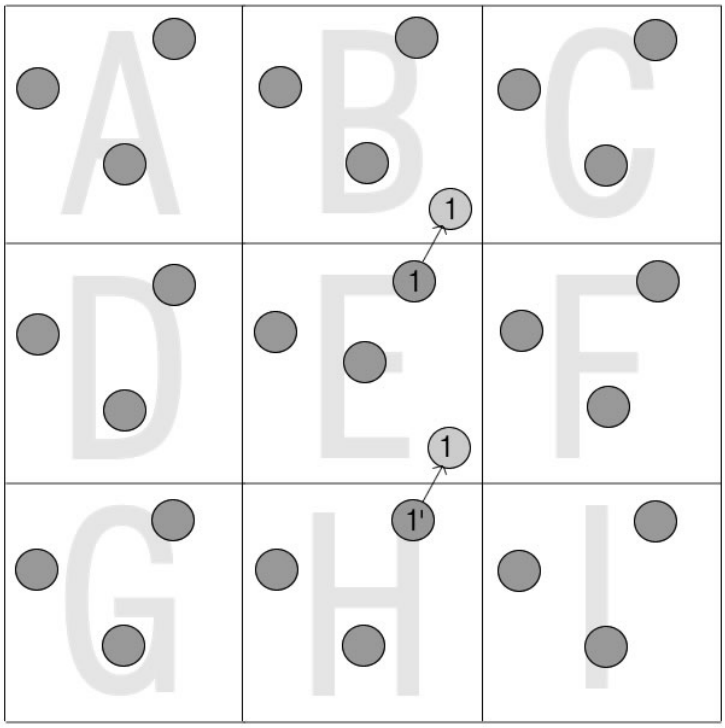

Figure 3.3 Two dimensional representation of periodic boundary conditions.

CHAPTER IV

EXPERIMENTAL PROCEDURE

This study consists of both theoretical and experimental parts. Simulation studies were also carried out with an interconnecting role between the theoretical and experimental tasks. Two systems were selected in order to investigate GFA. Zn-Mg system being one of the frontiers of metal-metal binary glasses was considered in order to investigate the Zn rich compositions. On the other hand Fe-B system being potential bearing for the production of BMGs with alloying additions was also selected to design new BMGs. In the theoretical branch interatomic potentials and ordering energies were calculated Zn-Mg and Fe-B binaries. For the systems considered the effect of the addition of a third element to ordering energy was investigated. Subsequently in the light of these results, MD simulations were carried out. In the experimental branch, centrifugal casting experiments and the characterization of the specimens produced were carried out for the Fe-B system. The theoretical findings form the basis of experimental work carried out.

4.1 THEORETICAL STUDIES

In this part of the study ordering energies between magnesium and zinc atoms in $MgZn_2$ phase and ordering energy between iron and boron atoms in Fe_3B phase were calculated according to the nearly one electron theory in pseudopotential approximation. Afterwards the variation of ordering energy between atoms in alloys with ternary alloying element additions to $MgZn_2$ and Fe_3B compositions were observed. All the calculations were done by utilizing computer programs Meh1, Meh2, Meh3, Meh7, Meh 71, Meh72, written by Hamdullah Mekhrabov,

which are available in Metallurgical and Materials Engineering Department. Ordering energies of the binary alloys were calculated by the Meh 7 program. After this calculation, the ordering energy values between different pairs of atoms in alloys with the addition of a third element were calculated for various alloying elements. Elements considered in the study were, Ag, Au, Zn, Cd, Hg, Sc, Y, La, Ti, Zr, Hf, V, Nb, Ta, Cr, Mo, W, Mn, Tc, Re, Fe, Ru, Os, Co, Rh, Ir, Ni, Pd, Pt, Li, Na, K, Rb, Cs, Be, Mg, Ca, Ba, Zn, Cd, Hg, Al, Ga, In, Tl, Si, Ge, Sn, Pb, As, Sb, Bi, Se, Te, Sr, B, C, P. For this purpose FORTRAN programs Meh1, Meh2, and Meh3 were used. For an A-B binary system where X denotes the ternary alloying element; Meh 1 program calculates the ordering energy between A and B atoms (W_{AB}), Meh2 program calculates the ordering energy between A and X atoms (W_{AX}), and Meh 3 program calculates the ordering energy between B and X atoms (W_{BX}).

From the outputs of the program runs, ordering energy can be read as a function of interatomic distance. In order to determine an exact value the liquid interatomic separation should be found and energy value should be extrapolated for this separation. For Fe_3B the distance between Fe and B atoms in the liquid phase was found from literature as 2.21 Å [65]. This corresponds to 4.1763 in atomic units. For the $MgZn_2$ intermetallic, interatomic distance data for liquid phase couldn't be found in literature and therefore the distance is approximated to the sum of atomic radii of Mg and Zn, which is 3.0075 Å [36]. This corresponds to 5.6612 in atomic units. When the ordering energies were calculated between one of the main elements and a ternary alloying addition element, interatomic distance was taken as the distance between the main elements which introduces another approximation.

Interatomic potentials for various atomic pairs were also calculated using the nearly one electron theory in the pseudopotential approximation.

4.2 MD SIMULATION

Simulation studies were carried out in order to determine atomistic insight about the motion of atoms during the rapid cooling from the liquid phase and the effect of ternary alloying additions to alloys. In addition to these, macroscopic thermodynamic parameters were intended to be explored. At this stage a main FORTRAN program was written in order to form the basis of simulation studies. FORTRAN language, which has been historically standard for scientific purposes, was chosen due to its high computational efficiency. Small auxiliary programs were written in MATHCAD because of the powerful visualization tools available within the program.

The program written for MD purposes consists of a main program and several subroutines. The code written is given in the Appendix A. The main program starts by determining initial parameters and creating output files. Afterwards subroutines *INITIAL_VELOCITIIES* and *FCC* were called for initialization. The KIND_DETERMINATION subroutine was used in various places to identify the types and masses of atoms. Initial interatomic forces were calculated by calling the *FORCE* subroutine and flowing the main loop, which performs Velocity Verlet type integration, starts within the main program for attaining the liquid structure of the alloy. Periodic boundary conditions were employed for the new coordinates. Force calculations were repeated at every time step. Temperature scaling was done inside the integration loop. Atomic positions, velocities and accelerations were recorded into relevant files. Also instantaneous temperature, kinetic energy and potential energy were monitored during integration. Translational order parameter and radial distribution functions (RDF) were also calculated during integration by calling the subroutines *ORDER* and *RADIAL_DIST_FNC.* After completing the first integration loop, the quenching phase begins by again performing the integration loop but this time temperature was constantly decreased by a specified rate to cool the alloy to room

temperature. The same kind of data which had been described previously was collected during the integration.

4.2.1 Initialization

In order to start the simulation problem the following should be prescribed:

- number of particles
- initial temperature and therefore kinetic energy
- initial coordinates and velocities of particles
- and time step for integration

In this study the number of particles was chosen as 864. This choice arises from optimization between execution time and resemblance to reality. As the number of atoms increases the approximation of simulation to reality increases, however at the same time execution time increases.

The objective of simulation was to perform rapid solidification from liquid state; therefore initial temperature was determined as the liquidus temperature of the system in concern. In order to determine the time step for integration, Eq. 4.1 deduced from conservation of total energy was used. In Eq. 4.1 m is the mass, r_0 is the equilibrium spacing and ε_0 is the equilibrium energy. In practice MD time step was taken as $\Delta t/100$ [66].

$$\Delta t = \sqrt{\frac{m r_0^2}{2\varepsilon_0}} \tag{4.1}$$

In this study time step was taken as 1.5 femto seconds for all simulations, which is much smaller than the values calculated using the above equation. Time step on the order of femto seconds granted further stability to the system. Initialization of positions and velocities will be discussed in the following sections.

4.2.1.1 Initial Velocities

In this study a linear congruential with a seed = 1, m=2^{40} and a=5^{17} triplet [63], was considered for random number generation. This sequence has a period of 2.75E11 which is extremely good enough for assigning initial velocities to 864 atoms.

A small program *RANDOR*, which is given below, is written in MathCAD for this purpose. It generates 3000 random numbers using the linear congurentional generator. The amount of random numbers can be increased by giving N greater numbers. However 2592 random numbers are sufficient for the three cartesian components of each of the velocity vectors for 864 atoms. Also partitioning of the kinetic energy equally among the cartesian coordinates was carried out by the small program *PARTITION*.

$$seed := 1$$

$$\begin{aligned} &Randor(seed) := \\ &\quad N \leftarrow 3000 \\ &\quad a \leftarrow 5^{17} \\ &\quad m \leftarrow 2^{49} \\ &\quad \text{for } i \in 1..N-1 \\ &\quad\quad rand_i \leftarrow \left(\frac{mod(seed \cdot a, m)}{m}\right) \\ &\quad\quad seed \leftarrow mod(seed \cdot a, m) \\ &\quad rand \leftarrow rand \cdot 2 - 1 \\ &\quad rand \end{aligned}$$

$$N := 1000$$

$$\begin{aligned} &program := \\ &\quad \text{for } i \in 0..N-1 \\ &\quad\quad x_i \leftarrow Randor(seed)_i \\ &\quad \text{for } i \in 0..N-1 \\ &\quad\quad y_i \leftarrow Randor(seed)_{i+1000} \\ &\quad \text{for } i \in 0..N-1 \\ &\quad\quad z_i \leftarrow Randor(seed)_{i+2000} \\ &\quad \begin{pmatrix} x \\ y \\ z \end{pmatrix} \end{aligned}$$

$$x := program_0 \qquad y := program_1 \qquad z := program_2$$

$$\text{partition} := \left| \begin{array}{l} \text{for } i \in 0..N-1 \\ \quad \left| \begin{array}{l} x_i \leftarrow \dfrac{x_i}{\sqrt{(x_i)^2 + (y_i)^2 + (z_i)^2}} \\ y_i \leftarrow \dfrac{y_i}{\sqrt{(x_i)^2 + (y_i)^2 + (z_i)^2}} \\ z_i \leftarrow \dfrac{z_i}{\sqrt{(x_i)^2 + (y_i)^2 + (z_i)^2}} \end{array} \right. \\ \begin{pmatrix} x \\ y \\ z \end{pmatrix} \end{array} \right.$$

$x := \text{partition}_0 \qquad y := \text{partition}_1 \qquad z := \text{partition}_2$

Before going further, the randomness of the numbers series was tested by a program written in MATHCAD. First a standard hit and miss test [55] was conducted. This can be done by calculating the area (π) of a circle with unit radius. The circle was centered at the origin and inscribed in a square given in Fig.4.1. 1500 trial shots were generated in the square. At each trial two random numbers generated by *RANDOR* were used as x and y coordinates of a trial point. The distance from the random point to the origin was calculated. If the distance is less than or equal to one, the shot has landed in the circle and hit is scored. If totally N shots are fired and N_{hit} are scored and if the numbers are totally random, the area ratio between the circle and square will be equal to ratio of hit to miss for a large number of trials: $\pi = \dfrac{4 \times Area_{quartercircle}}{Area_{square}} = \dfrac{4N_{hit}}{N}$

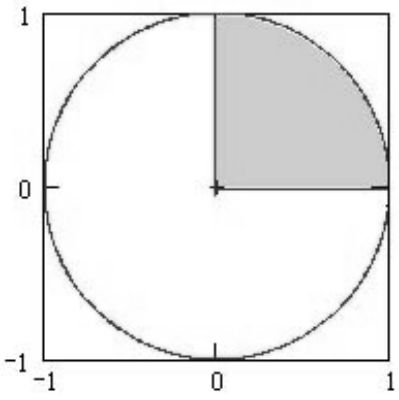

Figure 4.1 Standard hit and miss test circle

Therefore calculating the hit to miss ratio and plotting it versus number of trials will be a good measure of random series' efficiency. The convergence of amplitude of the graph to the number π is a qualitative criterion of the randomness of the numbers used for a random series. This behavior can be observed in Fig. 4.2.

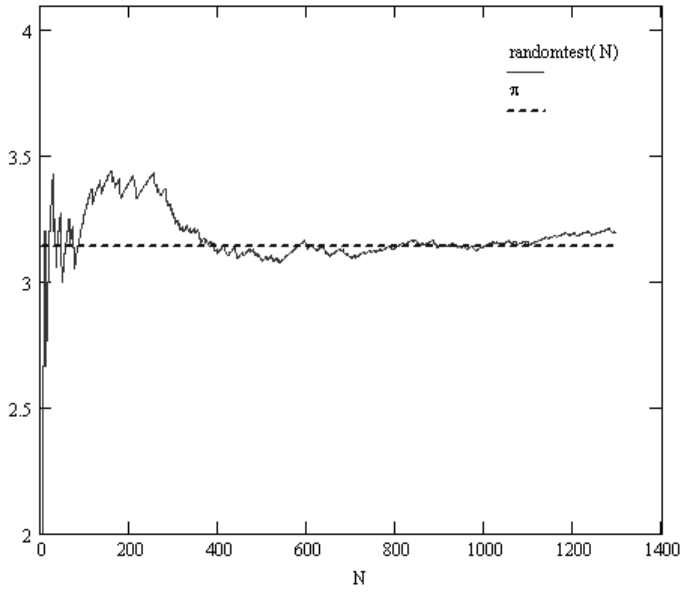

Figure 4.2 Hit miss ratio vs. Number of trials

In addition to this, when the numbers generated are taken as successive pairs (x,y) and successive triplets (x,y,z), they should define randomly distributed points in unit square and unit cube respectively. The distribution of the points in unit cube is given in Fig. 4.3., no pattern or regularity can be observed in these visualizations.

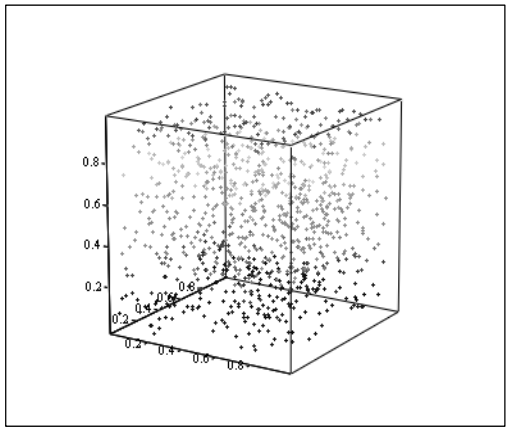

Figure 4.3 Random distribution of point in unit cube.

Afterwards the numbers tested were exported to text files and were read by the subroutine *INITIAL_VELOCITIES* of the main program. In the subroutine, firstly the net momentum per atom in x, y, and z axises were calculated and this net momentum was subtracted from each atom, in order to nullify the net momentum in the system. Following that, the velocities were scaled for the initial temperature. This was done by using the kinetic definition of the temperature. The scaling factor β should be determined. The system has 3N degrees of freedom, imposing total momentum to be zero removes 3 degrees of freedom while having the total kinetic energy to be constant removes another 1 degree of freedom. However, for simplicity these factors were neglected and degrees of freedom was taken as 3N. Then the scaling factor becomes:

$$\beta = \left[\frac{3Nk_b T_{ref}}{\sum_i m_i v_i} \right] \tag{4.2}$$

For scaling, each velocity component was multiplied with β and the initial velocity matrix was attained.

4.2.1.2 Initial Positions

Before giving the start up to the simulation, atoms were located to face centered cubic lattice (fcc) by the subroutine *FCC*. This task was done by forming a loop for generating periodic atom positions using the origin (0,0,0) and equivalent positions (0,1/2,1/2; 1/2,0,1/2; 0,1/2,1/2) of fcc lattice The initial crystal lattice can be seen in Fig. 4.4. The positions written into a text file were read by the main program.

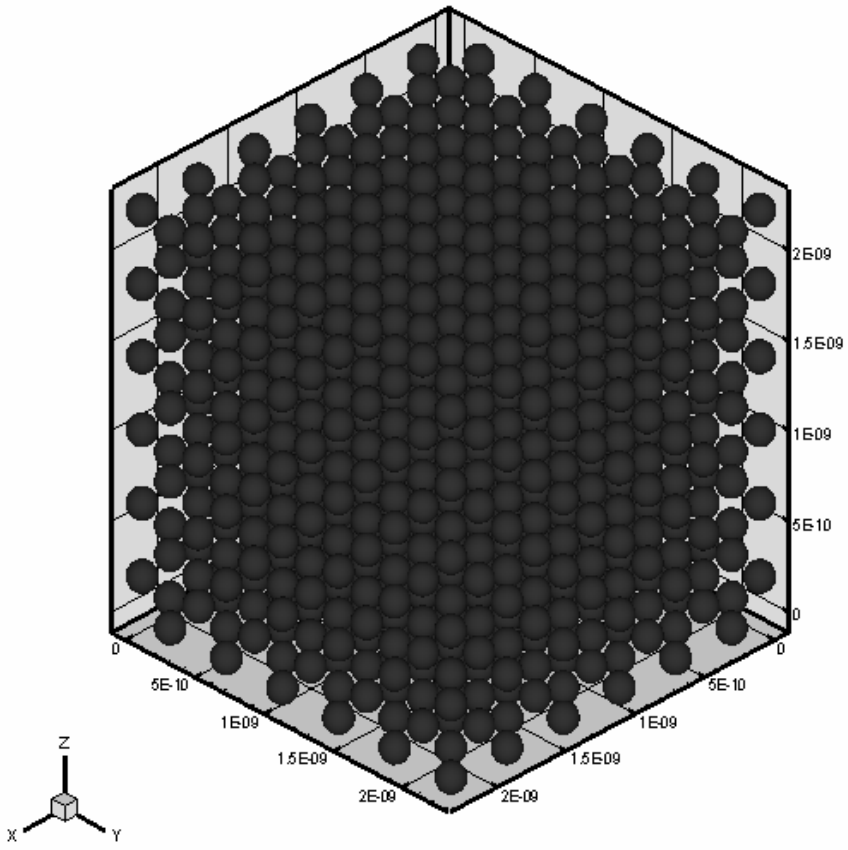

Figure 4.4 Initial fcc lattice constructed**.**

4.2.2 Force Calculation

Force calculation is a routine task which should be carried out in each step of numerical integration. The subroutine *FORCE* at any time step calculates the distance between all atoms, calls *kind_determination* subroutine in order to identify the types of atoms, modifies the interatomic distances according to the minimum image convention and finally calls the force functions for appropriate atomic interaction to calculate the potential and force between these atoms.

4.3 CASTING EXPERIMENTS

4.3.1 Alloy Selection

The Fe-B system has been studied intensively for metallic glasses. Especially the eutectic composition namely 83% Fe-17% B has been a focus. On the other hand one of the constituents of the eutectic reaction Fe_3B is a metastable intermetallic phase which can also be a potential candidate to form metallic glasses with other alloying additions. Fe_3B being a facet forming intermetallic encounters crystal growth problems and with alloying additives complex solidification behavior can be induced. Under rapid solidification conditions this can yield a BGFA where alloying elements which increase the ordering tendency are selected to modify the composition. Binary to quinary alloys were produced during the course of this study. Alloys which are beneficial to the discussion of GFA are given. The compositions of these alloys are given in table 4.1.

Table 4.1 Composition and crucibles used for the alloys produced**.**

Designation	Composition in atomic percent	Crucible
C1	$Fe_{75}B_{25}$	Alumina Based
C2	$Fe_{75}B_{25}$	Alumina based
C4	$Fe_{63}B_{21}Mo_{16}$	Alumina based
C6	$Fe_{63}B_{21}Mo_{14}W_{7}$	Alumina based
C9	$Fe_{62}B_{21}Mo_{5}W_{2}Zr_{10}$	Alumina based
C10	$Fe_{62}B_{21}Mo_{5}W_{2}Zr_{10}$	Silica based

4.3.2 Alloy Preparation

Industrial ferroboron which is commercially available was used as a master alloy. High purity elements were used during the alloy preparation step to modify the composition of master alloy. The chemical composition of the ferroboron used is given in table 4.2. Ferroboron used was in lump form with 10 to 50 mm in size and it was crushed to smaller pieces when used for alloy preparation.

Table 4.2 Composition of industrial ferroboron

Element	weight %
Fe	80,248
B	18,49
Al	0,088
Si	0,79
C	0,35
P	0,03
S	0,004

Other elements used during the experimental studies were, crystalline boron with 99.9% purity, iron pieces with 99.97+% purity, tungsten rods with 99.9% purity, molybdenum pellets with 99.7% purity and pure zirconium lumps with 99.8%

purity in metallic basis. All the elements were cut and/or crushed into smaller pieces in order to attain high homogeneity in the alloys prepared.

4.3.3 Copper Molds

For casting processes wedge shaped copper molds with different cavity dimensions were used. The schematic drawing is given in Fig. 4.5. Copper, owing to its high thermal conductivity (3.98 watt/cm.K), enables rapid solidification of the melt. On the other hand, the wedge shaped geometry enables it to have different cooling rates along the wedge direction. The highest cooling rate is attained in the thinnest section and the slowest cooling rate is attained in the thickest section. Before the casting experiments, the molds are cooled to 0 ^{0}C in order to enable higher cooling rates.

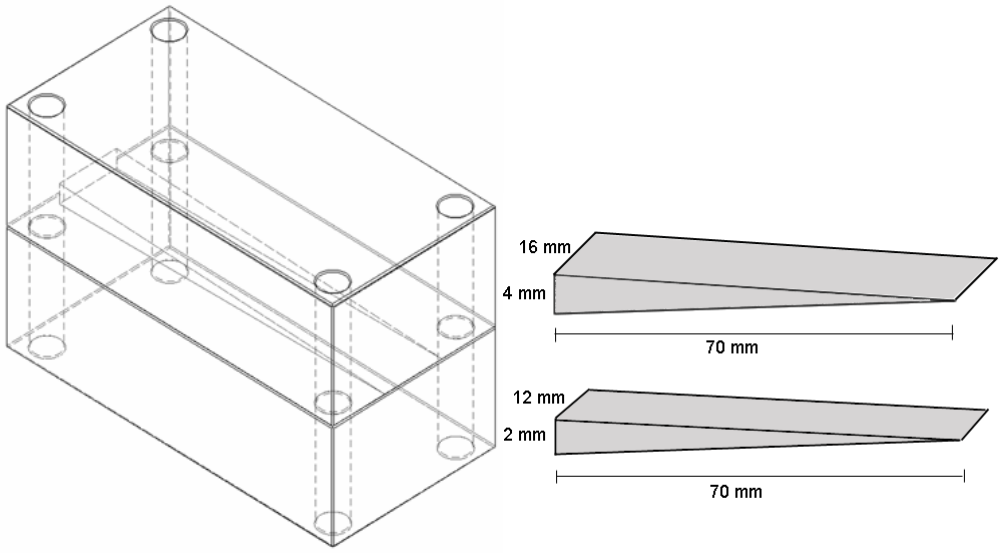

Figure 4.5 Schematic drawing of copper mold

4.3.4 Crucible Production

Ceramic alumina and silica crucibles in conical geometry were used for melting the alloy in the centrifugal casting machine. The drawing of the crucible is given in Fig.4.6. The alumina crucibles were synthesized, while the silica crucibles used were commercial products for jewelry castings. In order to synthesize crucibles Metacast-K97/MA alumina plaster was used. Alumina plaster has a particle size between 0 and 5 mm and has the chemical analysis given in Table 4.3. Alumina becomes the choice because its inert character, which enables nearly contamination free melting processes and high temperature resistance which enables melting of alloys with high liquidus temperature.

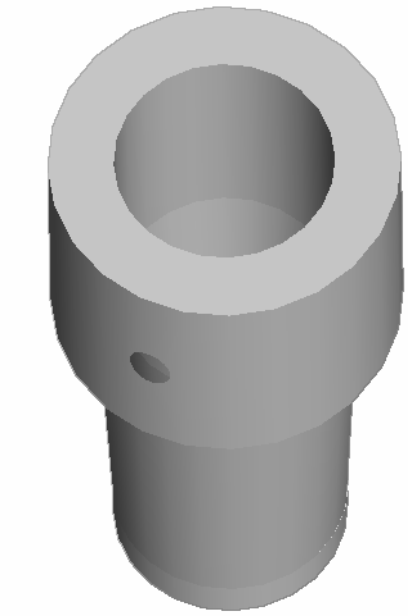

Figure 4.6 Drawing of the alumina crucibles used for casting.

Table 4.3 Chemical analysis of the Alumina plaster.

Compounds	Weight percentage
Al_2O_3	approx. 97.0
SiO_2	max. 0.2
Fe_2O_3	max. 0.1
CaO	max. 1.6

Plaster was mixed with the appropriate amount of water and casted into steel dies with conical geometry. Following air drying for 24 hours, sintering heat treatment was applied for the ceramic to gain strength. The temperature program of the heat treatment is given in the below graph. During the casting experiments crucibles should withstand temperature fluctuations; therefore thermal shock resistance is of great importance. To gain a high thermal shock resistance, alumina powder with a wide particle size distribution was used.

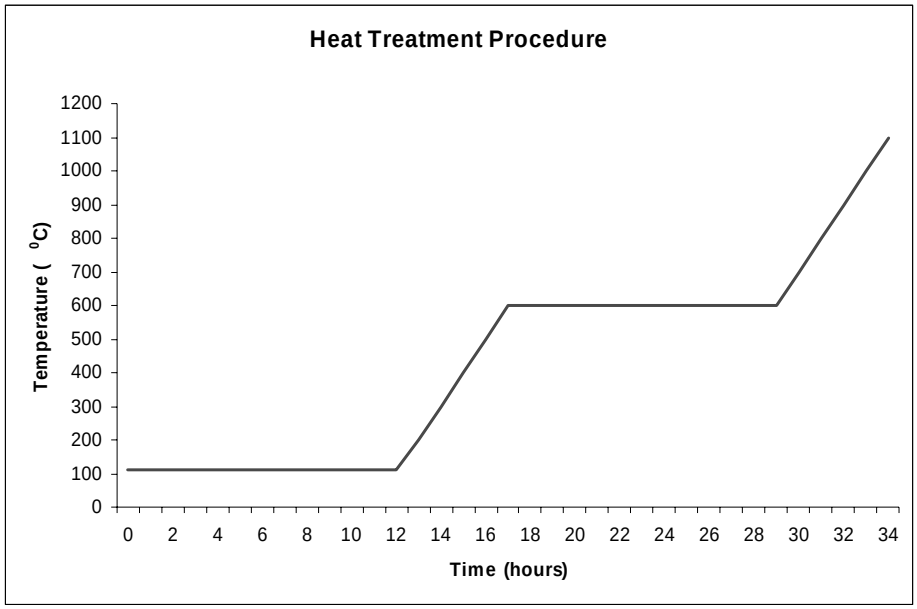

Figure 4.7 Sintering heat treatment program.

4.3.5 Melting and Casting

Melting and centrifugal castings were carried out using the Multihertz neutromag digital induction casting machine. Melting was done by induction heating of the alloy constituents in crucibles. Atmosphere control was accomplished by first applying a vacuum and afterwards flushing spectrometric argon gas into the system. Temperatures up to 2000 ^{0}C can be reached. Temperature control was attained by the pyrometer. However, pyrometer measurements are sensitive above 800 ^{0}C.

After the melting of alloy constituents, the alumina crucible with the opening directed to a wedge shaped copper mold, which are both fixed on the main arm of the machine are rotated at high speed and with the aid of centrifugal force the metallic melt is injected into the copper mold, where it solidifies rapidly.

4.3.6 Characterization of the Specimens

For characterization studies differential scanning calorimetry, X-ray diffraction and scanning electron microscopy were employed.

4.3.6.1 Thermal Analysis

Setaram SETSYS TGA-(DTA/DSC) thermal analyzer with facilities for simultaneous TGA and DTA/DSC measurements was used for thermal analysis of the specimens. For all alloys, small specimens around 25 mg were heated above the melting point of the alloy in an argon atmosphere in a crucible simultaneously with a blank sample crucible. Scanning rate of 20 ^{0}C/min was used. Heat flow and temperature signals were obtained via computer and software integrated with the DSC system. By analyzing heat flow vs. temperature graph, the glass transition temperature can be determined, if exists due to specific

endothermic relaxation shape. Crystallization temperature, other phase transformations and the enthalpy changes accompanying these transformations were calculated.

4.3.6.2 Microstructural Investigations

Firstly, metallographic specimen preparation was performed. From the wedge shaped as cast pieces, sections with varying cooling rate were mechanically cut and mounted into bakelite by mount press at 140 ^{0}C and 4000 psi. Grinding was carried out by 200, 400, 600, 800, 1200 SiC emery papers respectively in rotating discs. In order to attain scratch free surfaces polishing with diamond paste and alumina was performed step by step. Etchants 2% nital and 5% nital were used for finalizing preparation.

Optical observations were carried out with Nikon Optihot microscope. SEM investigations were carried out with JSM-6400 Electron Microscope (JEOL), equipped with NORAN System 6 X-ray Microanalysis System & Semafore Digitizer. Both secondary electron images and energy dispersive analysis (EDS) were taken with the SEM facilities.

4.3.6.3 X-Ray Diffraction

X-ray diffraction studies were carried out with a 100 kV Philips twin tube X-ray diffractometer (PW/1050). Cobalt K_α (λ = 1.79026 Å) radiation was used as the incident beam. Diffractogrammes with diffraction angles (2θ) between 20^0 to 100^0 were obtained for all specimens. The experimental parameters used for all investigations were fixed to 30 kV voltage 8 mA current, 400 cps, 1^0/minute speed for vigorous comparisons. From the diffractogrammes, 2θ values of peaks were identified and the phases present were explored accordingly, using the computer software PCPDFWIN.

4.3.6.4 Hardness Measurements

For the binary, alloy hardness test through out the wedge direction was carried out. EMCO Universal Hardness Testing machine was used. Measurements were carried out with Vickers indenter under 30 kgs load.

CHAPTER V

RESULTS AND DISCUSSION

Results obtained in this study will be given and discussed in three sections. These sections are theoretical calculations, simulation results and casting experiments.

5.1 THEORETICAL CALCULATIONS

5.1.1 Interatomic Interaction Potentials:

According to the equations 3.1 to 3.17 results, of the interatomic interaction potentials for the Zn-Mg, Mg-Mg, Zn-Zn, Fe-B, Fe-Fe and B-B pairs of atoms, interactions were calculated for different interatomic spacings by using computer programs, Meh7, Meh71 and Meh72. The results of Zn-Mg and Fe-B were plot as examples in Fig. 5.1. and Fig. 5.2. However, because an analytical form of the potential was needed, DataFit software was used to fit the data into a tenth order polynomial.

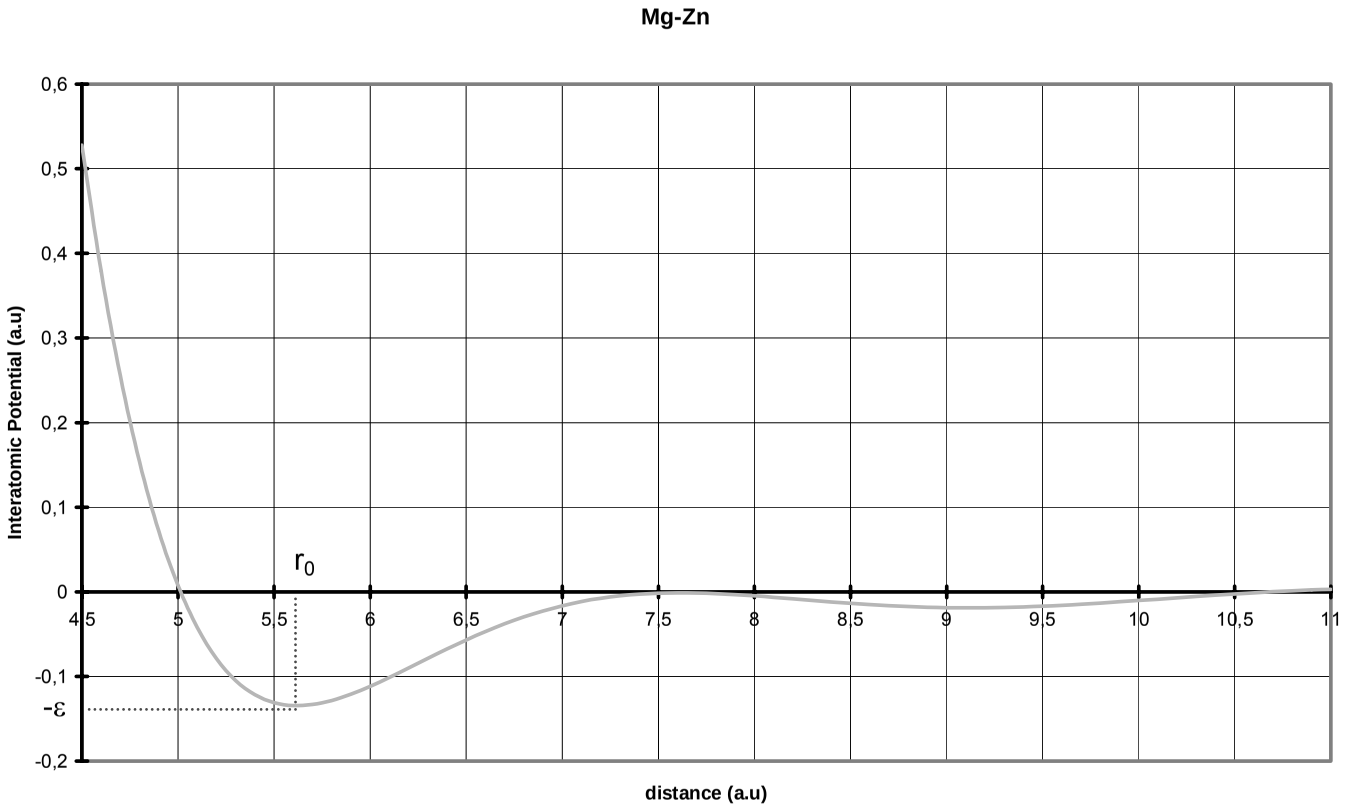

Figure 5.1 Interatomic interaction potential between Mg-Zn pairs of atoms (1 a.u(energy) = 2 Ry = 27.2 eV; 1.a.u(length) = 0.529177 Å).

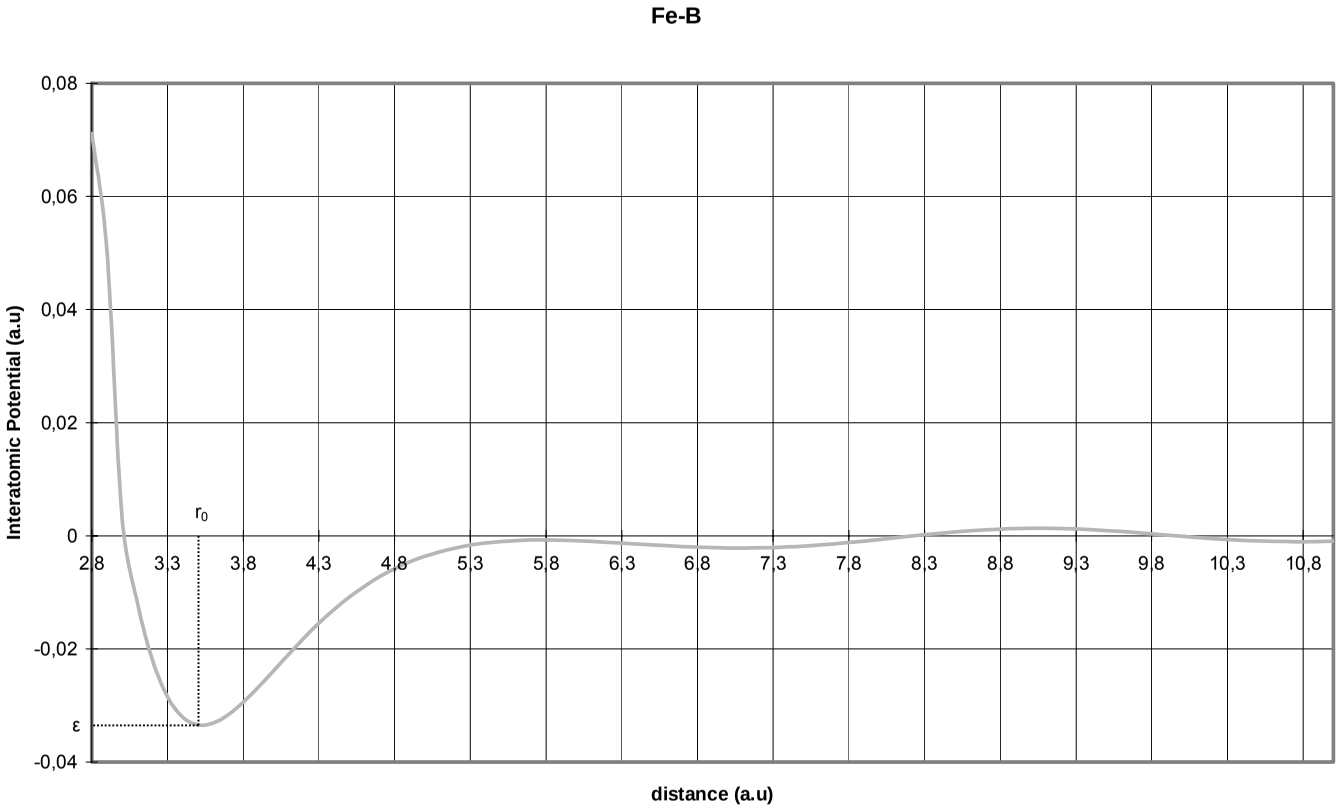

Figure 5.2 Interatomic interaction potential between Fe-B pairs of atoms

(1 a.u(energy) = 2 Ry = 27.2 eV; 1.a.u(length) = 0.529177 Å).

5.1.2 Ordering Energy Calculations

5.1.2.1 Ordering Energy Calculations for $MgZn_2$

The results of ordering energy calculations are given for the $MgZn_2$ intermetallic composition. The ordering energy between Mg and Zn atoms is shown as $W_{Mg\text{-}Zn}$, the ordering energy between the Mg and third element is shown as $W_{Mg\text{-}X}$ and ordering energy between Zn and third element is shown as $W_{Zn\text{-}X}$. The energy values are given in atomic units. In Table 5.2 the calculations were carried out for 2 at. % third element replacement in place of iron, while in the Table 5.3. calculations were done with replacing 2 at. % boron atoms with the third element specified.

Table 5.2 Results of ordering energy calculations for $Mg_{31}Zn_{67}X_2$

$Mg_{31}Zn_{67}X_2$							
X	W_{Mg-Zn}	W_{Mg-X}	W_{Zn-X}		W_{Mg-Zn}	W_{Mg-X}	W_{Zn-X}
$MgZn_2$	0,00153	-	-	**Nb**	0,00138	0,00015	-0,00112
Ag	0,00155	-0,00298	-0,00079	**Ni**	0,00148	-0,00018	0,00005
As	0,00140	0,00524	-0,00078	**Os**	0,00141	0,00412	0,00377
Au	0,00155	-0,00260	-0,00445	**P**	0,00140	0,00093	-0,00609
Ba	0,00171	0,15663	0,20574	**Pb**	0,00148	0,00633	0,00616
Bi	0,00147	0,01433	0,01258	**Pd**	0,00149	-0,00299	0,00240
C	0,00137	0,00546	-0,00048	**Pt**	0,00150	0,00744	0,00106
Ca	0,00163	0,02380	0,04022	**Rb**	0,00184	0,03706	0,06643
Cd	0,00153	0,00154	-0,00015	**Re**	0,00128	0,04705	-0,00958
Co	0,00148	-0,00017	0,00006	**Rh**	0,00145	0,00145	0,00151
Cr	0,00144	-0,00128	-0,00149	**Ru**	0,00140	0,00347	0,00369
Cs	0,00193	0,03319	0,07072	**Sb**	0,00144	0,00351	0,00135
Cu	0,00152	-0,00252	-0,00029	**Sc**	0,00150	-0,00004	-0,00035
Ge	0,00145	0,00083	-0,00215	**Si**	0,00144	-0,00007	-0,00368
Hf	0,00145	0,00405	0,00389	**Sn**	0,00147	0,00185	0,00130
Fe	0,00144	-0,00020	-0,00053	**Sr**	0,00168	0,06344	0,09166
Hg	0,00154	0,00666	0,00061	**Ta**	0,00138	-0,00013	-0,00180
In	0,00151	0,00380	0,00263	**Tc**	0,00128	-0,00011	0,00095
Ir	0,00141	0,00412	0,00378	**Te**	0,00142	-0,00157	-0,00544
K	0,00178	0,02244	0,04201	**Ti**	0,00142	0,00181	-0,00232
La	0,00156	0,00281	0,00299	**Tl**	0,00152	0,00508	0,00324
Li	0,00157	0,00115	-0,00166	**V**	0,00136	-0,00404	-0,00741
Mn	0,00148	-0,00023	0,00073	**W**	0,00133	0,00184	-0,00025
Mo	0,00133	0,00040	-0,00282	**Y**	0,00154	0,00135	0,00190
Na	0,00164	0,00137	0,00682	**Zr**	0,00145	0,00342	0,00389

Table 5.3 Results of ordering energy calculations for $Mg_{31}Zn_{67}X_2$.

$Mg_{33}Zn_{65}X_2$							
X	W_{Mg-Zn}	W_{Mg-X}	W_{Zn-X}		W_{Mg-Zn}	W_{Mg-X}	W_{Zn-X}
$MgZn_2$	0,00153	-	-	**Nb**	0,00142	0,00005	-0,00103
Ag	0,00158	-0,00302	-0,00084	**Ni**	0,00151	-0,00014	0,00005
As	0,00144	0,00521	-0,00085	**Os**	0,00145	0,00401	0,00380
Au	0,00158	-0,00280	-0,00460	**P**	0,00144	0,00090	-0,00616
Ba	0,00174	0,15345	0,20275	**Pb**	0,00152	0,00635	0,00614
Bi	0,00150	0,01427	0,01249	**Pd**	0,00153	-0,00305	0,00402
C	0,00140	0,00566	-0,00045	**Pt**	0,00153	0,00743	0,00102
Ca	0,00166	0,00335	0,04017	**Rb**	0,00187	0,03585	0,06536
Cd	0,00156	0,00155	-0,00015	**Re**	0,00132	-0,00540	-0,00962
Co	0,00152	-0,00013	0,00005	**Rh**	0,00149	0,00137	0,00157
Cr	0,00148	-0,00123	-0,00152	**Ru**	0,00144	0,00338	0,00377
Cs	0,00195	0,03143	0,06916	**Sb**	0,00148	0,00347	0,00132
Cu	0,00156	-0,00253	-0,00031	**Sc**	0,00154	0,00002	-0,00035
Ge	0,00149	-0,00540	-0,00216	**Si**	0,00147	-0,00008	-0,00369
Hf	0,00148	0,00394	0,00392	**Sn**	0,00151	0,00184	0,00130
Fe	0,00148	-0,00014	-0,00054	**Sr**	0,00171	0,06253	0,09095
Hg	0,00157	0,00664	0,00057	**Ta**	0,00142	-0,00025	-0,00173
In	0,00154	0,00378	0,00260	**Tc**	0,00132	-0,00014	0,00103
Ir	0,00145	0,00400	0,00380	**Te**	0,00146	-0,00164	-0,00550
K	0,00181	0,02193	0,04159	**Ti**	0,00146	0,00186	-0,00234
La	0,00159	0,00272	0,00301	**Tl**	0,00155	0,00511	0,00322
Li	0,00160	0,00113	-0,00166	**V**	0,00140	-0,00394	-0,00743
Mn	0,00152	-0,00020	0,00072	**W**	0,00137	0,00168	-0,00023
Mo	0,00137	0,00019	-0,00284	**Y**	0,00157	0,00128	0,00197
Na	0,00167	0,00134	0,00681	**Zr**	0,00149	0,00333	0,00399

Percent change in W_{Mg-Zn} due to presence of a third element was also calculated for the different alloying elements. The results are shown in Fig. 5.3 and Fig. 5.4 From the results it can be seen that Ag, Au, Ba, Ca, Hg, Cs, K, La, Li, Na, Rb, Sr and Y elements are increasing the ordering tendency between magnesium and zinc atoms when 2% magnesium is replaced with one of the elements specified. Whilst, when the alloying addition was done by replacing 2% Zn in addition to elements which are given for the $Mg_{31}Zn_{67}X_2$ composition Cd, Cu, Hg , In, Sc and Tl are also beneficial for increasing the ordering tendency between

magnesium and zinc atoms. The elements that increase the ordering energy are represented on the periodic table in Fig. 5.5. Most of these elements are group 1A and 2A elements. Apart from that 1A and 2A elements, are the ones with more impact on the ordering energies. For example Cs causes nearly 26% increase. Where the ordering energies between the main constituents and third elements are concerned, Ba has an intensive increasing effect. These results correlate well with the experimental founding in the literature [67,68]. GFA compositions according to these results can be designed. However, two obstacles are present, one of them is alkali and alkali-earth elements being quite reactive, such as even the humidity in the air can trigger reactions involving them; so alloy preparation is compulsory and severe differences between nominal and real compositions may arise. The other obstacle is the melting temperature of the compositions for Mg-Zn system is rather low, changing between 350-700 ^{0}C. T_{rg} values are therefore low as a consequence of this. For these reasons the Mg-Zn system was excluded from the casting experiments part of the study. In the literature no bulk amorphous alloy synthesized from Mg-Zn was reported. However, GFA ability of Mg-Zn alloys were investigated and amorphous phase formation was reported by melt spinning techniques in the literature [69, 70].

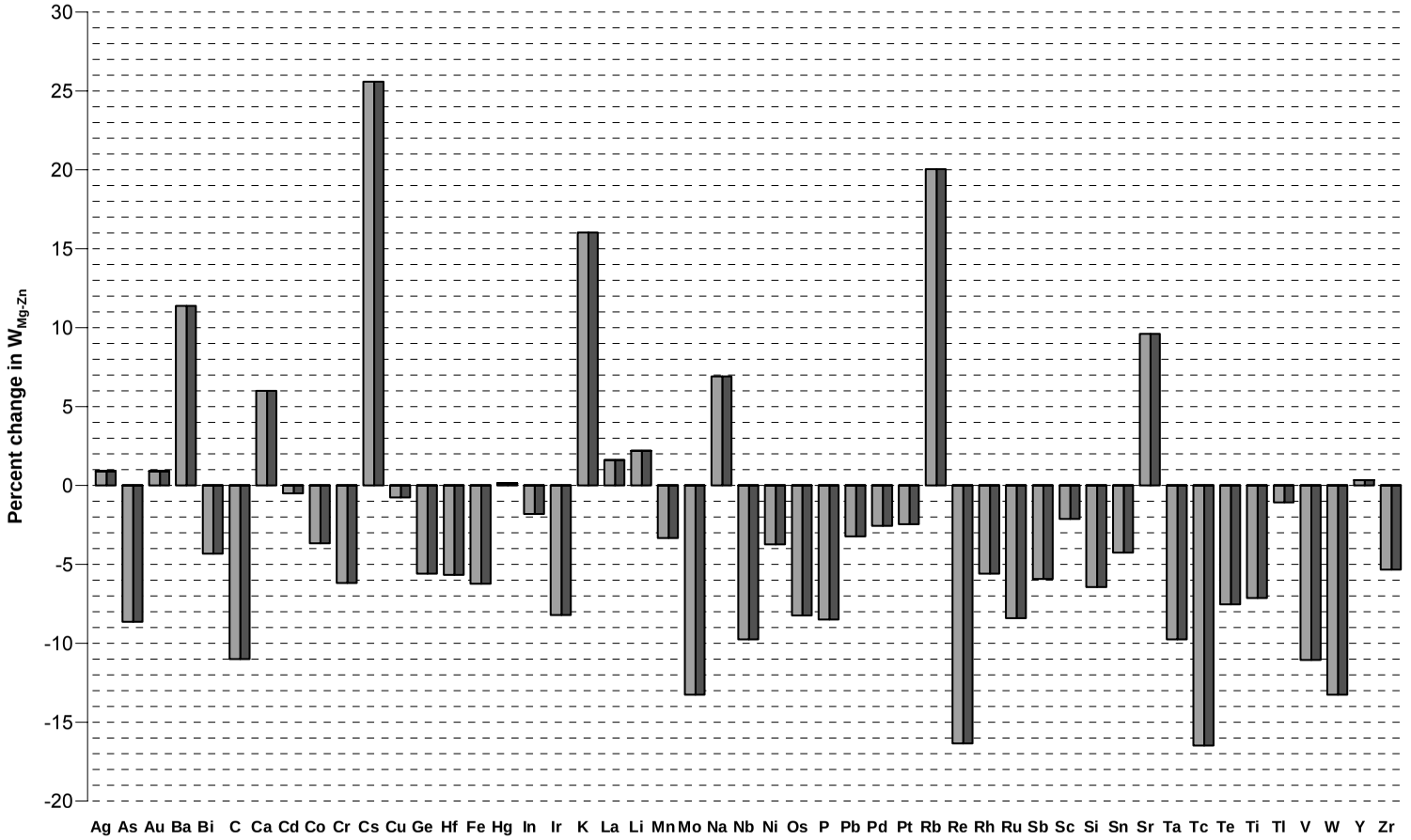

Figure 5.3 Percent change in W_{Mg-Zn} due to addition of 2 at. % third element in place of Mg

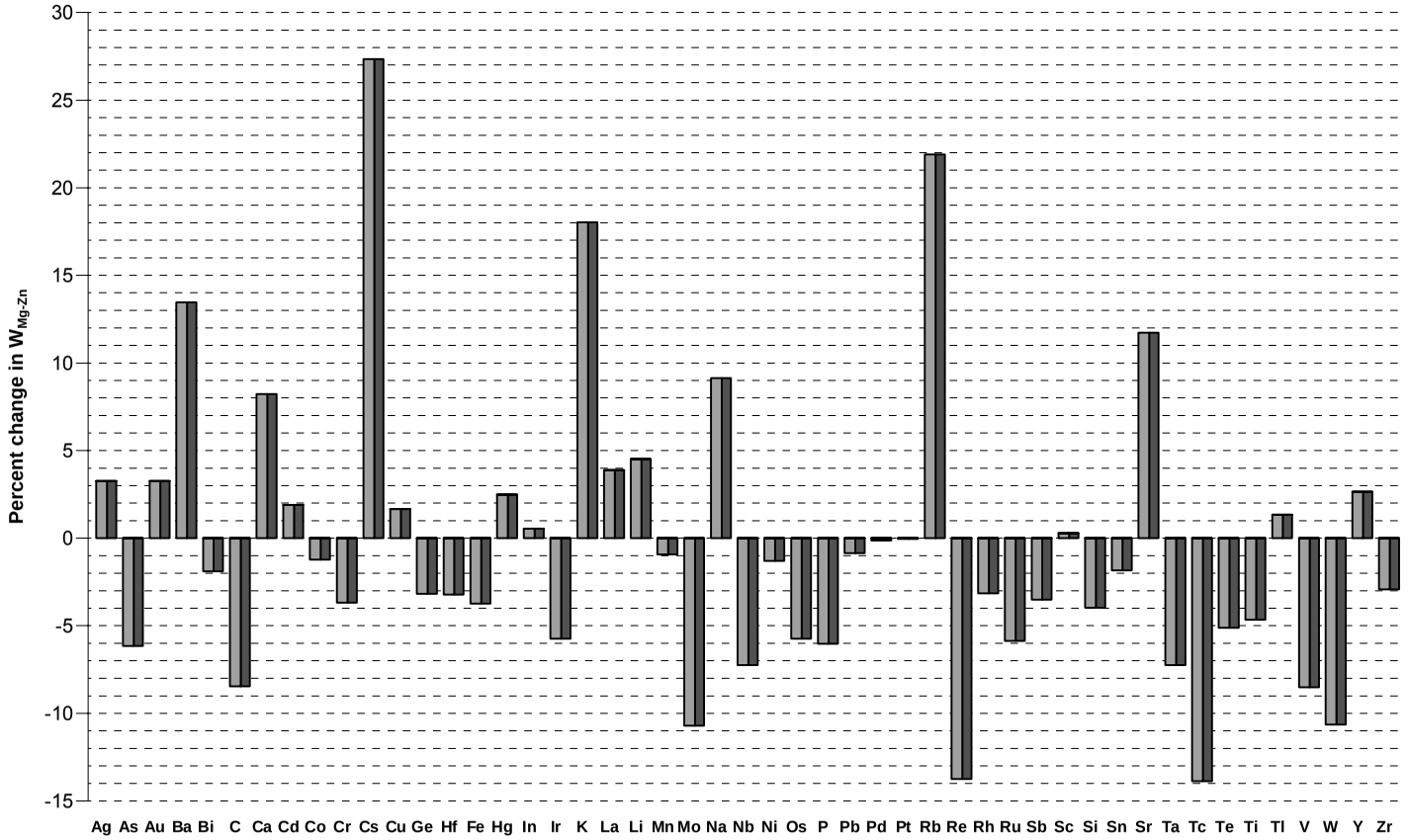

Figure 5.4 Percent change in W_{Mg-Zn} due to addition of 2 at. % third element in place of Zn

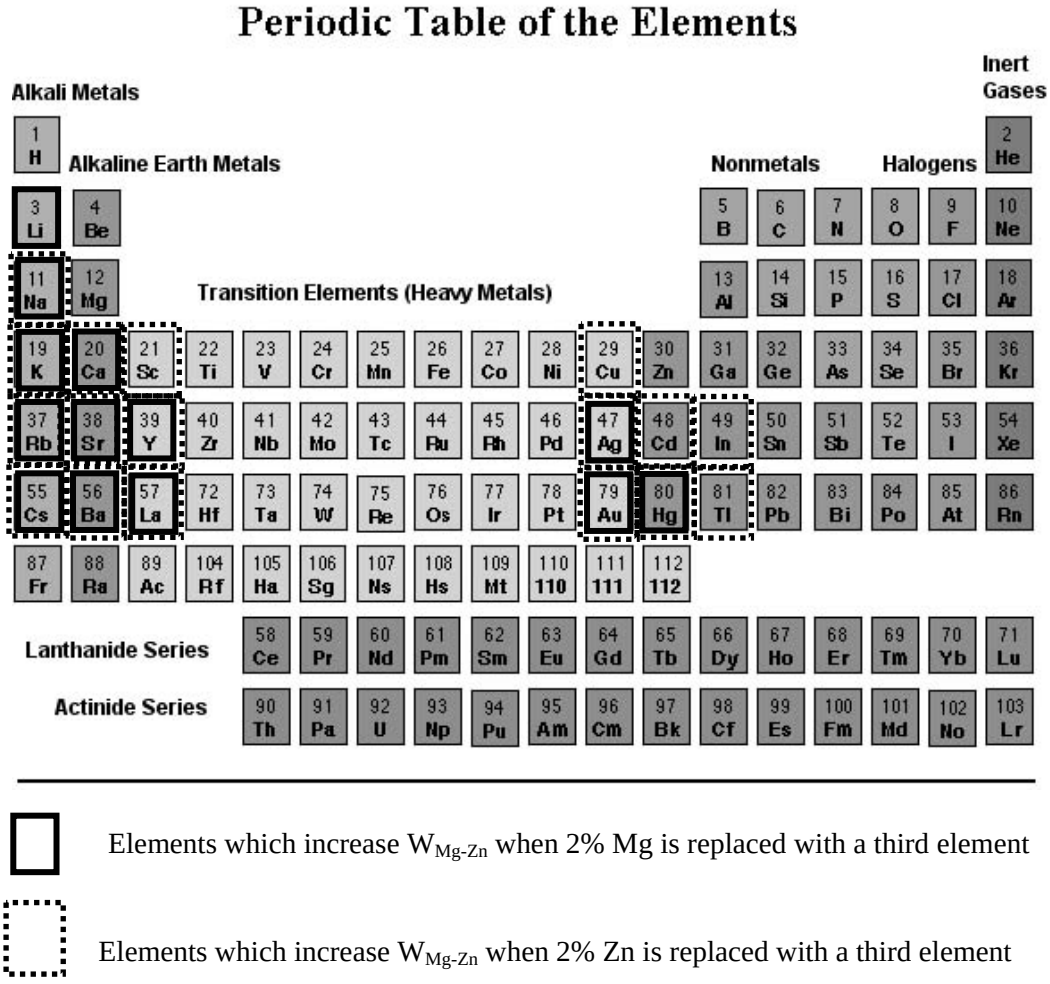

Fig. 5.5 The representation of elements which increase the W_{Mg-Zn} on periodic table

5.1.2.2 Ordering Energy Calculations for Fe_3B

The results of ordering energy calculations are given for the Fe_3B intermetallic composition. The data is given as three columns, similar to the previous tables and the energy values are given in atomic units. In Table 5.4 the calculations were carried out for 2% third element replacement in place of iron, while in Table

5.5 the calculations were done with replacing 2% boron atoms with the third element specified.

Table 5.4 The ordering energy calculations for $Fe_{73}B_{25}X_2$

$Fe_{73}B_{25}X_2$							
X	**W_{Fe-B}**	**W_{Fe-X}**	**W_{B-X}**		**W_{Fe-B}**	**W_{Fe-X}**	**W_{B-X}**
Fe3B	0,04969	-	-	**Ni**	0,04938	0,00408	0,03131
Ag	0,04831	-0,02581	-0,00457	**Os**	0,04982	0,04121	0,20136
As	0,04935	0,01580	0,08197	**P**	0,04930	-0,02240	0,04248
Au	0,04834	-0,02633	-0,01041	**Pb**	0,04804	0,03316	0,11305
Ba	0,04404	0,19521	0,43120	**Pd**	0,04895	0,00282	0,07485
Bi	0,04785	0,09669	0,19080	**Pt**	0,04891	0,00274	0,00722
C	0,05076	0,02944	-0,00373	**Rb**	0,04152	-0,03638	-0,00114
Ca	0,04589	0,21336	0,40658	**Re**	0,05092	0,09980	0,34537
Cd	0,04822	-0,00171	0,03793	**Rh**	0,04946	0,01218	0,14504
Co	0,04936	0,00396	0,03170	**Ru**	0,04987	0,05161	0,23434
Cr	0,04966	0,00117	0,05499	**Sb**	0,04840	0,03507	0,15356
Cs	0,03812	-0,09599	-0,08169	**Sc**	0,04821	-0,00001	0,04841
Cu	0,04889	-0,00722	0,01302	**Si**	0,04913	-0,01187	0,06486
Ge	0,04885	-0,00410	0,07357	**Sn**	0,04838	0,01418	0,12055
Hf	0,04890	0,04178	0,20330	**Sr**	0,04464	0,11237	0,28352
Hg	0,04802	-0,00123	0,01098	**Ta**	0,04977	0,05856	0,26423
In	0,04811	0,00115	0,06774	**Tc**	0,05097	0,16576	0,43115
Ir	0,04981	0,04101	0,20095	**Te**	0,04840	0,02895	0,17344
K	0,04289	-0,01360	0,02624	**Ti**	0,04941	-0,00249	0,04359
La	0,04692	0,01102	0,12832	**Tl**	0,04786	0,00508	0,04913
Li	0,04780	0,01792	0,02517	**V**	0,05023	-0,00760	0,04917
Mn	0,04925	-0,00052	0,04031	**W**	0,05041	0,10763	0,33871
Mo	0,05044	0,09583	0,32193	**Y**	0,04735	0,01432	0,15035
Na	0,04609	0,02008	0,06026	**Zn**	0,04891	0,05330	0,02449
Nb	0,04977	0,06686	0,28049	**Zr**	0,04879	0,05330	0,23779

Table 5.5 The ordering energy calculations for $Fe_{75}B_{25}X_2$

$Fe_{75}B_{23}X_2$							
X	**W_{Fe-B}**	**W_{Fe-X}**	**W_{B-X}**		**W_{Fe-B}**	**W_{Fe-X}**	**W_{B-X}**
Fe3B	0,04969	-	-	**Ni**	0,04832	0,00407	0,03071
Ag	0,04721	-0,02597	-0,00500	**Os**	0,04879	0,04110	0,20142
As	0,04830	0,01518	0,08186	**P**	0,04825	-0,02259	0,04256
Au	0,04723	-0,02693	-0,01070	**Pb**	0,04694	0,03279	0,11273
Ba	0,04280	0,18270	0,41458	**Pd**	0,04788	0,00282	0,07299
Bi	0,04674	0,09550	0,19016	**Pt**	0,04784	0,00261	0,00715
C	0,04977	0,02923	-0,00385	**Rb**	0,04024	-0,03809	-0,00454
Ca	0,04471	0,20988	0,40054	**Re**	0,04996	0,09989	0,34605
Cd	0,04711	-0,00168	0,03758	**Rh**	0,04841	0,01222	0,23458
Co	0,04872	0,00395	0,03110	**Ru**	0,04884	0,05174	0,23458
Cr	0,04862	0,00113	0,05416	**Sb**	0,04731	0,03477	0,15340
Cs	0,03834	-0,09754	-0,08468	**Sc**	0,04710	-0,00001	0,04795
Cu	0,04781	-0,00729	0,01240	**Si**	0,04807	-0,01181	0,06482
Ge	0,04778	-0,00413	0,06680	**Sn**	0,04729	0,01414	0,12034
Hf	0,04783	0,04168	0,20335	**Sr**	0,04343	0,10837	0,27684
Hg	0,04690	-0,00135	0,01089	**Ta**	0,04874	0,05882	0,26476
In	0,04700	0,00094	0,06749	**Tc**	0,05001	0,16611	0,43118
Ir	0,04878	0,04090	0,20101	**Te**	0,04732	0,02877	0,17346
K	0,04163	-0,01452	0,02379	**Ti**	0,04836	-0,00258	0,04345
La	0,04577	0,01086	0,11793	**Tl**	0,04675	0,00508	0,04886
Li	0,04667	0,01797	0,02485	**V**	0,04922	-0,00766	0,04888
Mn	0,04818	-0,00053	0,03975	**W**	0,04942	0,10766	0,33914
Mo	0,04945	0,09572	0,32238	**Y**	0,04621	0,01439	0,15043
Na	0,04491	0,01979	0,05878	**Zn**	0,04783	0,00509	0,02415
Nb	0,04874	0,06719	0,28107	**Zr**	0,04771	0,05344	0,23802

Percent change in W_{Fe-B} when there is a third element addition was also calculated for the different alloying elements. The results are shown in Fig. 5.6 and Fig. 5.7. From the results it can be seen that C, Mo, Re, Tc, V and W elements are increasing the ordering tendency between iron and boron atoms for both compositions. Apart from non-metal carbon all other elements are transition metals. The elements that increase the ordering energy are represented on the periodic table in Fig.5.8.

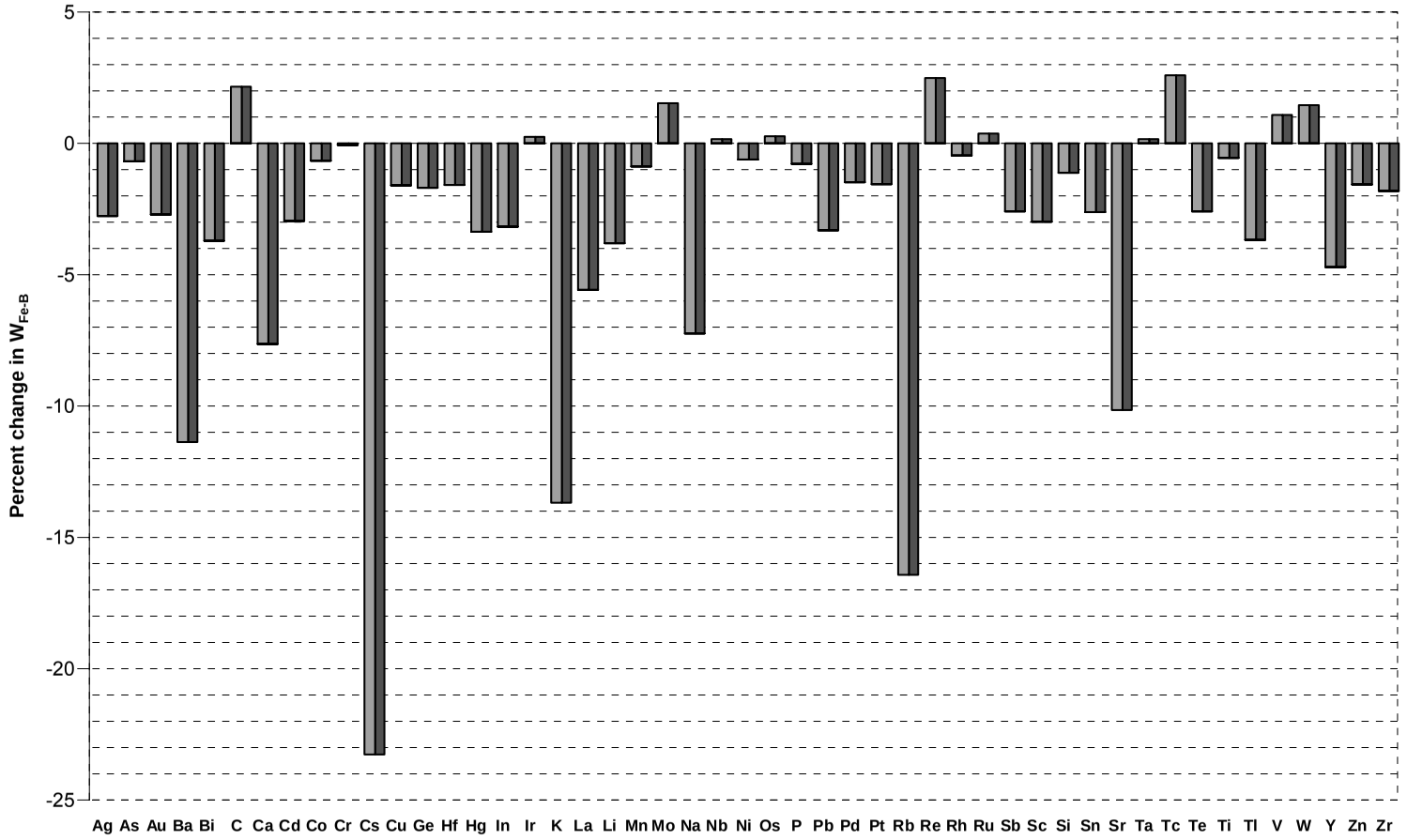

Figure 5.6 Percent change in W_{Fe-B} due to addition of 2 at. % third element in place of Fe

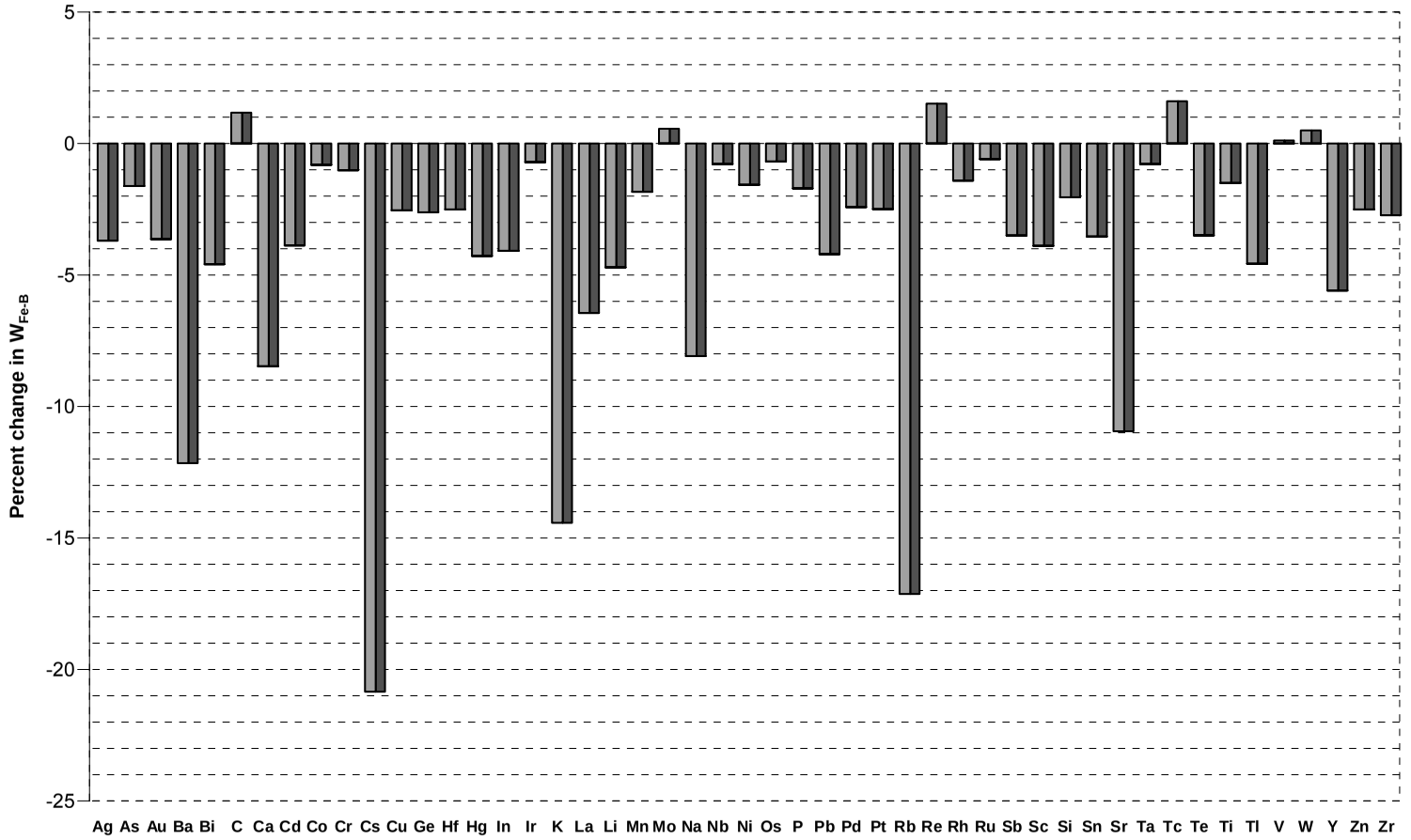

Figure 5.7 Percent change in W_{Fe-B} due to addition of 2 at. % third element in place of B

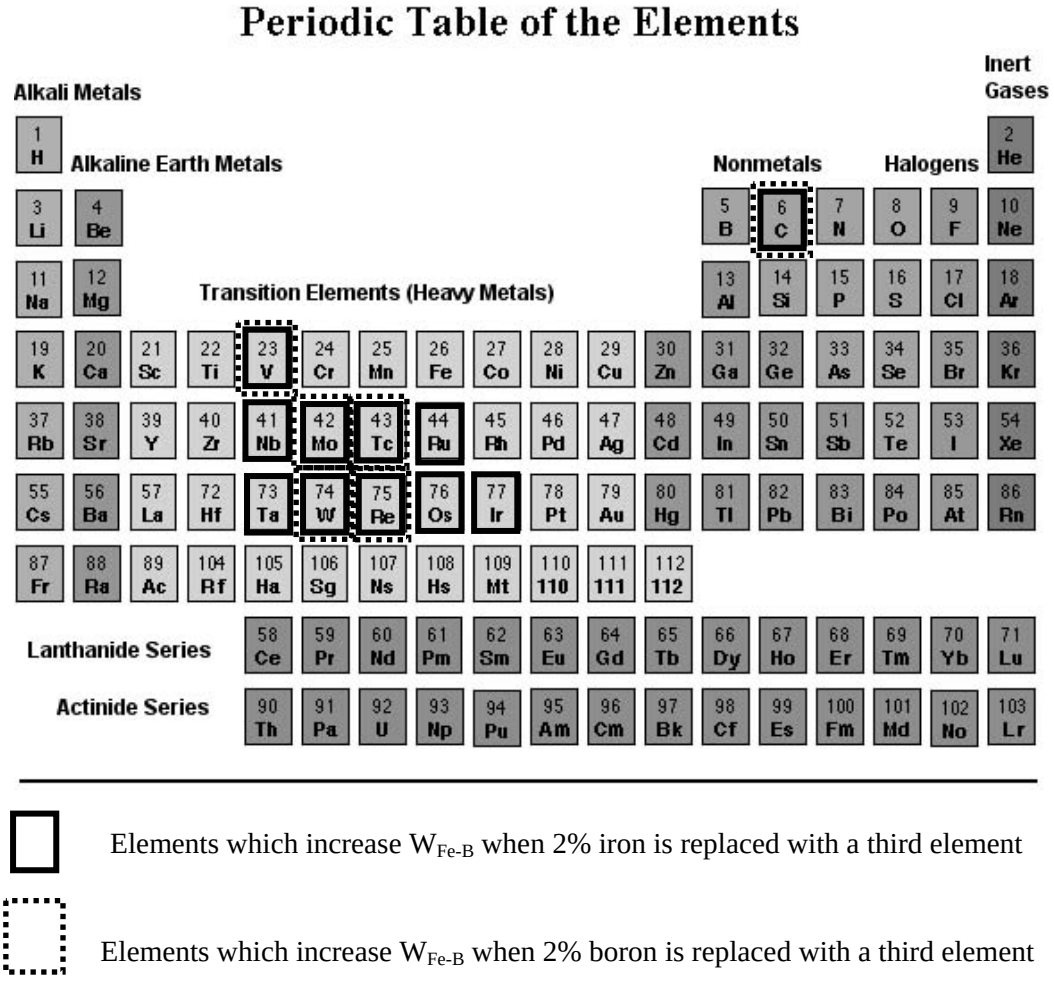

Fig. 5.8 The representation of elements which increase the W_{Fe-B} on periodic table

5.1.3 Prediction of Glass Forming Compositions

As discussed earlier, the production of bulk amorphous alloys up to date was based on trial and error methods and some semi empirical rules. Fe_3B intermetallic phase, which encounters crystal growth problems like most of the intermetallic phases, was considered to be the starting point for designing a glass forming composition. The variation of ordering energy was calculated to design

easily glass forming alloy compositions. The relationship between ordering energy and glass forming compositions should be dealt with in accordance to crystallization. Many alloy systems which are random solid solutions at elevated temperatures become partially ordered when the temperature is lowered. The amount of ordering energy between elements evaluates the degree of ordering. High ordering energy means; high tendency of unlike atoms to become nearest neighbors upon solidification because of the higher attractive potential for heterocoordination. This preferred heterocoordination necessitates an excessive amount of diffusion in the liquid phase when compared with a random solid solution because preferred atomic bonding should be accomplished in order to minimize the total energy. Therefore, elements which increase the ordering energy, especially between the binary components and other possible atomic matching combinations increase the needed undercooling for the crystal growth. This condition favors the glass forming of the melt upon rapid solidification because the suppression of the crystal growth becomes easier when the degree of needed undercooling increases.

From the results of ordering energy calculations given above, W and Mo which both increase W_{Fe-B} were chosen because of their availability. Although Tc and Re are believed to be other good candidates, they were not used due to their high cost and C was not selected as this study is centered on metallic alloying additions. Zr on the other hand, while decreasing W_{Fe-B} when used as a third element, it increases both W_{Fe-Zr} and W_{B-Zr} considerably and therefore was chosen as another alloying element during the studies.

Another parameter considered for the alloying element decision was the equilibrium solidification route dictated by the phase diagrams. The alloying elements which form complex intermetallics and undergo peritectic and eutectic reactions involving these phases were selected. Also, the compositions of

alloying elements were decided with this concern. Binary phase diagrams for the elements considered are given in Appendix B.

5.2 MD SIMULATIONS:

A molecular dynamics program, in order to heat and cool a binary or ternary system, was written in the course of this study. The code is general and can be used for any system, as long as the interatomic interaction potentials between atoms are defined. In order to test the viability of the program melting simulations were carried out, for Fe, Mg and Zn unary systems with Lennard-Jones potentials. The results for Fe will be given for the discussion.

Melting, owing to its first order transformation character, can be detected as a steep increase in the total energy of the system. The total energy vs. time step of the simulation results are given in Fig. 5.9. In Fig. 5.10 a closer look at the first 20,000 time steps of the total energy graph is presented. In Fig. 5.11 the change in the temperature of the system is given.

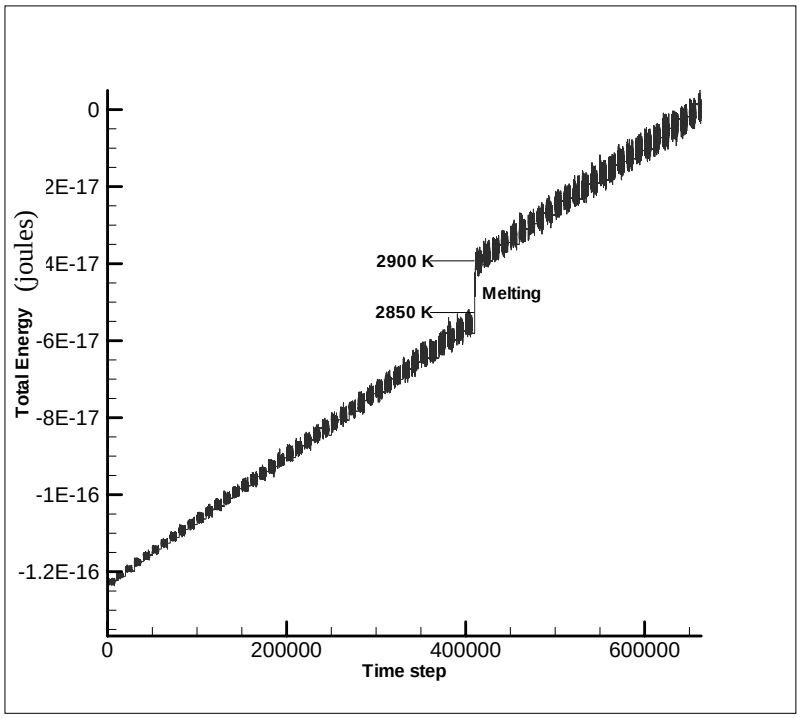

Figure 5.9 Total energy evolution of the system.

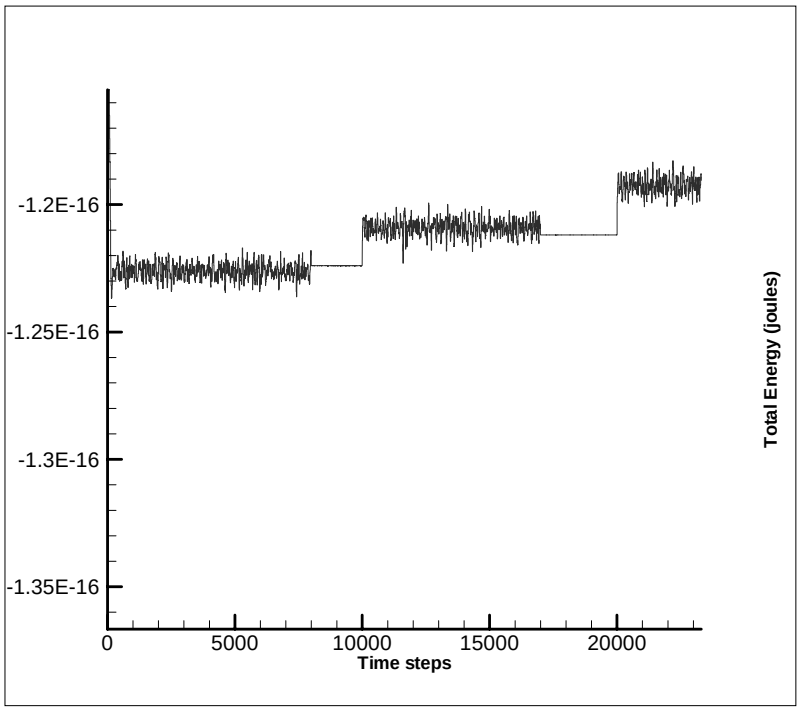

Figure 5.10 Total energy evolution of the system for first few thousand steps.

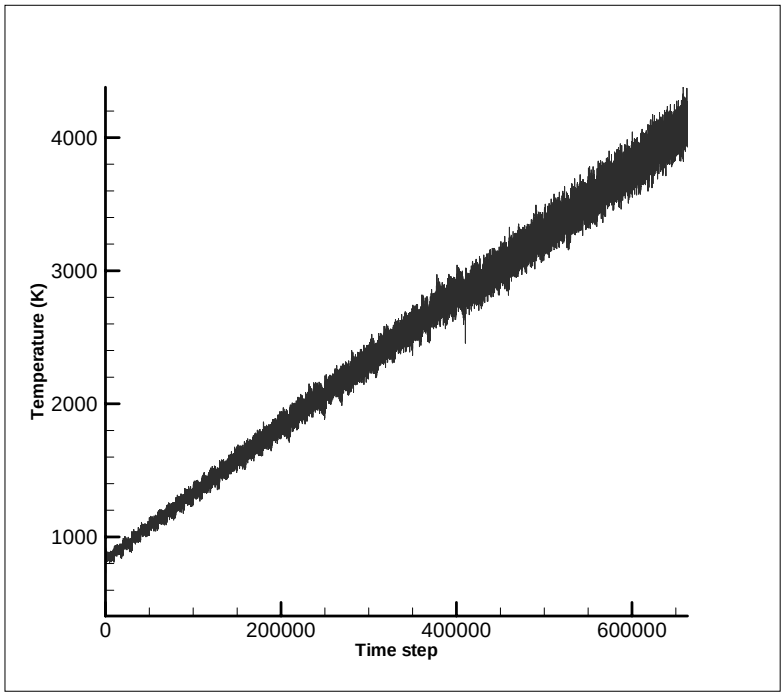

Figure 5.11 Temperature evolution of the system.

From the Fig. 5.10 it can be seen that at each isotherm for 7000 time steps, total energy fluctuates around a mean value especially at low temperatures, which is an indication of the system evolving to the equilibrium. After the 7000^{th} step of each isotherm the total energy is perfectly constant. The reason for this behavior is that after the 7000^{th} step no velocity scaling is applied, however as the temperature is monitored a small variance around the previously set temperature is seen. This means the temperature is practically constant.

The estimation of melting point is an indicator for how the interatomic potential correlates with the system. Therefore, the better the interatomic potential, smaller will be the difference between the real and simulation melting temperature. Experimentally, melting occurs at 1808 K for pure iron. However, for the MD simulation melting occurs between 2850-2900 K. The reason for the melting

temperature being higher in simulation can be explained in terms of configuration. The system under consideration in the simulation is homogeneous, without any free surface due to periodic boundary conditions employed. In addition because the initial configuration is a perfect fcc lattice, the system might not generate the equilibrium number and distribution of defects, which are usually the high energy sites available to trigger phase transformations. Although there should be some overshooting, a difference in the order of 1000 K necessitates the description of the system with Lennard-Jones potential is not the most sophisticated way.

The coordinates of the system at several different time steps are also given in Fig. 5.12. It can be observed that the temperature increases, the initial lattice starts to distort and after melting the complete long range order is lost.

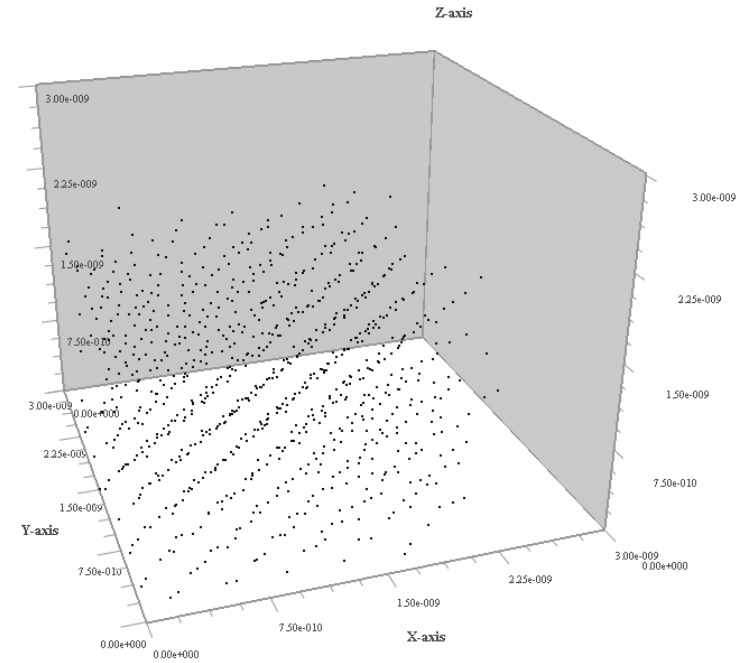

a)

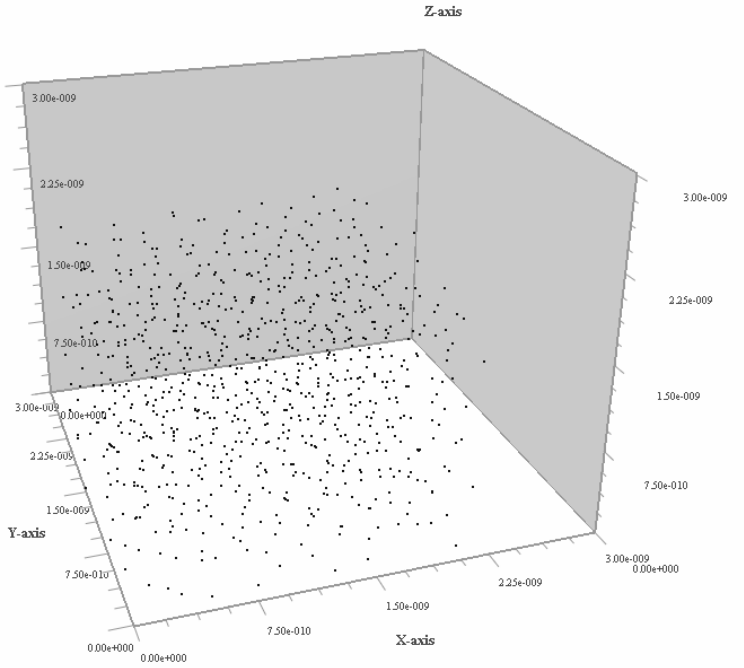

b)

Figure 5.12 The distribution of atoms in the simulation box, a) at T= 1350 K, b) at T= 2900 K.

Translational order parameter was calculated in order to check the melting temperature. For solids it is of order of unity, whereas for liquids it oscillates around zero. The change in the order parameter is given in Fig. 5.13. Translational order decreases as the system heats up where the atomic vibrations get stronger and when the solid structure is completely destroyed, at melting temperature, order steeply decreases near zero. Further heating of the system does not contribute a significant difference where oscillation of order parameter near zero is observed.

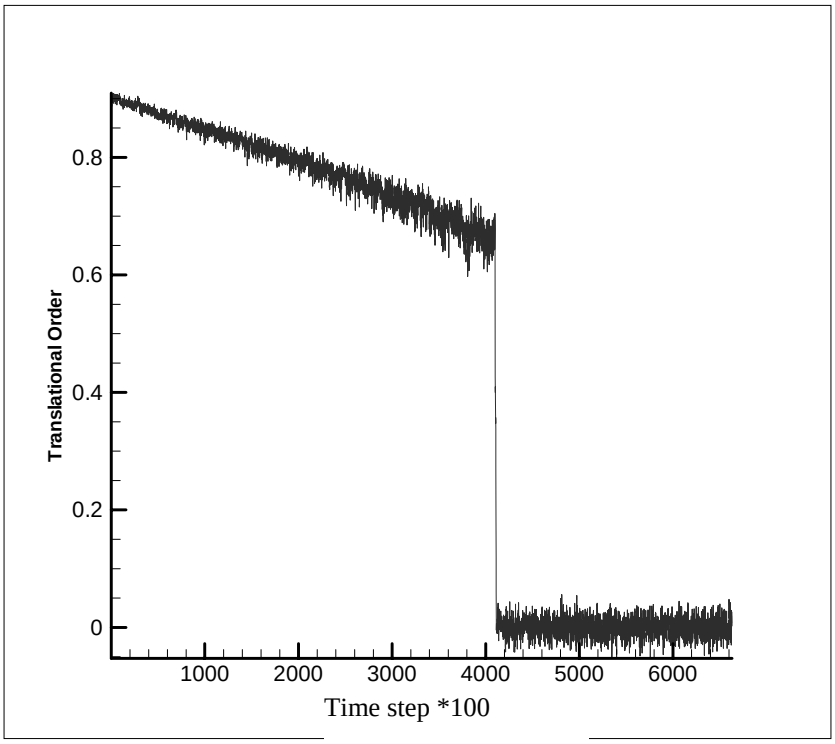

Figure 5.13 Variation of translational order parameter.

In addition to this, RDFs for two different temperatures are plot in Fig 5.14. The peaks in the RDF get broader as the temperature increases. At small separations RDF is zero, which indicates the effective width of atoms, since they cannot

overlap. A number of obvious peaks are present for the RDF at 850 K. This indicates a high degree of ordering present in crystalline state. However, for the liquid structure, peaks are broader because of the thermal motion of atoms. At very long range, RDF tends to a value of 1 because RDF describes the average density at this range.

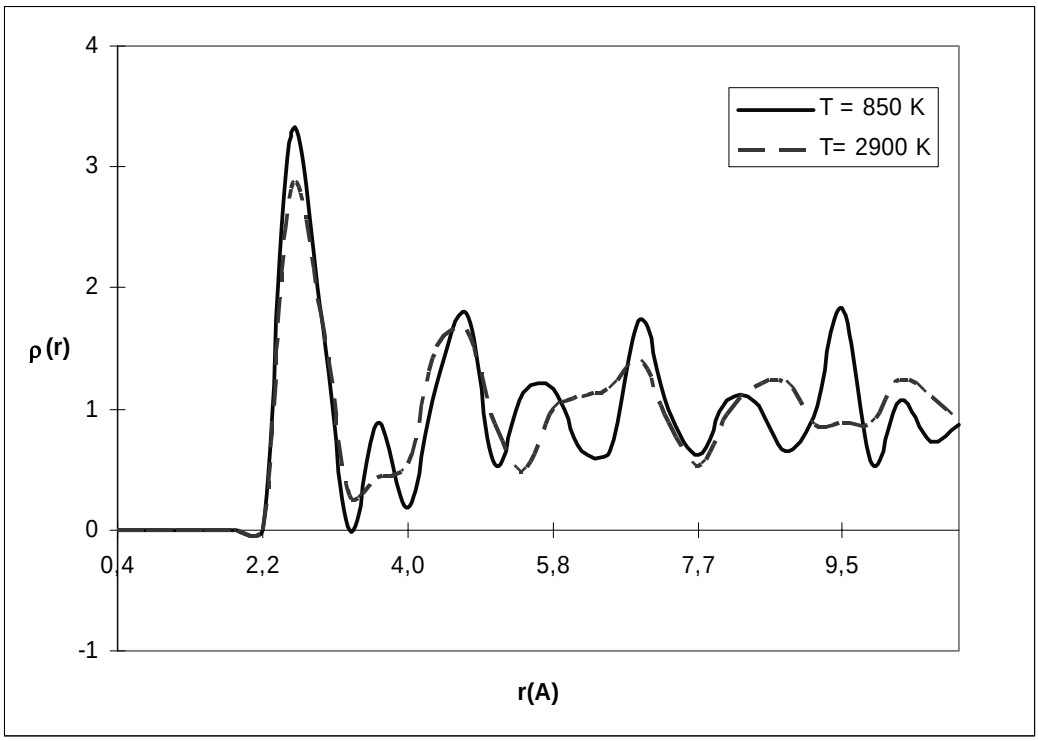

Figure 5.14 Radial distribution functions at 850 K and 2900 K.

In order to perform simulations for binary systems, the interatomic potential functions calculated, which are given in the previous section, were used to describe pair wise interactions between atoms. However, the potential energy drifts to large negative values shortly afterwards. This consequence is probably due to polynomial interpolation of the function, which is not adequate for the data at small separations. When the interpolation is carried out with exponential type

functions, the long range behavior of the data is lost and the potential energy values do not come to equilibrium. More detailed mathematical analysis should be carried out for the analytical forms of the functions.

5.3 CENTRIFUGAL CASTING EXPERIMENTS

Experimental studies were focused on forming amorphous alloys by adding alloying additions to $Fe_{75}B_{25}$ composition. This composition forms the Fe_3B intermetallic phase under non-equilibrium cooling conditions. Non-equilibrium phase diagram of the Fe-B system calculated by CALPHAD approach was taken from the literature [71] and given in Fig. 5.15. The dashed lines are the phase boundaries different from the equilibrium phase diagram. The equilibrium phase diagram of the system is also given in Fig 5.16. One major difference, between the equilibrium and non equilibrium phase diagrams, is the shift of iron rich eutectic composition to 18 at. % B from 17 at. % B and shift of the eutectic reaction temperature to 1114 ^{0}C from 1179 ^{0}C. In addition, a Fe_3B metastable phase appears on the non-equilibrium diagram instead of Fe_2B phase.

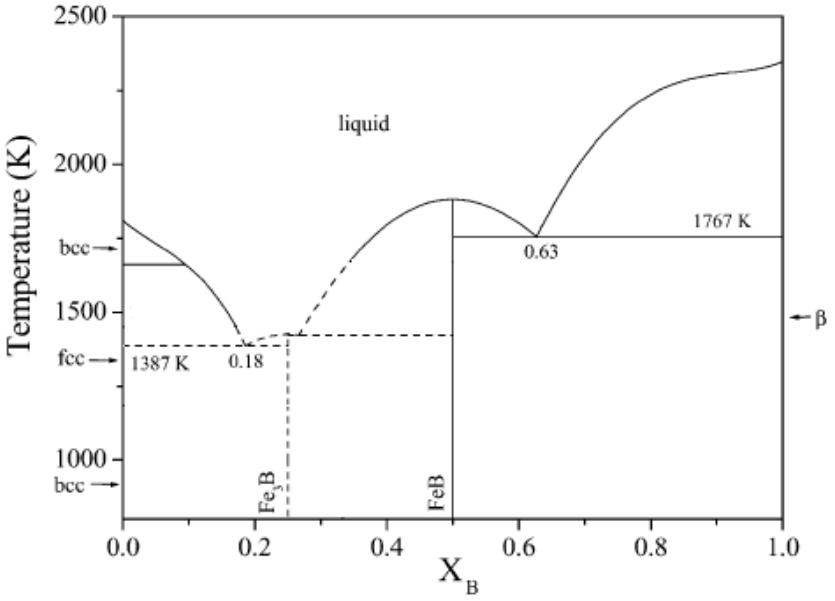

Figure 5.15 Non-equilibrium phase diagram of Fe-B system [71].

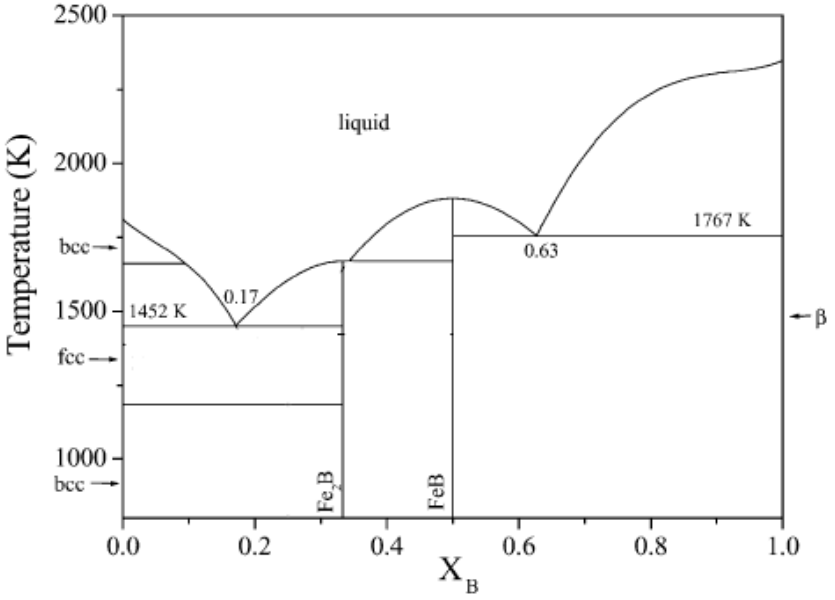

Figure 5.16 Equilibrium phase diagram of Fe-B system [71].

Fe_3B is one of the constituents of the eutectic phase mixture ($L \rightarrow \alpha + Fe_3B$). It is generally believed that eutectic compositions are suitable for alloys with high GFA due to the temperature gap being less between crystallization and glass transition. However, intermetallic compositions should also be favorable for amorphous alloy synthesis because of crystal growth problems encountered. For Zr-Ni alloys, experimental findings state that eutectic $Zr_{76}Ni_{24}$ possess a higher critical cooling rate than intermetallic $Zr_{67}Ni_{33}$ alloy [72]. Eutectics are generally believed to be good glass forming compositions, however they can have poorer GFA relative to intermetallic compositions, due to either the presence of metastable phases competing with glass formation or low melt viscosity due to lack of ordering in the melt. However, intermetallic compounds, owing to high melt viscosity and slow nucleation and growth because of their complex structure, can make them even better glass forming compositions. The crystallization problems can be explained according to the solidification interface morphology.

Two different growth morphologies are present for solid/liquid interfaces. Faceted interfaces are planar angular surfaces which are atomically flat while non-faceted interfaces are smooth and atomically rough. When the differences in structure and bonding between solid and liquid phases are high, the transition region between them becomes narrower in order to accommodate these differences. Dimensionless entropy ($\alpha=\Delta S/R$) is a good indicator for growth morphology. When α value exceeds 2, solidification proceeds with facet forming phase, like intermetallic phase growth. When α value is smaller than 2, crystallization occurs on a non-faceted interface which is the case in pure metals. An atomically flat interface will maximize the bonding between atoms in the crystals and those in the interface. This kind of interface will close up the gaps in the interface at the atomic scale and atomically flat surface will be favored. Such an interface will expose few bonds to atoms arriving via diffusion through the

liquid. Hence growth will be more difficult and requires an additional undercooling [73].

The solid intermetallic phase Fe_3B is a good example for faceted interface, due to having a complex crystal structure. In the literature, the crystallographic data for this phase is interchangeable. However, the most reliable data found by the author is given. Fe_3B has an orthorhombic structure with DO_{11} structure type. Space group of the structure is Pnma. It has the following lattice parameters, a= 4.439 Å, b= 5.5428 Å and c=6.699 Å [74]. At this point Powdercell 2.3, software for visualizing crystal structures, was used. The crystallographic data was given input and the corresponding drawing of the unit cell is given in Figure 5.17.

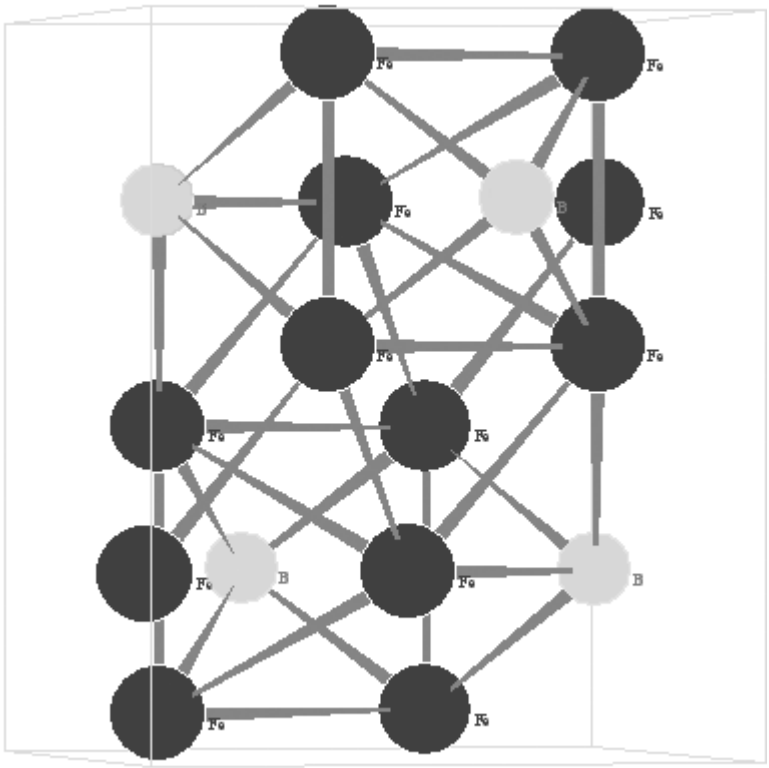

Figure 5.17 Unit cell of Fe_3B.

When the other intermetallic compound $MgZn_2$ is concerned, the same crystal complexity is observed. $MgZn_2$ has a hexagonal closed packed structure with C14 structure type. Space group of the structure is $P6_3/mmc$. It has the following lattice parameter, a= 5.17 Å and c=8.50 Å [74]. By using the Powdercell software the unit cell drawing of the $MgZn_2$ intermetallic was found and given in Fig. 5.18.

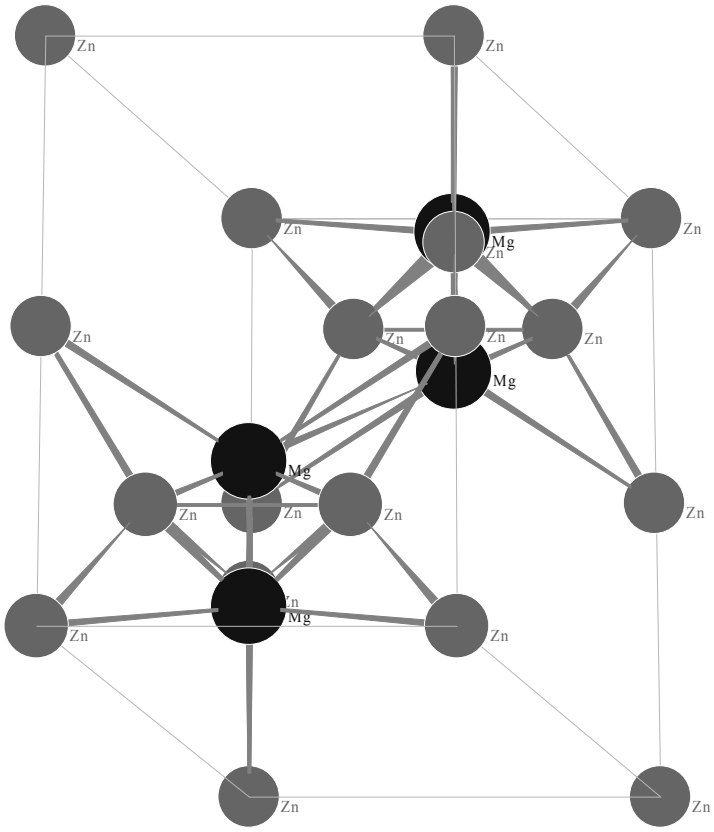

Figure 5.18 Unit cell of $MgZn_2$.

Another general remark to discuss before compiling the specific results for alloys produced is the skewed eutectic zone phenomena. Although an intermetallic binary composition was selected and modified with other alloying elements for the casting experiments, that did not prevent the microstructure forming eutectic phase mixtures in some specimens. Eutectic formation is an interacting

nucleation and cooperative growth of two solid phases. Under certain undercoolings eutectic microstructure can be found in a composition range. The coupled zone is defined as the range of alloy compositions and interface temperatures in which the eutectic morphology lead the growth front. The extent of the zone can be determined by comparing the growth velocities of eutectic and primary phases [75]. There are two types of coupled zone for eutectic systems. When the growth behaviors of two primary constituents are alike and regular eutectic formation is observed, coupled zone originates itself symmetrically around the eutectic point. On the other hand, a skewed coupled zone originates when the eutectic growth is irregular, where one of the primary phases shows a faceted solidification interface. That type of coupled zone is always skewed towards the faceted phase, owing to growth difficulties even at high undercoolings. Fe-B system having Fe_3B as one of the eutectic constituents will show this kind of coupled zone. According to Tan et al. [76] microstructural evolution of a hypereutectic alloy as a function of cooling rate in alloy system with skewed coupled zone is expected to be fully eutectic at the lowest cooling rate, eutectic plus faceted primary phase when cooling rate is increased, fully eutectic again when cooling rate is further increased, and finally eutectic plus non-faceted primary face at the highest cooling rate. However when the T_g of the alloy system is high enough, extremely high cooling rates result with fully amorphous or partially amorphous plus faceted phase microstructures. When the interface temperature of the eutectic is lower than T_g, eutectic growth will be suppressed [73].

5.3.1. C1 $Fe_{75}B_{25}$ alloy

The first binary alloy synthesized was the binary $Fe_{75}B_{25}$ alloy. Ferroboron alloy is used as the source of boron. Casting temperature of the alloy was 1200 ^{0}C. Although centrifugal casting causes rapid solidification, no amorphous phase was detected in the DSC trace, even at the thinnest section of the mold. This result

was however expected because it is known from the literature that crystallization in binary alloys is suppressed only when very high cooling rates are employed. According to previous studies in the lab, critical cooling rate for $Fe_{75}B_{25}$ alloy was calculated as 7.3337E04 ^{0}C/sec [77]. From the DCS trace, which is given in Fig. 5.19, it can be seen that the melting occurs at the onset of the endothermic peak at 1187 ^{0}C. The enthalpy of melting is found to be 89.90 joules/gram. From the phase diagram the melting temperature of metastable Fe_3B phase is 1151 ^{0}C, while the melting temperature of equilibrium Fe_2B phase is 1179 ^{0}C. Two possibilities are present for the heating curve of $Fe_{75}B_{25}$, either decomposition of the metastable Fe_3B to Fe_2B and α-ferrite occurs with an exothermic peak in the DSC signal or metastable melting of the Fe_3B was observed. According to the high temperature X-ray investigations reported in the literature, Fe_3B is stable in the temperature range 1157 ^{0}C and 1247 ^{0}C [78]. DSC traces reveal no endothermic peak for the decomposition of Fe_3B. However, to be on the safe side, the DSC measurements were repeated after slowly cooling (20 ^{0}C/sec) the sample in the DSC furnace. DSC scan of this experiment is given in Fig. 5.20. The only significant difference between these two graphs are the endothermic peak at around 953 ^{0}C that was present in the slowly cooled sample which is absent in the original DSC curve. The consequence of this behavior will be discussed following the evaluation of microstructural results.

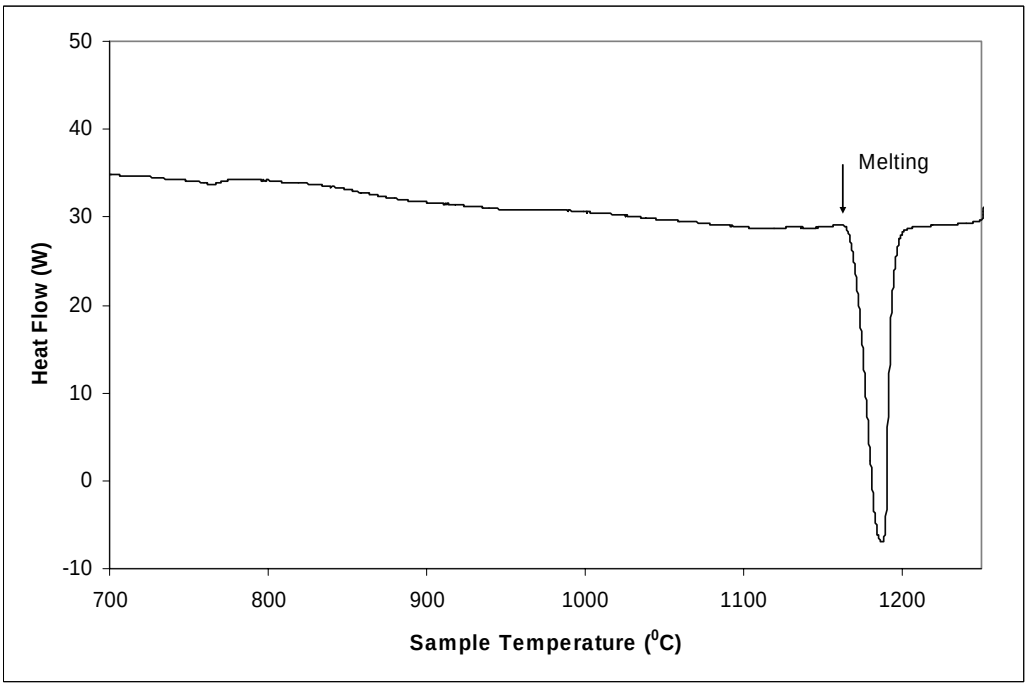

Figure 5.19 DSC trace of C1 with a scanning rate of 20 ^{0}C/sec.

Table 5.6 Thermal data about C1 alloy.

Melting Temperature	Enthalpy of Melting
1187 ^{0}C	89.90 joules/gram

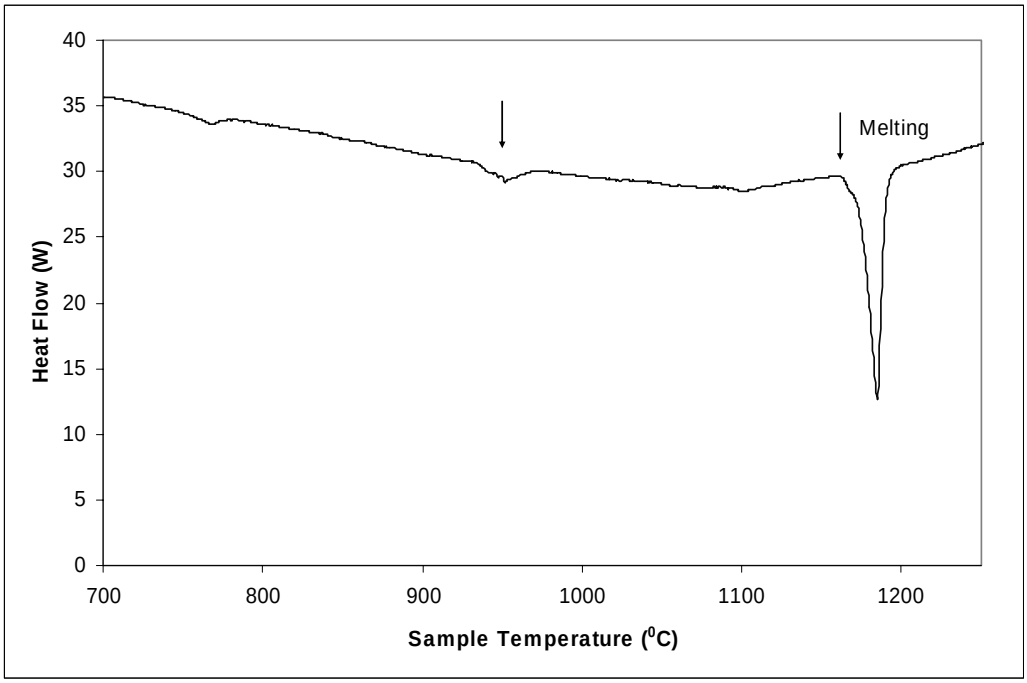

Figure 5.20 DSC trace of C1 with a scanning rate of 20 ^{0}C/sec after cooling slowly.

From the microstructural point of view the alloy was found to be composed of dendrites and eutectic phase mixture composed of Fe_3B and α-ferrite. The phases were identified according to the phase diagram, microstructure and X-ray results; detection of boron with EDS was not possible owing to boron being a light element. Also from the X-ray diffraction results it was found that some Fe_2B boron was also present in the alloy. X-ray results are given in Fig 5.21. It is believed that both intermetallic phases were formed during solidification and Fe_2B could not be visually isolated from the Fe_3B phase in the micrographs. The microstructure seen was not expected according to nominal composition under slow cooling conditions. This microstructure was formed due to skewed coupled zone phenomena. The coupled zone being skewed to the faceted intermetallic phase, revealed the microstructural findings. However, when the slowly cooled sample was heated in the DSC furnace the Fe_2B phase establishes from

decomposition of Fe_3B and metastable melting of Fe_2B was detected. Also, the endothermic signal in the DSC trace can be explained by this phase transformation.

The microstructure of the sample was analyzed through the wedge dimension in order to observe the alterations due to different cooling rates. From the micrographs it is seen that as the cooling rate increased eutectic phase separation distance and the percentage of primary α-Fe phase were decreased. This refinement arose due to decrease in time for the liquid phase to perform composition partitioning on the eutectic reaction front when cooling rate was increased. The secondary electron images of the alloy are given in Fig 5.22. From the EDS analysis no elements other than Fe were detected. Although the ferroboron alloy contains minute amounts of impurities, probably the alloy was compositionally refined due to slag formation during casting and/or the amount of impurities inside the alloy was insufficient for detection.

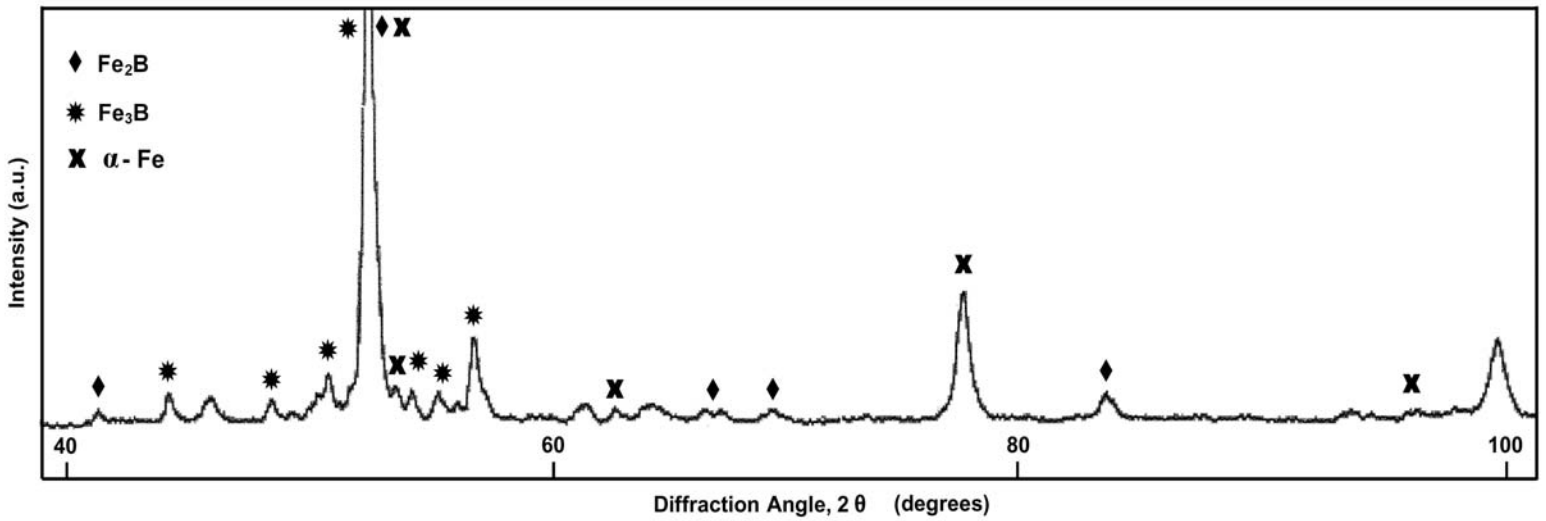

Figure 5.21 X-ray diffraction pattern of C1 alloy.

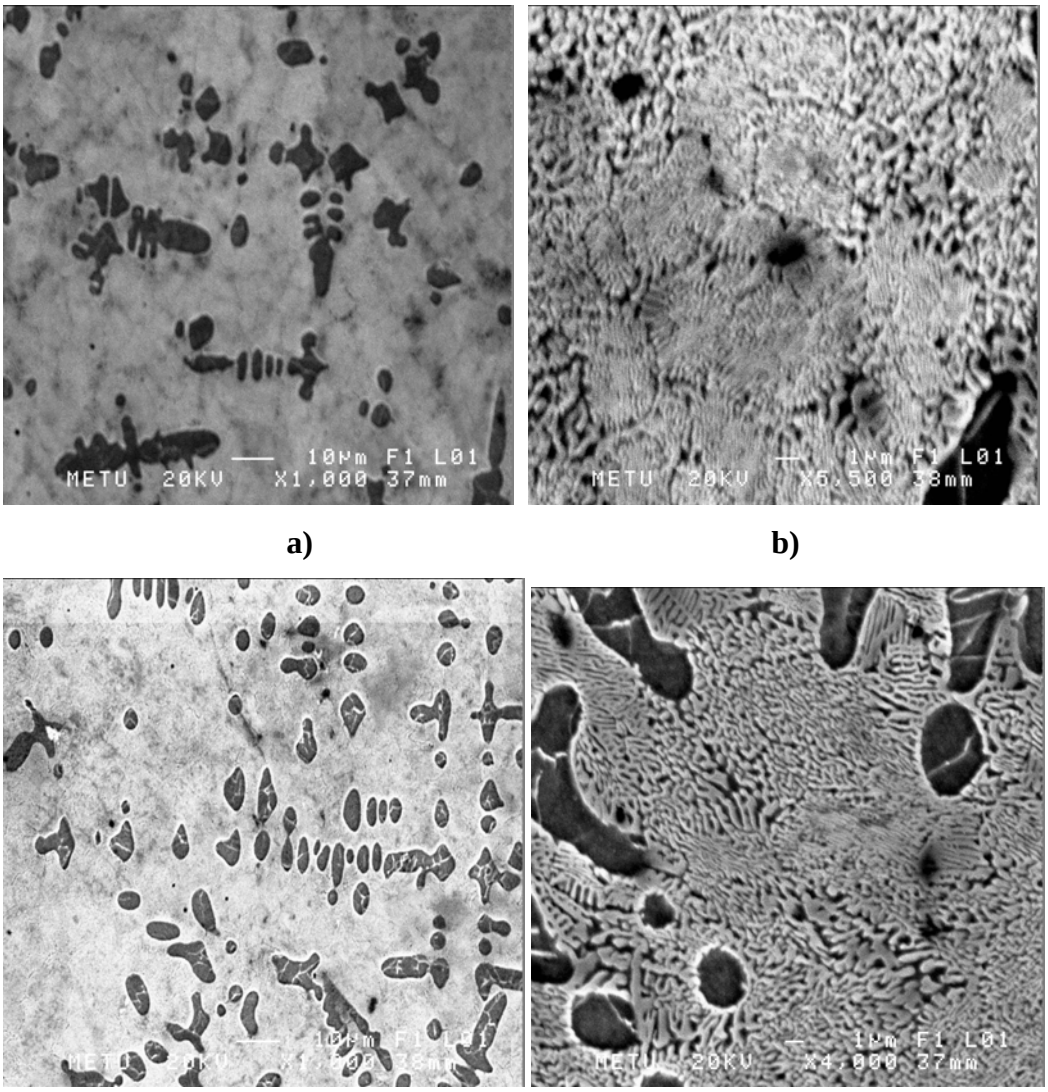

Figure 5.22. Secondary electron images of C1 alloy. a) and b) are the photographs taken from the thinnest section while c) and d) are taken from the thickest section of the casting.

In order to see mechanical consequences of the microstructural refinement, results of hardness measurements are given for this alloy in Fig.5.23. It is seen that hardness increases through the wedge direction when the cooling rate increases. Also, it is seen that hardness and therefore strength of the specimen is

higher in the transversal axis in the thinner sections. This probably arises due to solidification rate being higher in this direction. Hardness values around 700 HV can be achieved at the thin sections, which means this material can find usage areas such as cutting tool applications.

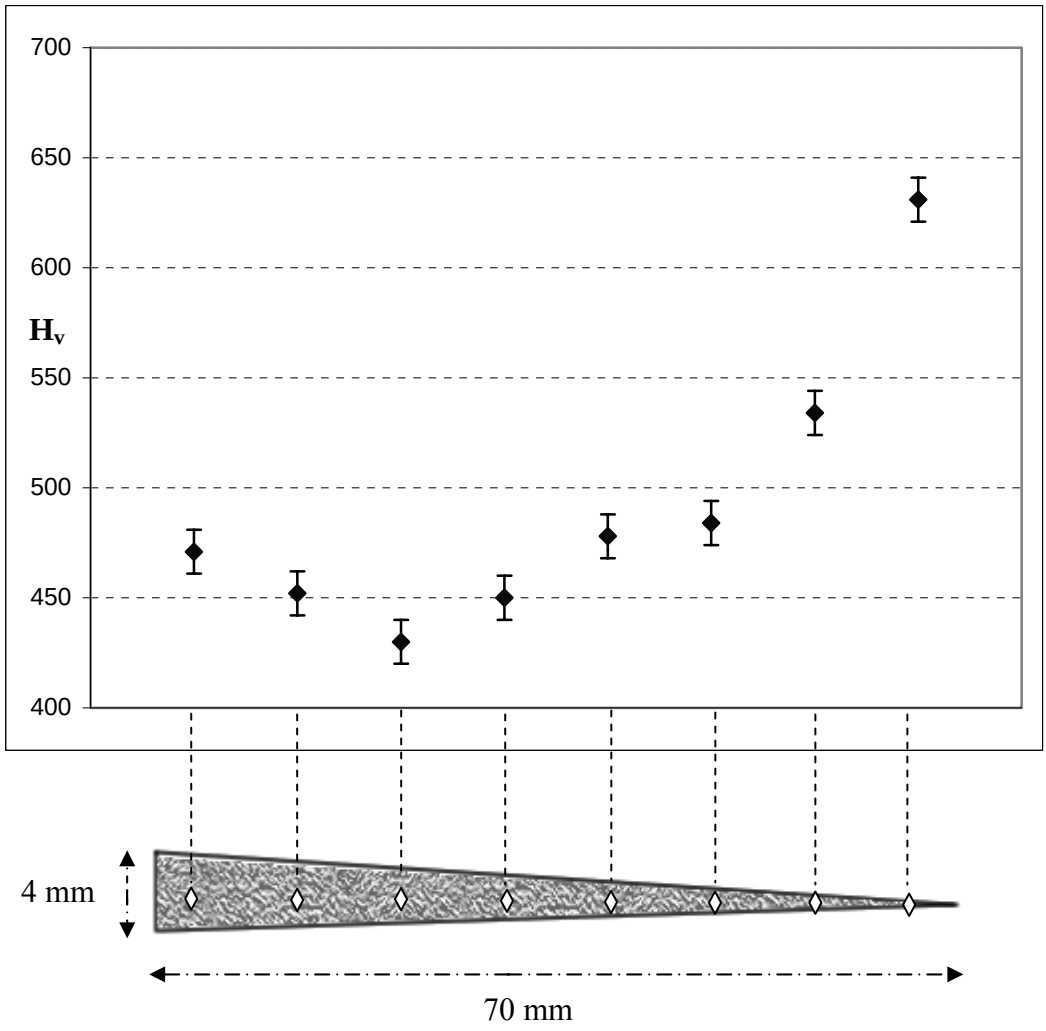

Fig 5.23 Hardness profile of $Fe_{75}B_{25}$ alloy hardness measurements are taken from the corresponding positions on the wedge given in the figure.

5.3.2 C2 $Fe_{75}B_{25}$ alloy

In order to see the differences between binary alloys synthesized using pure elements and ferroboron alloy, C2 alloy was produced with the same composition $Fe_{75}B_{25}$ from pure elements. Firstly, the DSC trace of the alloy is given in Fig. 5.24. The melting temperature of the alloy was found to be 1160 ^{0}C. Again no amorphous structure can be seen. No trace for decomposition of Fe_3B is seen.

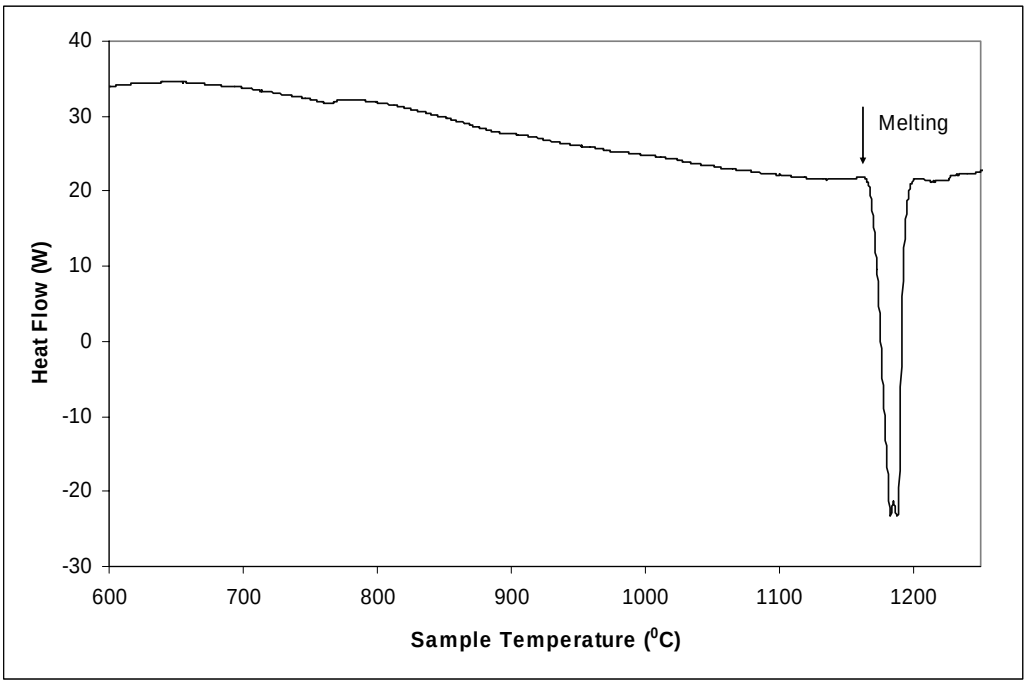

Figure 5.24 DSC curve of C2 alloy with a scanning rate 20 ^{0}C/min.

Table 5.7 Thermal data about C2 alloy.

Melting Temperature	Enthalpy of Melting
1160 ^{0}C	96.86 joules/gram

When microstructural examinations were carried out for the C2 alloy, an interesting phase selection occurred according to the cooling rate of the examinations taken. At the thickest section of wedge, faceted primary Fe_3B and eutectic phase mixture consisting of Fe_3B and α-Fe exist. When the examinations were done on the mold wall, α-Fe dendrites become the primary phase together with an irregular eutectic mixture. Also in some middle regions completely eutectic microstructure can be seen. The SEM images of the alloy are given in Fig. 5.25. In these images transition from 100% eutectic to primary α-Fe plus eutectic can be seen, the upper right part of the picture c) is nearer to the mold wall therefore cools more rapidly. X-ray results given in Fig. 5.26 show Fe_2B, Fe_3B and α-Fe phases can be identified from the diffraction peaks.

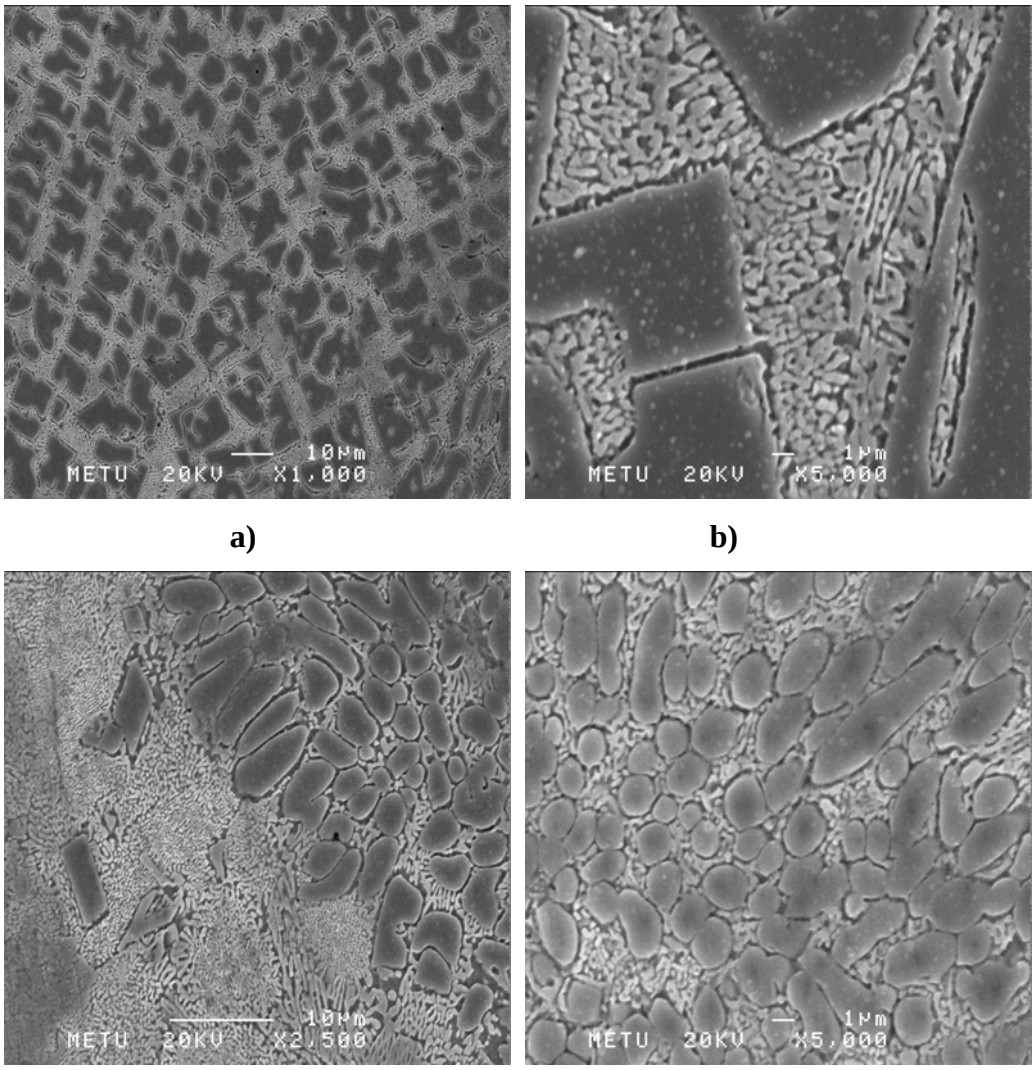

a) **b)**

c) **d)**

Figure 5.25 Secondary electron images of C2 alloy a) and b) are taken from the thickest section, c) taken from the outer part middle sections, d) taken from the thinnest section.

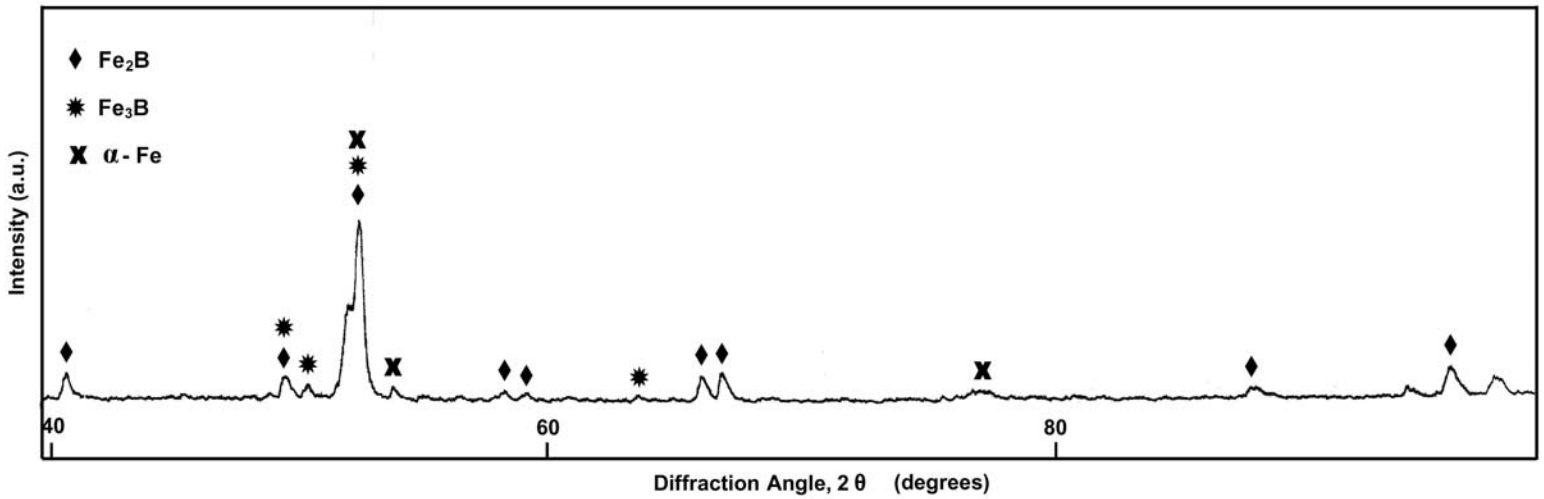

Figure 5.26 X-ray Diffraction pattern for C2 alloy.

The phase selection process occurred in alloy C2, while alloy C1 synthesized from ferroboron, just showed a refinement upon different cooling conditions, this should be explained. Although there can be slight composition inhomogenities for the ferroboron, probably the other impurities present altered the geometry of the coupled zone or may have inhibited the nucleation of α-Fe dendrites. However, this is no more than a speculation and in order to investigate this phenomenon exact spectrometric analysis, which can detect boron, should be done to compare the compositions of each alloy.

The hardness profile given in Fig. 5.27 shows an increasing trend similar to C1 alloy. However, higher values were attained. This is due to primary phase being the Fe_3B in the thick regions. Also, the amount of change in the hardness values from the thick sections to thin sections was less. This probably occured due to coarse microstructure at thickest sections contains hard Fe_3B phase but as the cooling rate increases the primary phase changes to fine softer α-Fe.

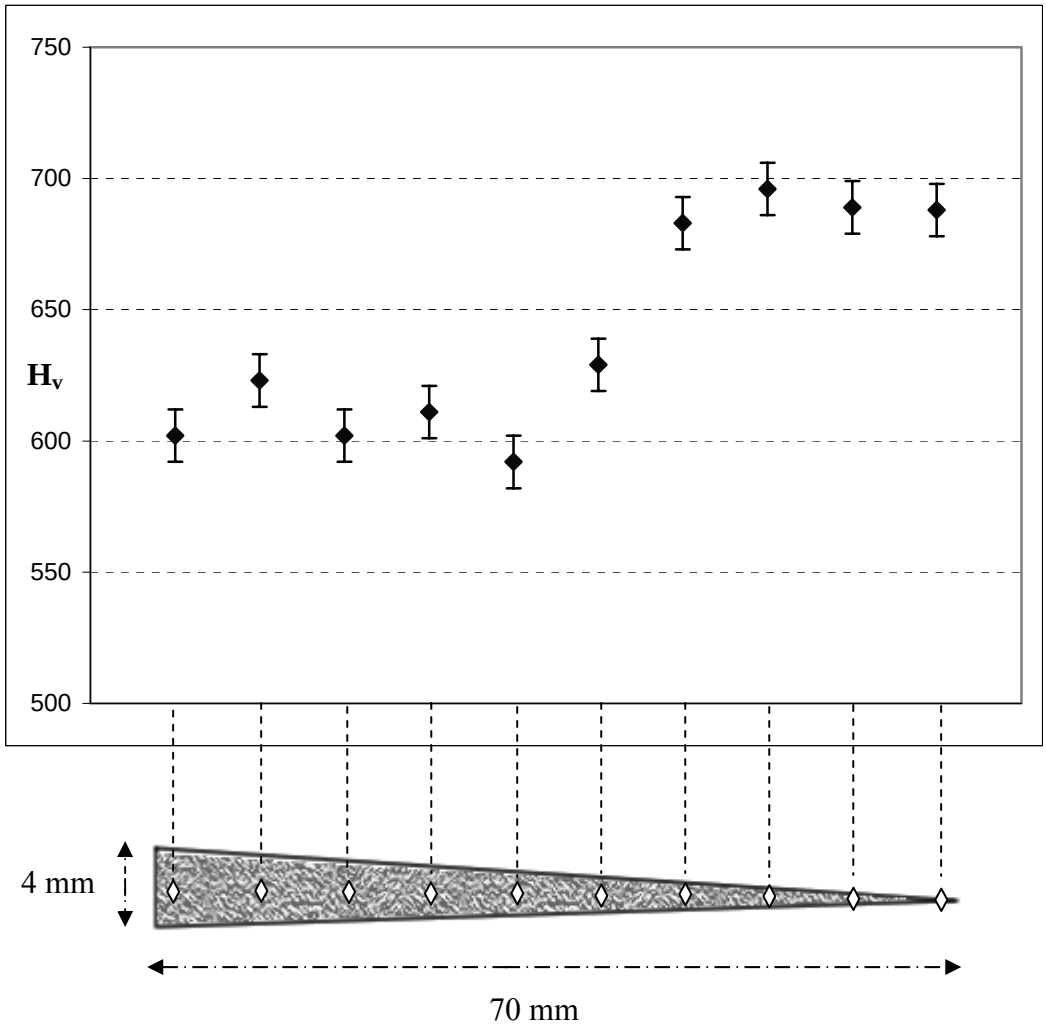

Figure 5.27 Hardness profile of C2 alloy. Hardness measurements are taken according to the wedge given in the figure.

5.3.3 C4 $Fe_{63}B_{21}Mo_{16}$ alloy

The first ternary alloy to be discussed will be C4. Mo was added to the binary composition, while the stoichiometry between iron and boron was not altered. When deciding on the amount of Mo to be added, phase diagrams between Mo-Fe and Mo-B were considered. For both systems, compositions near invariant reactions where complex eutectics are formed were chosen.

The casting temperature of the alloy was 1250 ^{0}C. The DSC trace taken for the alloy is given in Fig. 5.28. From the DSC curve no glass transition and crystallization behavior was observed. In other words, a fully crystalline alloy was synthesized although it was rapidly cooled. The melting temperature, which is the onset point of exothermic peak was found to be 1210 ^{0}C. The alloy formed was very brittle and it was even hard to handle without fracture.

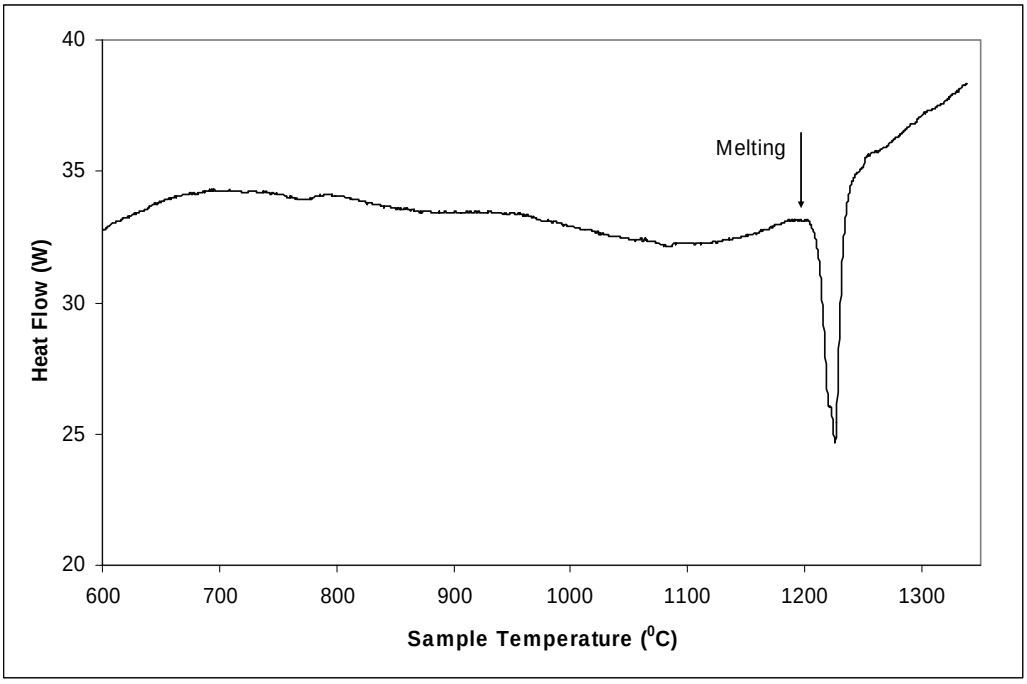

Figure 5.28 DSC curve of C4 alloy with a scanning rate 20 ^{0}C/min.

Table 5.8. Thermal data about C4 alloy.

Melting Temperature	Enthalpy of Melting
1210 ^{0}C	13.76 joules/gram

In order to examine the microstructural evolution of the alloy, secondary electron and back scatter images were taken. The SEM images of the alloy are given in Fig. 5.29. EDS analyses of the phases are given in Table 5.9 for the phases present. The phases on the micrograph are named as the X phase with the lightest contrast, Y phase with the medium contrast and Z phase with the darkest contrast.

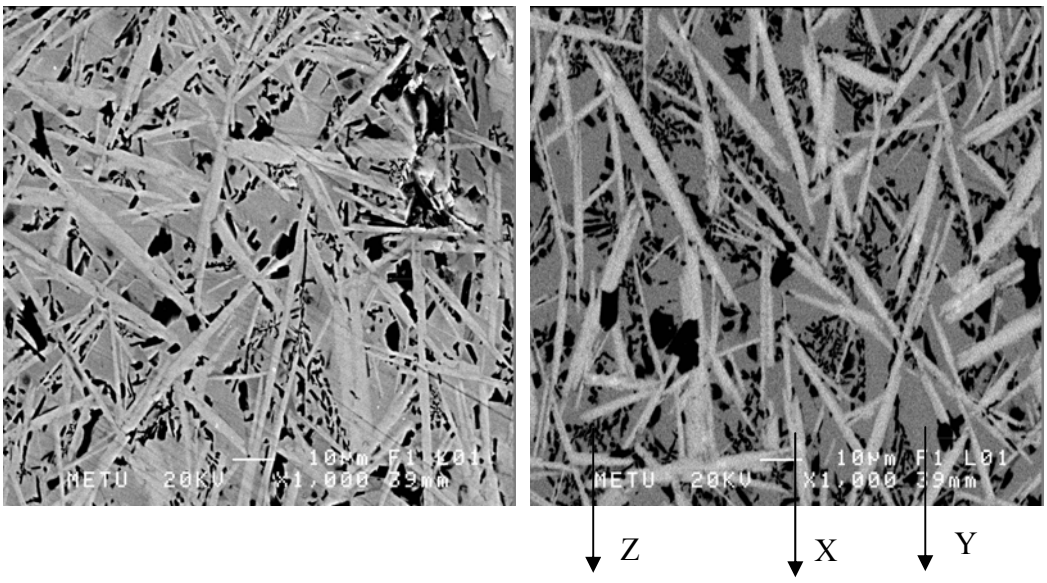

a) **b)**

Figure 5.29 SEM views of C4 alloy, a) secondary electron image, and b) back scatter image

Table 5.9 EDS analysis results for the phases present in C4 alloy

	X		Y		Z	
	weight percent	atomic percent	weight percent	atomic percent	weight percent	atomic percent
Fe	47,84	61,2	99,53	99,18	82,23	73,55
Mo	52,17	38,8	0	0,00	4,85	2,52
Al	0	0	0	0	12,93	23,93
S	0	0	0,47	0,82	0	0

When the X-ray results were examined, the phases that exist in the microstructure were found to be Fe_2B, Fe_3B, FeB, Fe_2Mo, Fe_2MoB_4 and Fe_3Al. X-ray diffractogramme of the alloy is given in Fig. 5.30. When this data was combined with the EDS results, the Z phase was found to be Fe_3Al phase. Aluminum should have been reduced from the Al_2O_3 bearing crucible and altered the composition of the alloy. Y phase is believed to be Fe_2B and/or Fe_3B and X phase is Fe_2MoB_4 and $FeMo_2$

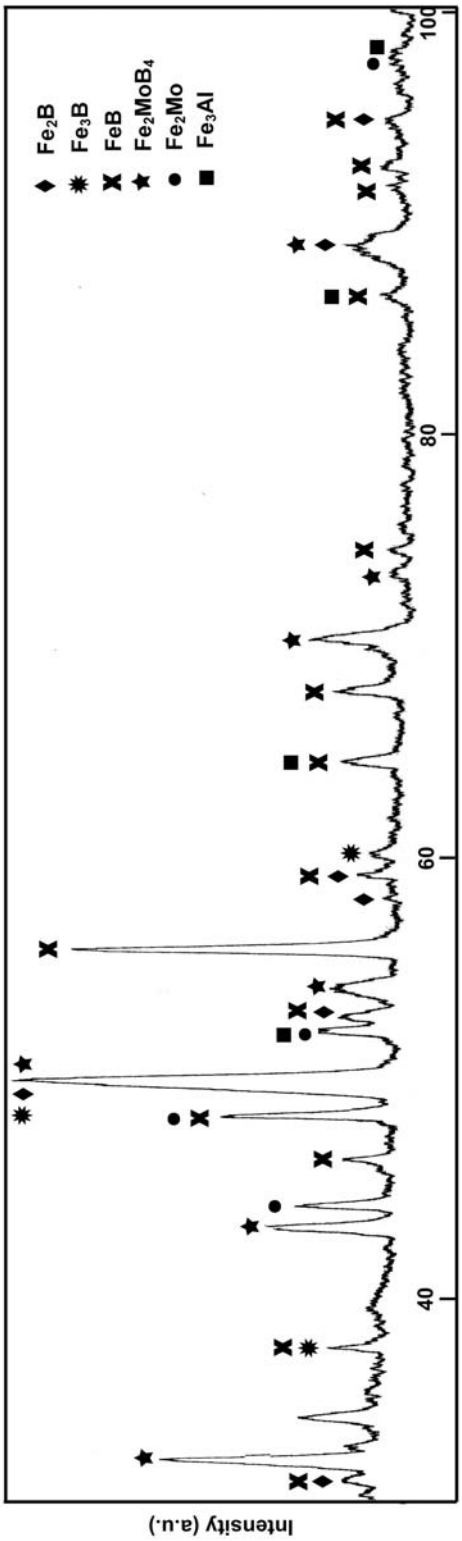

Figure 5.30 X-ray Diffraction pattern for C4 alloy.

5.3.4 C6 $Fe_{63}B_{16}Mo_{14}W_7$ alloy

From the previous results, it is deduced that Mo addition didn't increase the GFA considerably. In order to increase GFA further, another alloying element W was added to alloy according to the predictions based on ordering energy calculations. The stoichiometry between the iron and boron was conserved to $Fe_{75}B_{25}$.

The casting temperature of this alloy was 1300 ^{0}C. However, DSC trace of this alloy also ceases to show an amorphous phase. DCS curve of the alloy is given in Fig. 5.31. In the DSC trace, around 880 ^{0}C, a Tg like Cp variation can be seen. However, from the SEM observations no amorphous phase was detected for this alloy. This behavior probably arises from some structural relaxation of rapidly cooled phases. The melting temperature of the alloy was found to be 1280 ^{0}C. Although the melting temperature of the alloy C6 is same as the C4 alloy, the casting temperature has to be higher in our system due to the increased amount of high melting point elements such as Mo and W. Melting temperature of Mo is 2620 ^{0}C, while the melting temperature of the W is 3400 ^{0}C. The increase in the casting temperature is believed to be detrimental to glass forming of the alloy. When the casting was carried out well above the melting temperature, cooling rate decreases.

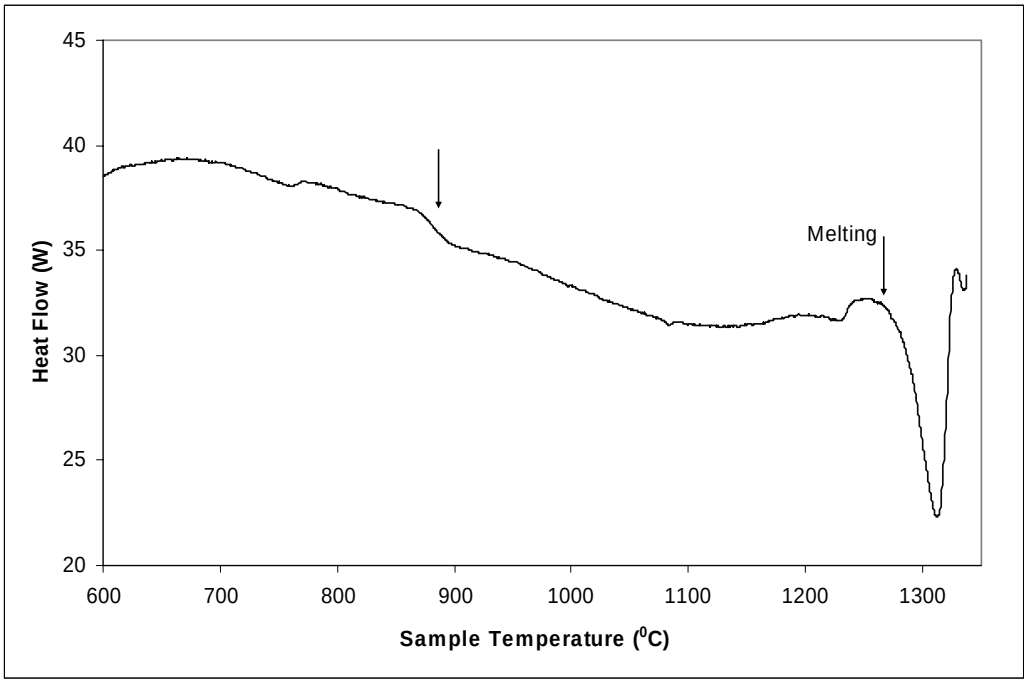

Figure 5.31 DSC curve of C6 alloy with a scanning rate 20 ^{0}C/min.

Table 5.10 Thermal data about C6 alloy.

Melting Temperature	Enthalpy of Melting
1280 ^{0}C	29.60 joules/gram

From a microstructural point of view, the alloy consists of a faceted intermetallic primary phase and an irregular eutectic phase mixture. SEM images of the alloy are given in Fig. 5.32. It was also observed that the primary phase morphology becomes more irregular when the cooling rate increases. This is due to one of the eutectic phases encountering growth problems. Also, the eutectic phase separation distance decreases when the cooling rate increases. When the EDS analyses were carried out the compositions of the microconsituents were found and tabulated in Table 5.11. The eutectic phases could not be analyzed because they are being too small. In the secondary electron images of the alloy taken

from the thinnest region, even at 4000x magnification, the eutectic phase was not resolved properly, however from element analyses it was confirmed that it has the same composition with the eutectic in the thick regions of the sample. According to this, it was comprehended that the eutectic morphology is distorted due to high cooling rates.

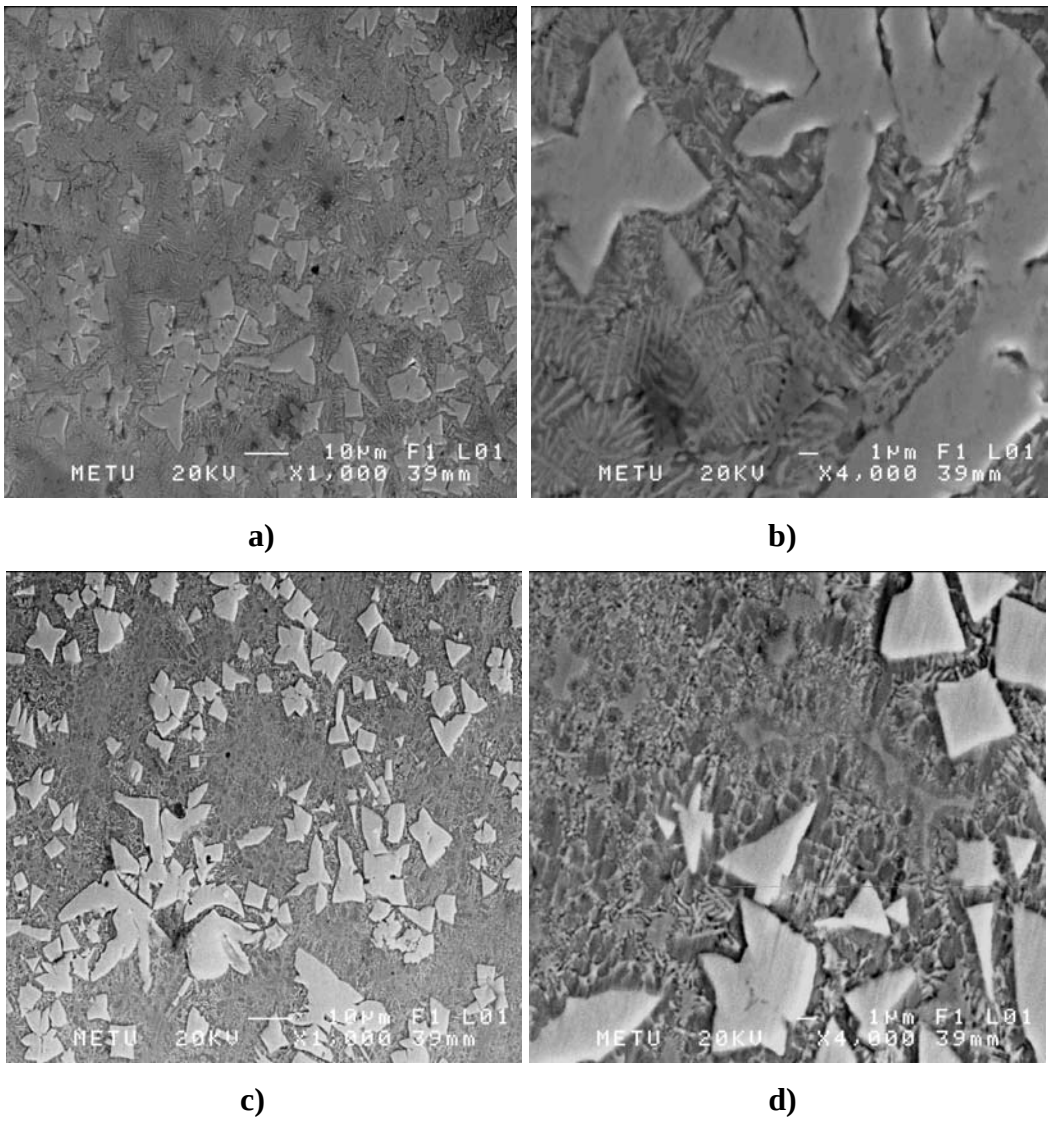

Figure 5.32 Secondary electron images of C6 alloy a) and b) are taken from the thickest region of the casting while c) and d) are taken from the thinnest region.

Table 5.11 EDS analysis results of C6 alloy.

	Faceted phase		Eutectic phase mixture	
	weight percent	**atomic percent**	**weight percent**	**atomic percent**
Fe	19,31	33,19	70,83	83,47
Mo	51,60	51,63	18,57	12,74
W	29,09	15,19	10,59	3,79

From the X-ray results, detected phases were identified as $Fe_{1.25}W_{1.75}B_2$, $FeMo_2B_2$ and Fe_2MoB_4. X-ray diffraction pattern of the alloy is given in Fig. 5.33.

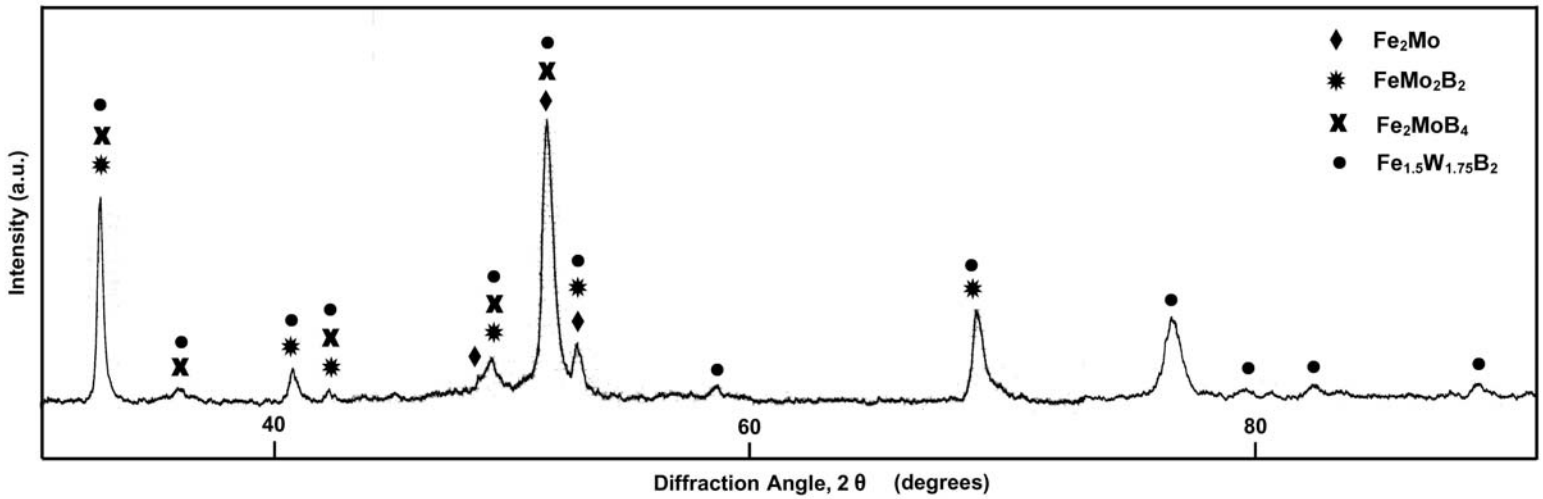

Figure 5.33 X-ray Diffraction pattern for C6 alloy.

5.3.5 C9 $Fe_{62}B_{21}Mo_5W_2Zr_6$ alloy

It was recognized from the previous casting experiments that when high melting point alloying additives like Mo and W are added to the system, the melting temperature increases. This complicates both the casting process and negatively affects the glass forming ability. Zr on the other hand, forming ternary eutectic with Fe and boron at Zr rich side, may decrease the melting temperature of the alloy. However, another complication arises due to Zr being very reactive. Alumina from the crucible material can also be reduced when the temperatures are high. For Fe-B-Zr system it was reported in the literature that the Mo and W is effective in increasing the GFA and when these elements were used in the combination of Mo5W2 it is seen that T_{rg} about 0.60 can be obtained [79].

Casting temperature of the alloy was 1350 ^{0}C. However, an excessive amount of slag formation was detected during the heating of alloy constituents. The temperature measurements were done by the pyrometer and it is probable that the temperature below the slag layer was well above the casting temperature reported. From the DSC curve there was no distinct sign of crystallization, however there were some C_p variations quite unexpected for a crystalline alloy. In order to reveal this behavior, the melted alloy was slowly cooled in the DSC furnace to room temperature and heated again in the DSC furnace. Two curves are given in Fig. 5.34. The variations around 800 ^{0}C are more evident when compared with the DSC trace of slowly cooled alloy. Also, the melting enthalpy for the rapidly cooled specimen was significantly higher than the slowly cooled sample. For some non-bulk forming metallic glasses such behavior can be observed. Instead of forming distinct crystallization, structural relaxation can occur. In that case an exothermic peak may be absent. According to this justification at the thinnest section of the casting some amorphous phase can be found where the cooling rate is high, however when thickness increases slightly crystalline phases should be present.

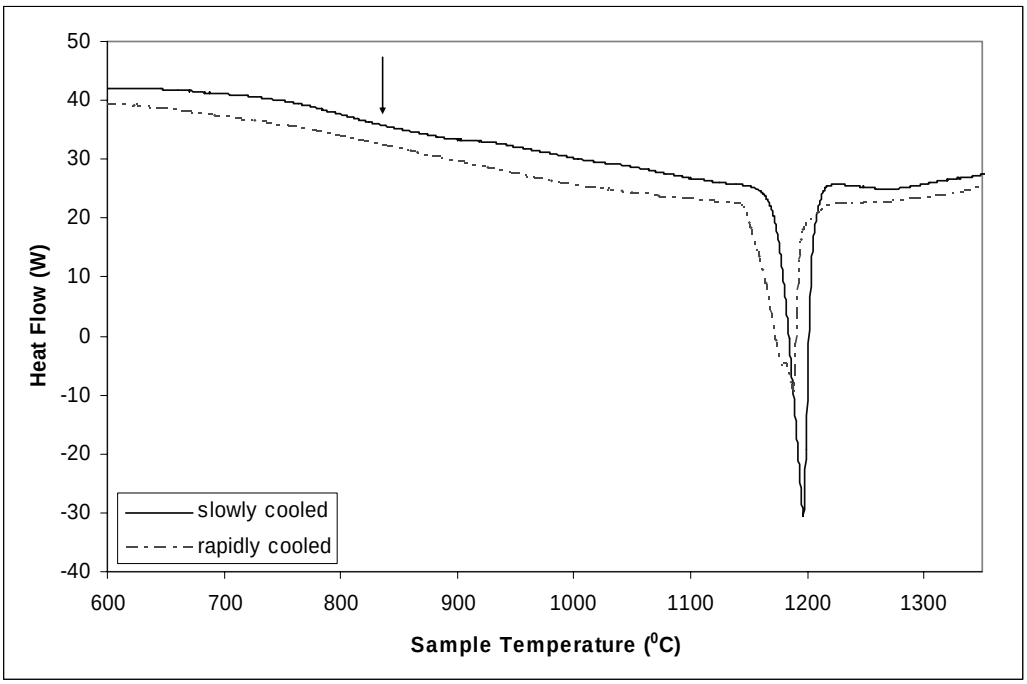

Figure 5.34 DSC curve of C9 alloy with a scanning rate 20 ^{0}C/min.

Table 5.12 Thermal data about C9 alloy.

Melting Temperature	Enthalpy of Melting
1196 ^{0}C	134.35 joules/gram

When microstructural investigations were carried out, at the thinnest section amorphous matrix was observed with crystalline phases embedded into it. However, when the examinations were done for thicker sections no amorphous matrix appears. When the alloy was examined from the thickest region, a faceted primary phase and an irregular eutectic formation was observed. The faceted phase is bearing Fe, Mo, and W, while eutectic phase mixture contains Fe, Al and probably B. SEM images of the alloy are given in Fig.5.35. The general

composition of the alloy according to EDS analysis was 11.41 % Al, 76.81 % Fe, 8.19% Mo and 3.59% W in atomic percents when boron is excluded.

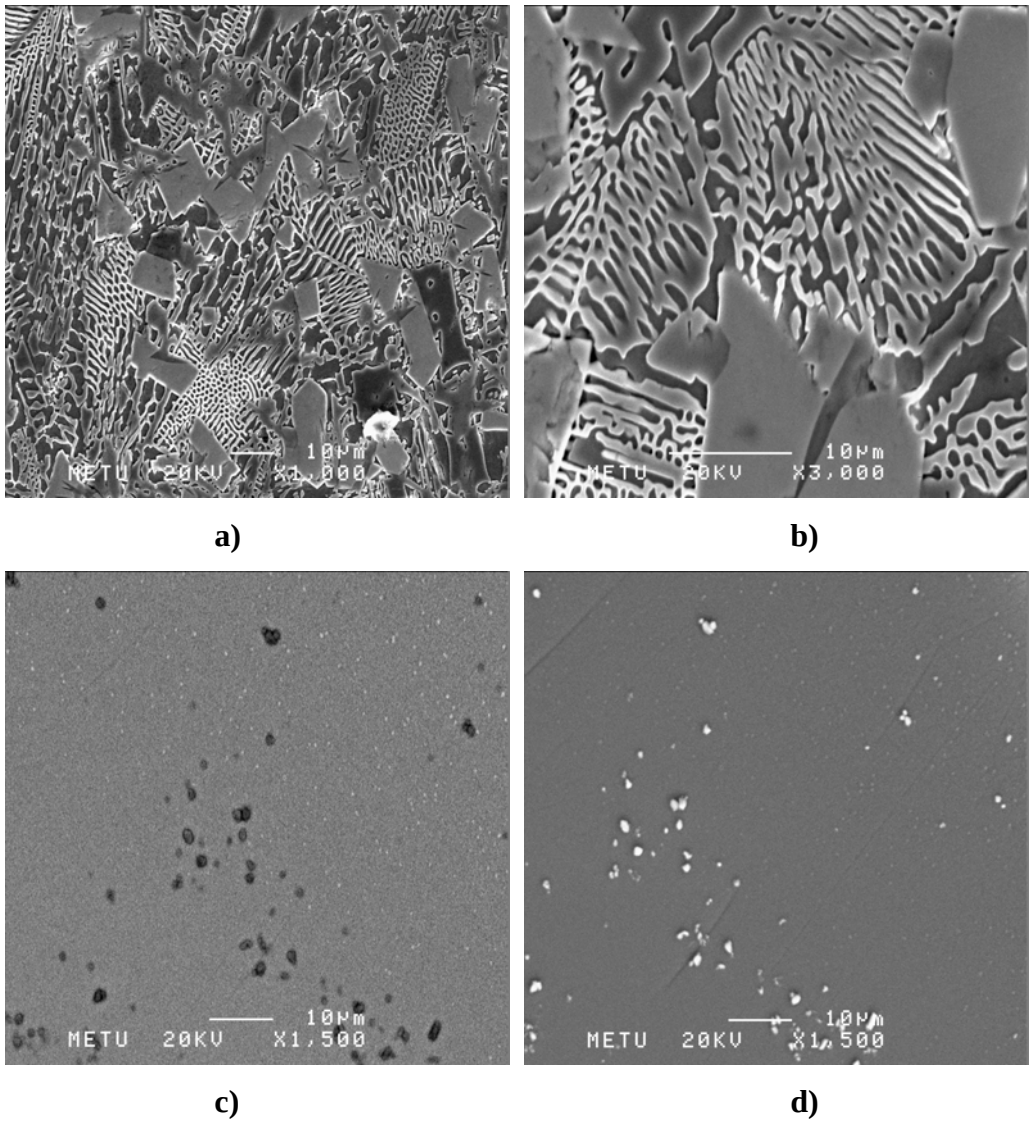

Figure 5.35 SEM images of C9 alloy a) and b) are taken from thick section while c) is back scattered image of the thinnest section d) is the secondary electron image of the thinnest section.

Table 5.13 EDS analysis results of C9 alloy.

	Faceted		Eutectic phase mixture	
	weight percent	**atomic percent**	**weight percent**	**atomic percent**
Fe	20,70	36,50	93,29	87,52
Mo	42,83	43,96	0	0
W	36,47	19,54	0,33	0,09
Al	0	0	6,38	12,38

When the X-ray data related with this alloy was examined, the α-Fe, ZrB and ZrB_2 phases were identified in the thinnest section of the alloy. Although in x-ray results the crystalline peaks were present there was also a broad peak centered near $2\theta=50^0$ which indicates some amorphous phase is also present. X-ray diffraction pattern of the alloy is given in Fig. 5.36.

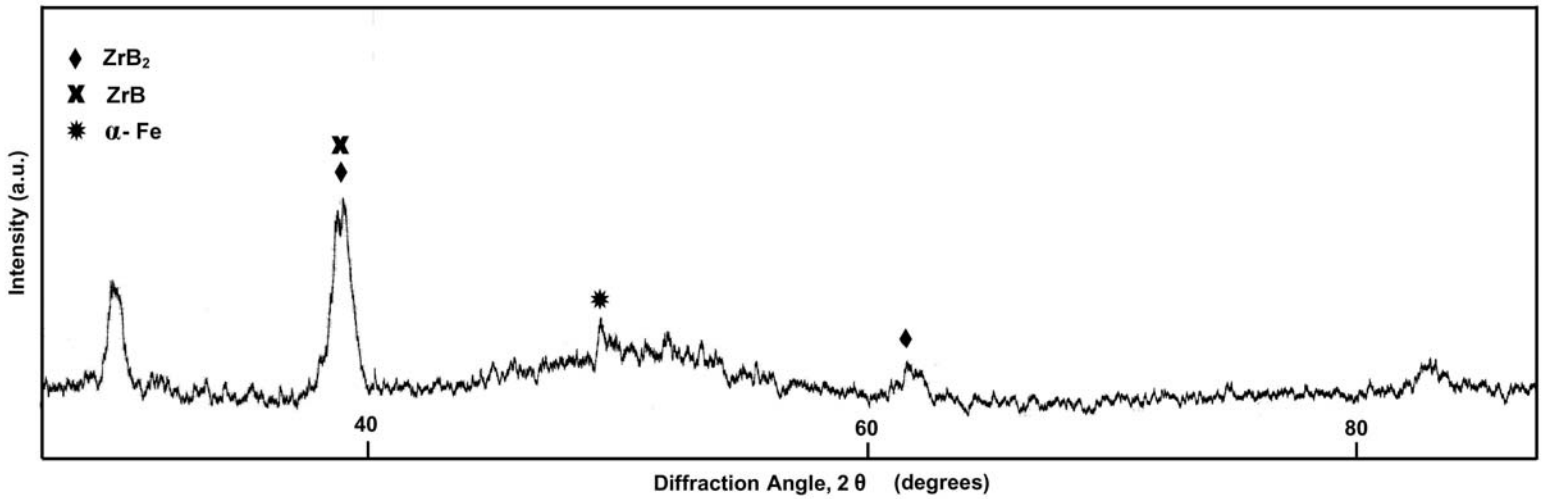

Figure 5.36 X-ray Diffraction pattern for C9 alloy.

5.3.6 C10 $Fe_{62}B_{21}Mo_5W_2Zr_6$ alloy

This alloy is same with C9 in terms of nominal composition, however due to reactions which occurred in previous experiments, two changes were made during casting. Firstly, the crucible used was changed and the Manfredi Y15 PT silica based crucible was used instead of an alumina based one, in order to avoid Zr being oxidized. Casting temperature of the quinary alloy C10 is 1380 ^{0}C and the heating rate was high in order to inhibit any reaction and excessive slag formation which can trigger compositional shifts. The alloy produced has an amorphous structure with some inevitably formed quenched in nuclei. Glass transition and crystallization behavior is revealed by the DSC curve given in Fig. 5.37. T_g of the alloy was found as 629 ^{0}C. The alloy shows a very distinct crystallization behavior. The onset of crystallization is 680 ^{0}C. According to the number of exothermic peaks, the crystallization is rather complex and occurs in five stages. The liquidus temperature of the alloy is 1112 ^{0}C. However, there are three endothermic melting peaks. This behavior indicates a sequential eutectic peritectic melting. From the thermal data obtained from the DSC curve T_{rg} was found to be 0.57 while ΔT_x was 51 ^{0}C.

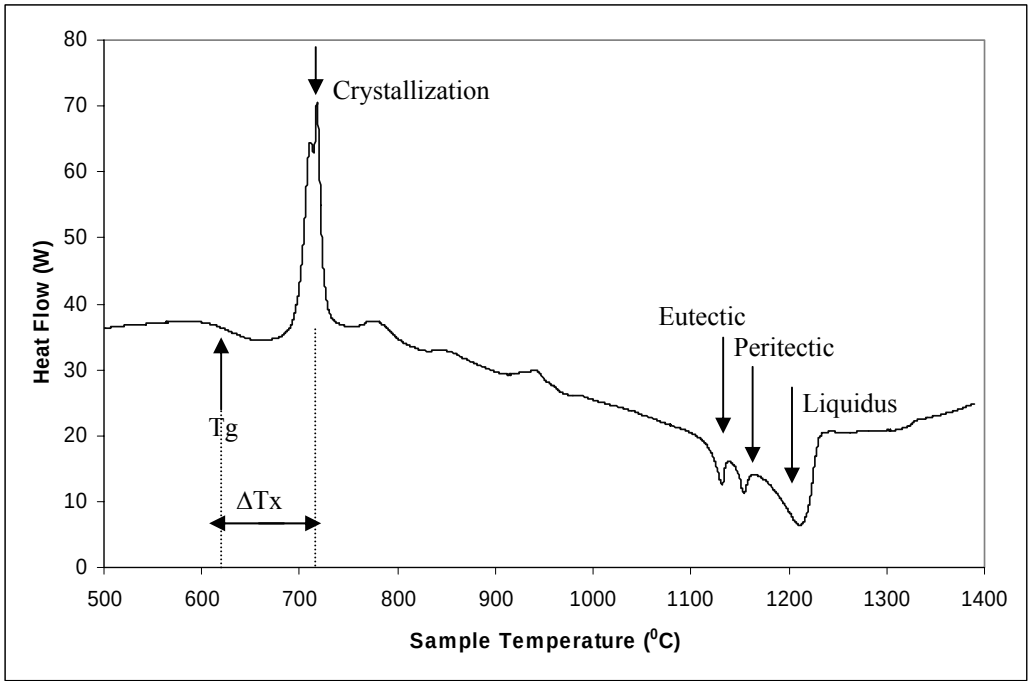

Figure 5.37 DSC curve of C10 alloy with a scanning rate 20 ^{0}C/min.

Table 5.14 Thermal data about C10 alloy.

T_g	T_x	T_e	T_p	T_L	ΔHx	ΔHe	ΔHp
629 ^{0}C	680 ^{0}C	1108 ^{0}C	1138 ^{0}C	1164 ^{0}C	-65.87 (J/mol)	4.6544 (J/mol)	6.626 (J/mol)

Microstructural examination of the specimens showed that at the thin regions of the alloy where cooling rate is high the amorphous matrix was formed. Small crystals embedded in the matrix were α-Fe crystallites. At the thickest region of the wedge, crystalline structure was seen. General composition of the alloy was compared with the nominal composition to check the efficiency of casting. The nominal and actual compositions were the same within the error limit of EDS analyses. The SEM photographs taken are given in Fig. 5.38. The crystalline phases present were a primary faceted phase and eutectic phase mixture.

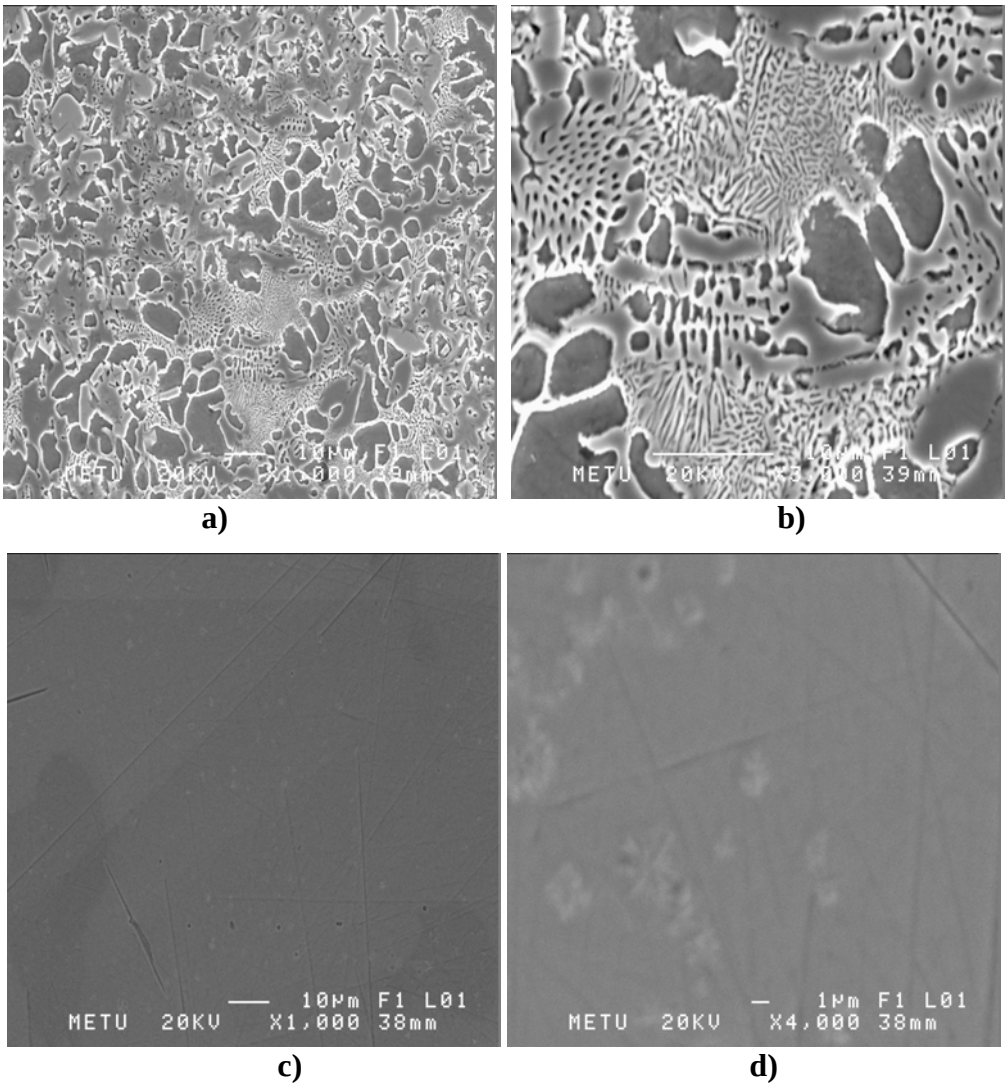

Figure 5.38 Secondary electron images of C10 alloy a) and b) are taken from thick section while c) and d) are taken from thin sections.

From the x-ray pattern given in Fig. 5.39, a broad peak was observed for thin regions, which verifies the DSC results. Some crystalline peaks were also identified. The presence of some crystalline phase was also seen from the SEM observations, the size and percentage of the crystalline phases increase as the cooling rate decreases.

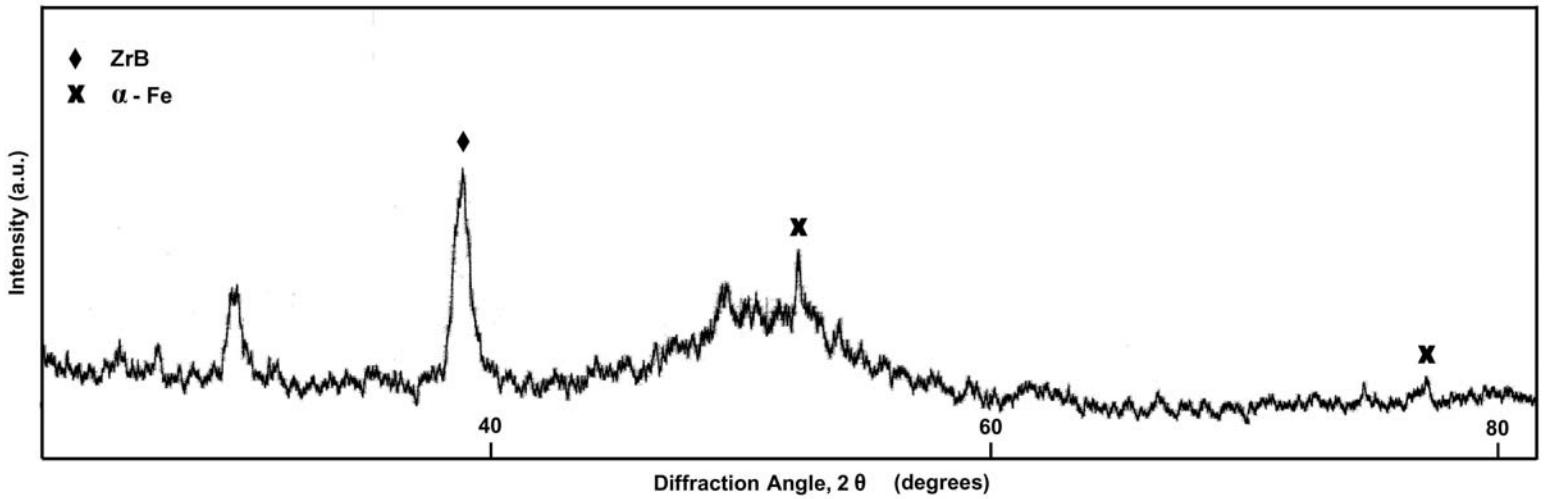

Figure 5.39 X-ray Diffraction pattern for C10 alloy.

From the results obtained it can be suggested that glass forming ability is increased drastically when the solidification involves a peritectic eutectic reaction sequence. One of the phases being intermetallic, which showed faceted growth morphology in primary growth and forming irregular eutectics with the other phase, also believed to enhance the GFA of the system.

When the fracture surfaces were investigated by naked eye, a shiny appearance was observed. The fracture surface of the alloy was also examined by the help of SEM. SEM photographs are given in Fig. 5.40. For crystalline materials, fracture surfaces had two main characteristic appearances, either ductile fracture or brittle fracture. Ductile fracture surfaces were rough and irregular and the surface usually contained many micro voids and dimples. On the other hand brittle fracture surfaces were usually recognized by the cleavage planes. The fracture surface for C10 alloy was bright and it did not show the characteristics of either brittle nor ductile fracture. It showed the characteristic amorphous fracture surface with a featureless matrix. No grain boundary was observed. However, there were small shallow spots on the surface which has approximately 800 nm size on average. These spots were probably formed due to crystalline phase α-Fe sticking to the other side of the fracture surface or falling apart.

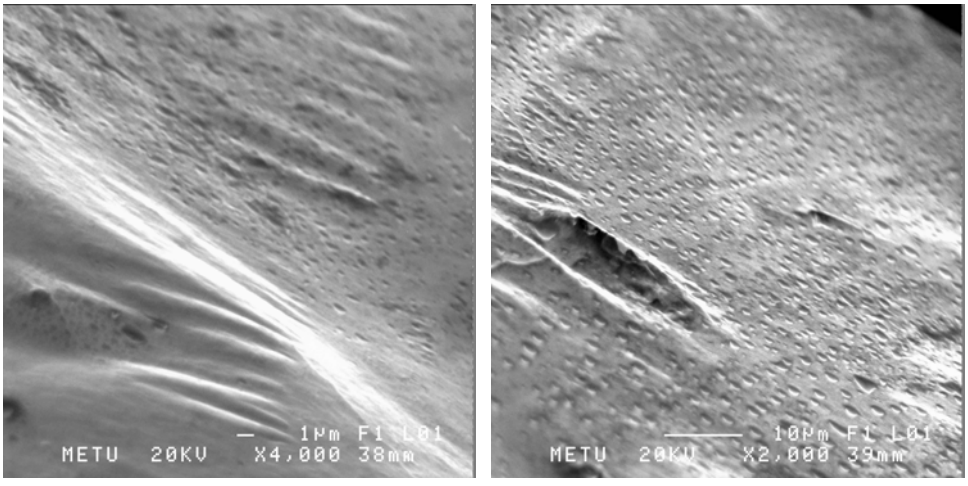

Figure 5.40 Secondary electron fracture surface images of C10 alloy

CHAPTER VI

CONCLUSIONS

Conclusions drawn from the study can be summarized as follows:

1. For the Zn-Mg system, the ordering energy between the atoms are increased when Ag, Au, Ba, Ca, Hg, Cs, K, La, Li, Na, Rb, Sr and Y elements are used as alloying additions in place of Mg. While Cd, Cu, Hg, In, Sc, Tl, Ag, Au, Ba, Ca, Hg, Cs, K, La, Li, Na, Rb, Sr, Y are the elements which increase the ordering energy when used as alloying additions in place of Zn. For Zn-Mg system especially 1A and 2A metals increase the GFA of the alloy and are potential alloying candidates for designing new bulk glass forming systems.

2. For the Fe-B system, the ordering energy between the atoms are increased when C, Mo, Re, Tc, V and W elements are used as alloying additions.

3. MD program developed can be used to investigate GFA and structure of amorphous alloys. However, the interatomic potentials are crucial for the results of simulation studies. Correct interpolation of interatomic potential data is crucial for attaining analytical forms of potentials.

4. Centrifugal Casting process can be successfully used for producing bulk amorphous alloys.

5. Silica based vessels are essential for melting when alloys containing highly reactive elements such as Zr are being used.

6. Alloying addition of Zr to Fe-B system enhances the GFA significantly.

7. $Fe_{62}B_{21}Mo_5W_2Zr_6$ alloy can be vitrified in bulk forms and the BGFA related with this alloy is due to complex solidification behavior, with the presence of sequential peritectic and eutectic reactions upon cooling. The formation of amorphous phase is attained when the growth of faceted intermetallic and irregular eutectic is suppressed due to high cooling rate.

REFERENCES

1. F.E. Luborsky in ‘‘Amorphous Metallic Alloys’’, Edited by F.E. Luborsky, Butterworths Monographs in Materials, 1983.
2. N. Mattern, U. Kühn, H. Hermann, H. Ehrenberg, J. Neuefeind, J. Eckert, Acta Materialia, 50 (2002) 305–314.
3. J. Kramer, Z. Phys., 106 (1937) 675.
4. A. Brenner, D. E.Couch and E. K. Williams, J. Res. Natn. Bur. Stand., 44 (1950) 109.
5. P. Duwez, Trans. Am. Soc. Metals, 60 (1967) 607.
6. I. S. Miroshienko and I. V. Salli, Ind. Lab. 25 (1959) 1463 in English; Zav. Lab., 25 (1959) 1398.
7. R. (Jr.) Pond, and R. Maddin, TMS-AIME, 245 (1969) 2475
8. HS. Chen, D. Turnbull, Acta Metall 17 (1969) 1021-1031.
9. F. Jörg Löffer, Intermetallics, 11 (2003) 529-540.
10. HS. Chen, Acta Metall 22 (1974) 1505-1511.
11. B.X. Liu, W.S. Lai, Q. Zhang, Materials Science and Engineering, 29 (2000) 1-48.
12. H.W. Kui, A.L. Greer, D. Turnbull, Applied Physics Letters, 45 (1984) 615-616.
13. A. Inoue, T. Zhang, T. Masumoto, T. Mater Trans JIM 30(1989) 956-972.
14. A. Inoue, A. Karo, T. Zhang, S.G. Kim, T. Masumoto, T. Mater Trans JIM 32(1991) 609-616.
15. T. Zhang, A. Inoue, T. Masumoto, Trans JIM 32(1991) 1005-1010.
16. A. Peker, W.L. Johnson, Applied Physics Letters 63 (1993) 2342-2344.
17. A. Inoue, A. Takeuchi, Materials Transaction, 43 (2002) 1982-1906.
18. J. Saida, M. Matsushita, A. Inoue, Intermetallics 10 (2002) 1089-1098.
19. A. Inoue, Acta Materialia 48 (2000) 279-306.
20. M. Telford, Materials Today, 36 (2004) 36-42.

21. S. J. Pang, T. Zhang, K. Asami, A. Inoue, Acta Materialia 50 (2002) 489-497.
22. S. Linderoth, Proceedings of the 22nd Risø International Symposium on Materials Science: Science of Metastable and Nanocrystalline Alloys, Structure, Properties, and Modelling, Edited by A.R. Dinsen, M. Eldrup, D. Juul Jensen, S. Linderoth, T.B. Pedersen, N.H: Pryds, A. Schroder Pdersen, J. A. Werth, (2001) 69-88.
23. A. Inoue, Bulk Amorphous Alloys Preparation and Fundamental Characteristics, Trans. Tech Publications, 1998.
24. A. Inoue, Acta Materialia 48 (2000) 279-306.
25. J. Daniel Sordelet, Elena Rozhkova, Matthew F. Besser, Matthew J. Kramer. Journal of Non-Crystalline Solids 317 (2003) 137-143.
26. M. H. Lee, D.H. Bae, W.T. Kim, D.H. Kim, E. Rozhkova, P.B. Wheelock, D.J. Sordelet, Journal of Non-Crystalline Solids 315 (2003) 89-96.
27. Z. P. Lu, H. Tan, Y. Li, S.C. Ng, Scripta Materialia 42 (2000) 667-673.
28. Z. P. Lu, H. Tan, Y Li, S.C. Ng, Journal of Non-Crystalline Solids 270 (2000) 103-114.
29. H.A Davies in "Amorphous Metallic Alloys" Edited by F.E. Luborsky, Butterworths Monographs in Materials, 1983.
30. P. Duwez, Transactions of the ASM 60 (1967) 603-633.
31. Z.P. Lu, Y. Li, S.C. Ng, Journal of Non-Crystalline Solids 270 (2000) 103-114.
32. G. Shao, Intermetallics 11 (2003) 313-324.
33. D. Turnbull, Contemp. Physc., 10 (1969) 473.
34. W. H. Wang, C. Dong, C. H. Shek, Material Science and Engineering R, 44 (2004) 45-89.
35. O.N. Senkov, J.M. Scott, Scripta Materiala, 50 (2004) 449–452.
36. O.N. Senkov, D.B. Miracle, Materials Research Bulletin, 36 (2001) 2183-2198.

37. Z.P. Lu, C.T. Liu, Acta Materialia 50 (2002) 3501-3512.
38. M. V. Akdeniz, Amdulla O. Mekhrabov, M. K. Pehlivanoğlu, Journal of Alloys and Compounds, 386 (2005) 185-191.
39. J. L. Finney in "Amorphous Metallic Alloys" Edited by F. E. Lubrosky, 1984 42-57.
40. Bernal, J. D., Nature, 188,910 (1960)
41. K. Suzuki, in "Amorphous Metallic Alloys", Edited. F. E. Luborsky, 1984, 74-100.
42. L. Wang, H. Cong, Y. Zhang, X. Bion, Physica B, 335 (2005) 140-146.
43. A. Inoue, A.R. Yavari, Mater. Trans. JIM 39 (1998) 318.
44. E. G. Noya, C. Rey and L. J. Gallego, Journal of Non-Crystalline Solids, 298 (2002) 60-66.
45. L. Wang, Y. Zhang, H. Yang and Y Chen, Physics Letters A, 317 (2003) 489-494.
46. L. Qi, H. F. Zhang, Z. Q. Hu and P. K. Liaw, Physics Letters A, 327 (2004) 506-511.
47. H.H. Kart, M. Uludoğan, T. Çağın and M. Tomak, Journal of Non-Crystalline Solids, 342 (2004) 6-11.
48. V. Heine, M. L. Cohen, D. Weaine, Solid State Physics, vol. 24 Edited by H. Ehrenreich et al., Academic Press, New York, 1970.
49. A. O. Mekhrabov and M. V. Akdeniz, Metallurgical and Materials Transactions A, 34A (2003) 721.
50. A. O. Mekhrabov. and M. V. Akdeniz, Chemical Eng. Comm., 190 (2003) 898.
51. A. O. Mekhrabov and M. V. Akdeniz., Acta Materialia, 47-7 (1999) 2067.
52. A. O. Mekhrabov, M. V. Akdeniz and M. M. Arer, Acta Materialia, 45-3 (1997) 1077.
53. M. V. Akdeniz, A. O. Mekhrabov, Acta Materialia, 46- 4 (1998) 1185.
54. Robert E. Stephenson, Computer Simulation for Engineers, Harcourt Brace Jovanovich 1971.

55. M.P. Allen, D.J. Tildesley, Computer Simulation of Liquids, Clarendon Press, 1989.
56. D. Frenkel, B. Smit, Understanding molecular simulation: from algorithms to applications, San Diego : Academic Press, 1996.
57. A. A. Selezenev, A. Yu. Aleynikov, N. S. Gantchuk, P. V. Yermakov, J. K.Labanowski, A. A. Korkin, Computational Materials Science 28 (2003)107 –124.
58. F. Shimojo , T. J. Campbell, R. K. Kalia, A. Nakano, P. Vashishta, S. Ogata, K. Tsuruta, Future Generation Computer Systems 17 (2000) 279–291.
59. J. M. Haile, Molecular Dynamics Simulation Elementary Methods, A Wiley-Interscience Publication, 1997.
60. J. A. McCammon, B. R. Gelin, M. Karplus, Nature (Lond.) 267 (1977) 585.
61. D. C. Raparot, The Art of Molecular Dynamics Simulation, Cambridge University Press, 1995.
62. H. Gould, J. Tobochnik, An Introduction to Computer Simulation Methods: Applications to Physical System. Jon Wiley and Sons, 2003.
63. I. M. Sobol, Y. L. Levitan, Computers and Mathematics with Applications 37 (1999) 33-40.
64. P. Gerald, Jr. Dwyer, K.B. Williams, Journal of Economic Dynamics & Control 27 (2003) 645–650.
65. N. Cowlam, Journal of Non-Crystalline Solids, 205-207, (1996) 567.
66. Ş. Erkoç, Lecture Notes On Simulation of Many Particle Systems.
67. O. N. Senkov, J. M. Scott, Materials Letters, 58, 7-8 (2004) 1375-1378.
68. H. Men, Z. Q. Hu, J. Xu, Scripta Materialia, 46 10 (2002) 699-703.
69. N. Mingolo, Thermochimica Acta 302 (1997) 41-46.
70. M.V. Akdeniz, J. V. Wood, Journal of Material Science 31 (1996) 545-550.

71. M. Plumbo, G. Cacciamani, E. Bosco, M. Baricco, Intermetallics 11 (2003) 1293-1299.
72. S. Banerjee, R.T. Savalia, G.K. Dey, Material Science and Engineering A304-306 (2001) 26-33.
73. F. Kurtz, Fundamentals of Solidification, Trans Tech Publications, 1992.
74. W.B. Pearson, A Handbook of Lattice Spacings and Structures of Metals and Alloys, Pergamon Press, 1967.
75. W. J. Yao, X.J. Han, B. Wei, Journal of Alloy and Compunds 348 (2003) 88-99.
76. H. Tan, Y. Zhang, D. Ma, Y.P. Feng, Y. Li, Acta Materialia 51 (2003) 4551-456.
77. S. Gürbüz, Synthesis and Characterization of Iron-Based Alloy Systems, METU M.s Thesis, 2004.
78. B. Livio, A. Carlo, B. Marcell, Journal of Alloys and Compounds 247 (1997) 164-171.
79. K. Pehlivanoğlu, Production and Development of Bulk Metallic Glasses, METU PhD. Thesis, 2003.

APPENDIX

A. MOLECULAR DYNAMICS CODE

```
PROGRAM MOLDYN
IMPLICIT NONE
INTEGER:: N
COMMON N
INTEGER:: I,J,T, TQ, NTIME1, NTIME2 !loop counter during integration
COMMON I,J
DOUBLE PRECISION:: TS, PE, TEMP_K, G, KE, M, A, KB, M_FE, M_B, KE1,V, VIR, P, K,
PSET, SCALE
COMMON TS, PE,TEMP_K
DOUBLE PRECISION, DIMENSION(864):: VX, VY, VZ ! velocity arrays
DOUBLE PRECISION, DIMENSION(864):: X, Y, Z    ! position arrays
COMMON X,Y,Z
COMMON VX, VY, VZ
DOUBLE PRECISION, DIMENSION(864):: AX, AY, AZ ! accelaration arrays
DOUBLE PRECISION:: L_,W_,D_ !Length Width and Depth of the simulation box to be used
DOUBLE PRECISION:: RESCALER, V_S
CHARACTER (LEN=2):: ID         ! identity of the atom
COMMON ID
DOUBLE PRECISION:: TMON    ! Temperature monitored

! parameters are initialized
N = 864                    ! number of particles to be used in the simulation
KE1 = 0                    ! initial kinetic energy
KE  = 0                    ! kinetic energy
V_S = 0                    ! initial unscaled kinetic energy
TEMP_K = 800.0D0           ! Temperature in Kelvin

!integration parameters
TS  = 1.5D-15              ! length of time step in seconds
NTIME1 = 10000             ! number of time steps to be used in equilibration
NTIME2 = 200000            ! number of steps to be use in the quenching phase
SCALE = 8000               ! number of scale steps
KB = 1.380658D-23          !Boltzmann constant in joule per Kelvin
M_FE = 55.85/6.023D26      !mass of the IRON in kg
M_B = 10.81/6.023D26       !mass of the B in kg
M = 55.85/6.023D26         !mass of iron in kg
PSET = 131325.0
A = 3.4300D-10             ! Lattice parameter of Fe3B


OPEN (9, FILE = 'POSITION.OUT')
OPEN (10, FILE = 'VELOCITY.OUT')
OPEN (8, FILE = 'KINETIC_ENERGY.OUT')
```

```
OPEN (88,FILE ='TEMPERATURE.OUT')
OPEN (77, FILE ='ACCELERATION.OUT')
OPEN (99, file = 'PE.OUT')
OPEN (100, FILE ='TOTE.OUT')
OPEN (4,FILE='PRESSURE.OUT')


!Velocity Verlet algorithm for the numerical integration of particles
CALL INITIAL_VELOCITIES(N,TEMP_K,VX,VY,VZ, KB, M, M_FE, M_B)
!Calculation of initial kinetic energy
DO I=1,N
        CALL KIND_DETERMINATION(I,M,M_FE,M_B,ID)
        KE1 = KE1 + 0.5 * M * (VX(I)**2 + VY(I)**2 + VZ(I)**2)
END DO
WRITE(*,*) 'Initial kinetic energy of the system is',KE1
CALL FCC(A,K)
!CALL BCC(A,K)
!CALL SC(A,K)
L_= A*(N/K)**(1.0/3.0)
W_= A*(N/K)**(1.0/3.0)
D_= A*(N/K)**(1.0/3.0)

OPEN(55,FILE="FCC.TXT",FORM="FORMATTED",STATUS="OLD")
DO I=1,N
        READ(55,20) X(I), Y(I), Z(I)
        20 FORMAT(4X,F20.17,4X,F20.17,4X,F20.17)
END DO

T =1 ! initial time for the determination of initial forces
CALL FORCE(N,X,Y,Z,T,A,AX,AY,AZ,M,M_FE,M_B,TEMP_K,PE,VIR,L_,W_,D_)
WRITE(*,*) 'Initial potential energy of the system is', PE
P = (N*KB*TEMP_K)/(L_*W_*D_) + VIR/(3*L_*W_*D_)

DO T=1,NTIME1
        KE = 0; V_S = 0
        IF (MOD(T,100) == 0) THEN
        WRITE (9,*) T; WRITE (10,*) T
        END IF
        DO I=1,N
                CALL KIND_DETERMINATION(I,M,M_FE,M_B,ID)
                X(I) = X(I) + VX(I)*TS + AX(I)*(TS**2)/2.0          ! new positions
                IF (X(I) .LT. 0.0D0) X(I) = X(I) + L_               ! PBC
                IF (X(I) .GT. L_) X(I) = X(I) - L_
                Y(I) = Y(I) + VY(I)*TS + AY(I)*(TS**2)/2.0
                IF (Y(I) .LT. 0.0D0) Y(I) = Y(I) + W_
                IF (Y(I) .GT. W_) Y(I) = Y(I) - W_
                Z(I) = Z(I) + VZ(I)*TS + AZ(I)*(TS**2)/2.0
                IF (Z(I) .LT. 0.0D0) Z(I) = Z(I) + D_
                IF (Z(I) .GT. D_) Z(I) = Z(I) - D_
                VX(I) = VX(I)+ 0.5*AX(I)*TS
                VY(I) = VY(I)+ 0.5*AY(I)*TS
                VZ(I) = VZ(I)+ 0.5*AZ(I)*TS
```

```
                IF (MOD(T,100) == 0) THEN
                        WRITE(9,*) ID, X(I), Y(I), Z(I)
                END IF
        END DO
        CALL FORCE(N,X,Y,Z,T,A,AX,AY,AZ,M,M_FE,M_B,TEMP_K,PE,VIR,L_,W_,D_)
        P = (N*KB*TEMP_K)/(L_*W_*D_) + VIR/(3*L_*W_*D_)
        WRITE(4,*) P
        IF (MOD(T,100) == 0) THEN
                WRITE(77,*) AX,AY,AZ
                WRITE (*,*) 'potential energy =', PE
        END IF
        DO I=1,N
                CALL KIND_DETERMINATION(I,M,M_FE,M_B,ID)
                VX(I) = VX(I) + (TS/2.0D0)*(AX(I))          ! new velocities
                VY(I) = VY(I) + (TS/2.0D0)*(AY(I))
                VZ(I) = VZ(I) + (TS/2.0D0)*(AZ(I))
                KE = KE + 0.5  * M *(VX(I)**2 + VY(I)**2 + VZ(I)**2)
        END DO
                IF (T<SCALE) THEN
                IF(MOD(T,10) == 1) THEN

        RESCALER=SQRT(3*REAL(N)*KB*TEMP_K)/DSQRT(2.0D0*KE)
                        KE= 0
                        DO I=1,N
                                CALL KIND_DETERMINATION(I,M,M_FE,M_B,ID)
                                VX(I) = VX(I) * RESCALER
                                VY(I) = VY(I) * RESCALER
                                VZ(I) = VZ(I) * RESCALER
                                KE = KE + 0.5*M*(VX(I)**2+VY(I)**2+VZ(I)**2)
                        END DO
                END IF
                END IF
        IF (MOD(T,100) == 0) THEN
                CALL ORDER(X,Y,Z,A,N,T)
                IF (MOD(T,5000) == 0) THEN
                CALL RDF(N,X,Y,Z,L_,W_,D_,A,T)
                END IF
        END IF
        WRITE(99,*) PE
        TMON = 2*KE/((3*REAL(N)-4)*KB)
        WRITE(8,*) KE
        WRITE(88,*) TMON
        WRITE(100,*) KE+PE
END DO

! end of equilibration phase !
! quenching phase begins!
WRITE(9,*) 'Quenching phase begins'
WRITE(10,*) 'Quenching phase begins'
DO TQ=1,20
        !TEMP_K= TEMP_K-60
        TEMP_K= TEMP_K+50
        DO T=(NTIME1+1)+(TQ-1)*10000, (NTIME1+1)+(TQ)*(NTIME2/20)
        KE = 0; V_S = 0
```

```
IF (MOD(T,100) == 0) THEN
WRITE (9,*) T; WRITE (10,*) T
END IF
DO I=1,N
        CALL KIND_DETERMINATION(I,M,M_FE,M_B,ID)
        X(I) = X(I) + VX(I)*TS + AX(I)*(TS**2)/2.0
        IF (X(I) .LT. 0.0D0) X(I) = X(I) + L_
        IF (X(I) .GT. L_) X(I) = X(I) - L_
        Y(I) = Y(I) + VY(I)*TS + AY(I)*(TS**2)/2.0
        IF (Y(I) .LT. 0.0D0) y(I) = y(i) + W_
        IF (Y(I) .GT. W_) Y(I) = Y(I) - W_
        Z(I) = Z(I) + VZ(I)*TS + AZ(I)*(TS**2)/2.0
        IF (Z(I) .LT. 0.0D0) Z(I) = Z(I) + D_
        IF (Z(I) .GT. D_) Z(I) = Z(I) - D_
        IF (MOD(T,100) == 0) THEN
                WRITE(9,*) ID, X(I), Y(I), Z(I)
        END IF

        VX(I) = VX(I)+ 0.5*AX(I)*TS
        VY(I) = VY(I)+ 0.5*AY(I)*TS
        VZ(I) = VZ(I)+ 0.5*AZ(I)*TS

END DO
CALL FORCE(N,X,Y,Z,T,A,AX,AY,AZ,M,M_FE,M_B,TEMP_K,PE,VIR,L_,W_,D_)
P = (N*KB*TEMP_K)/(L_*W_*D_) + VIR/(3*L_*W_*D_)
WRITE(4,*) P
IF (MOD(T,100) == 0) THEN
        WRITE(77,*) AX,AY,AZ
        WRITE (*,*) 'potential energy =', PE
END IF
DO I=1,N
        CALL KIND_DETERMINATION(I,M,M_FE,M_B,ID)
        VX(I) = VX(I) + (TS/2.0D0)*(AX(I))
        VY(I) = VY(I) + (TS/2.0D0)*(AY(I))
        VZ(I) = VZ(I) + (TS/2.0D0)*(AZ(I))
        KE = KE + 0.5  * M *(VX(I)**2 + VY(I)**2 + VZ(I)**2)
END DO
        IF (T<10000*tq+ SCALE) THEN
        IF (MOD(T,10) == 1) then

RESCALER=SQRT(3*REAL(N)*KB*TEMP_K)/DSQRT(2.0D0*KE)
                KE= 0
                DO I=1,N
                        CALL KIND_DETERMINATION(I,M,M_FE,M_B,ID)
                        VX(i) = VX(I) * RESCALER
                        VY(i) = VY(i) * RESCALER
                        VZ(i) = VZ(i) * RESCALER
                        KE = KE + 0.5*M*(VX(I)**2+VY(I)**2+VZ(I)**2)
                END DO
        END IF
        END IF
IF (MOD(T,100) == 0) THEN
        CALL ORDER(X,Y,Z,A,N,T)
        IF (MOD(T,5000) == 0) THEN
```

```
                CALL RDF(N,X,Y,Z,L_,W_,D_,A,T)
                END IF
        END IF
        WRITE(99,*) PE
        TMON = 2*KE/((3*REAL(N)-4)*KB)
        WRITE(8,*) KE
        WRITE(88,*) TMON
        WRITE(100,*) KE+PE
        END DO
END DO

CALL CPU_TIME(G)
OPEN (1,FILE = 'TIME.TXT')
WRITE(1,*) G
CLOSE (UNIT =8)
CLOSE (UNIT =9)
CLOSE (UNIT =10)
CLOSE (UNIT =88)
CLOSE (UNIT =77)
END


SUBROUTINE KIND_DETERMINATION(I,M,M_FE,M_B,ID)
INTEGER, INTENT(IN):: I
CHARACTER(LEN=2), INTENT(OUT):: ID
DOUBLE PRECISION, INTENT(IN):: M_FE, M_B
DOUBLE PRECISION, INTENT(OUT):: M
IF (MOD(I,4)==1) THEN
ID ='B'
ELSE
ID ='FE'
END IF
IF (ID=='FE') THEN
M = M_FE
ELSE
M=M_B
END IF
END SUBROUTINE KIND_DETERMINATION

SUBROUTINE INITIAL_VELOCITIES(N,TEMP_K,VX,VY,VZ, KB,M, M_FE, M_B)
INTEGER, INTENT(IN):: N
DOUBLE PRECISION, INTENT(IN)::  TEMP_K, KB,M,M_FE,M_B
DOUBLE PRECISION, DIMENSION(N), INTENT(OUT):: VX, VY, VZ
INTEGER:: I
DOUBLE PRECISION:: VXTOTAL, VYTOTAL, VZTOTAL, VXTOT2, VYTOT2, VZTOT2,
V_S, RESCALER1, RESCALER
CHARACTER(LEN=2):: ID

OPEN(11,FILE='INITIAL_VELOCITIES.OUT')
OPEN(66,FILE='RANDOM1.TXT')
OPEN(67,FILE='RANDOM2.TXT')
OPEN(68,FILE='RANDOM3.TXT')
VXTOTAL = 0; VYTOTAL = 0; VZTOTAL = 0
! random numbers generated by randor are read from text files
```

```
DO I=1,N
        READ(66,*) VX(I)
        VXTOTAL = VXTOTAL + VX(I)
        READ(67,*) VY(I)
        VYTOTAL = VYTOTAL+  VY(I)
        READ(68,*) VZ(I)
        VZTOTAL = VZTOTAL+  VZ(I)
END DO
VXTOT2 = VXTOTAL/REAL(N)
VYTOT2 = VYTOTAL/REAL(N)
VZTOT2 = VZTOTAL/REAL(N)
!Adjust the total momentum of the system to zero
DO I=1,N
        VX(I) = VX(I) - VXTOT2
        VY(I) = VY(I) - VYTOT2
        VZ(I) = VZ(I) - VZTOT2
END DO
V_S = 0
DO I=1,N
        CALL KIND_DETERMINATION(I,M,M_FE,M_B,ID)
        V_S= V_S + 0.5*M*(VX(I)**2+VY(I)**2+VZ(I)**2)
END DO
RESCALER1= (3*REAL(N)*KB*TEMP_K)/(2*V_S)
RESCALER = DSQRT(RESCALER1)
DO I=1,N
        CALL KIND_DETERMINATION(I,M,M_FE,M_B,ID)
        VX(I) = VX(I) * RESCALER  !kinetic energy of atoms are rescaled
        VY(I) = VY(I) * RESCALER
        VZ(I) = VZ(I) * RESCALER
        WRITE(11,*) ID,VX(I), VY(I), VZ(I)
END DO
CLOSE (UNIT = 11)
RETURN
END


SUBROUTINE FCC(A,K)
DOUBLE PRECISION, INTENT(IN):: A
DOUBLE PRECISION, DIMENSION(864):: X, Y, Z
DOUBLE PRECISION, DIMENSION(8):: X0, Y0, Z0
DOUBLE PRECISION, INTENT(OUT):: K
INTEGER:: IX, IY, IZ
K=4
OPEN (UNIT=55,FILE="FCC.TXT")

X0(1)=0.0
Y0(1)=0.0
Z0(1)=0.0
X0(2)=0.5*A
Y0(2)=0.5*A
Z0(2)=0.0
X0(3)=0.5*A
```

```
Y0(3)=0.0
Z0(3)=0.5*A
X0(4)=0.0
Y0(4)=0.5*A
Z0(4)=0.5*A
DO IX=0,5
  DO IY=0,5
    DO IZ=0,5
            DO I=1,4
            X(I)=IX*A+X0(I)
            Y(I)=IY*A+Y0(I)
            Z(I)=IZ*A+Z0(I)
            WRITE(55,10) X(I), Y(I), Z(I)
            10 FORMAT(4X,F20.17,4X,F20.17,4X,F20.17)
            END DO
    END DO
  END DO
END DO

CLOSE (55)
END SUBROUTINE FCC



SUBROUTINE BCC(A,K)
DOUBLE PRECISION, INTENT(IN):: A
DOUBLE PRECISION, DIMENSION(1500):: X, Y, Z
DOUBLE PRECISION, DIMENSION(2):: X0, Y0, Z0
DOUBLE PRECISION, INTENT(OUT):: K
INTEGER:: IX, IY, IZ
K=2
OPEN (UNIT=56,FILE="BCC.TXT")

X0(1)=0.0
Y0(1)=0.0
Z0(1)=0.0
X0(2)=0.5*A
Y0(2)=0.5*A
Z0(2)=0.5*A
DO IX=0,6
  DO IY=0,6
    DO IZ=0,6
            DO I=1,2
            X(I)=IX*A+X0(I)
            Y(I)=IY*A+Y0(I)
            Z(I)=IZ*A+Z0(I)
            WRITE(56,10) X(I), Y(I), Z(I)
            10 FORMAT(4X,F18.16,4X,F18.16,4X,F18.16)
            END DO
    END DO
  END DO
END DO

CLOSE (56)
```

```
END SUBROUTINE BCC


SUBROUTINE SC(A,K)
DOUBLE PRECISION, INTENT(IN):: A
DOUBLE PRECISION, DIMENSION(1500):: X,Y,Z
DOUBLE PRECISION :: X0, Y0, Z0
DOUBLE PRECISION, INTENT(OUT):: K
INTEGER:: IX, IY, IZ
K=1
OPEN (UNIT=57,FILE="SC.TXT")

X0 =0.0
Y0 =0.0
Z0 =0.0
DO IX=0,6
  DO IY=0,6
    DO IZ=0,6
            DO I=1,1
            X(I)=IX*A+X0
            Y(I)=IY*A+Y0
            Z(I)=IZ*A+Z0
            WRITE(57,10) X(I), Y(I), Z(I)
            10 FORMAT(4X,F18.16,4X,F18.16,4X,F18.16)
            END DO
    END DO
  END DO
END DO

CLOSE (57)
END SUBROUTINE SC


SUBROUTINE FORCE(N,X,Y,Z,T,A,AX,AY,AZ,M,M_FE,M_B,TEMP_K,PE,VIR, L_,W_,D_)
INTEGER:: I,J
INTEGER, INTENT(IN)::N,T
DOUBLE PRECISION:: RCUT
DOUBLE PRECISION:: DX,DY,DZ,DXX,DYY,DZZ, DIST, FXI,FYI,FZI, FIJ, FXIJ, FYIJ,
FZIJ, POT_FE3B, FORCE_FE3B, POT_FE,FORCE_FE,POT_B, FORCE_B
DOUBLE PRECISION, INTENT(IN)::A, M, M_FE, M_B
DOUBLE PRECISION, DIMENSION(864):: FX,FY,FZ
DOUBLE PRECISION, DIMENSION (864),INTENT(OUT):: AX,AY,AZ
DOUBLE PRECISION, INTENT(IN):: L_, W_, D_
DOUBLE PRECISION, DIMENSION(864), INTENT(IN):: X,Y,Z
INTEGER:: KIND1,KIND2
DOUBLE PRECISION, INTENT(IN):: TEMP_K
DOUBLE PRECISION, INTENT(OUT):: PE, VIR
DOUBLE PRECISION:: XI,YI,ZI, L2,W2,D2
CHARACTER(LEN=2):: ID
RCUT = 0.4 * L_
L2=L_/2.0
D2=D_/2.0
W2=W_/2.0
```

```
OPEN (7, file = 'FORCE.OUT')
PE = 0

VIR = 0

DO I= 1,N
        FX(I)=0; FY(I)=0; FZ(I)=0            ! initializing the force arrays
END DO
DO I=1,N-1
        CALL KIND_DETERMINATION(I,M,M_FE,M_B,ID)
        IF (ID=='FE')   KIND1 = 1
        IF (ID=='B') KIND1  = 2
        XI = X(I); YI = Y(I); ZI = Z(I)
        DO J=I+1,N
                CALL KIND_DETERMINATION(J,M,M_FE,M_B,ID)
                IF (ID=='FE') KIND2 = 1
                IF (ID=='B') KIND2  = 2
                DX = XI - X(J)
                DY = YI - Y(J)
                DZ = ZI - Z(J)
                DXX = DABS(DX)
                DYY = DABS(DY)
                DZZ = DABS(DZ)

    IF(DXX.GT.L2) DX = (DXX- L_) * SIGN(1.0,DX)        !minimum image convention
                IF(DYY.GT.W2) DY = (DYY- W_) * SIGN(1.0,DY)
                IF(DZZ.GT.D2) DZ = (DZZ- D_) * SIGN(1.0,DZ)
                DIST = DSQRT(DX**2 + DY**2 + DZ**2)
                IF(KIND1==1 .AND. KIND2== 1) THEN   ! interaction is between fe-fe
                        IF (DIST .LT. RCUT) THEN
                                FIJ = FORCE_FE(DIST)
                                VIR  = VIR + FIJ*DIST
                                FXIJ = FIJ*DX/DIST
                                FYIJ = FIJ*DY/DIST
                                FZIJ = FIJ*DZ/DIST
                                PE = PE + POT_FE(DIST)

                                FX(I) = FX(I) + FXIJ
                                FY(I) = FY(I) + FYIJ
                                FZ(I) = FZ(I) + FZIJ
                                FX(J) = FX(J) - FXIJ
                                FY(J) = FY(J) - FYIJ
                                FZ(J) = FZ(J) - FZIJ
                        END IF
                END IF
                IF (KIND1==1 .AND. KIND2== 2)  THEN !interaction is between fe-b
                        IF (DIST .LT. RCUT) THEN
                                FIJ = force_fe3b(dist)
                                VIR  = VIR + FIJ*DIST
                                FXIJ = FIJ*(DX/DIST)
                                FYIJ = FIJ*(DY/DIST)
                                FZIJ = FIJ*(DZ/DIST)
                                PE = PE + POT_FE3B(DIST)
```

```
                                FX(i) = FX(I) + FXIJ
                                FY(i) = FY(I) + FYIJ
                                FZ(i) = FZ(I) + FZIJ
                                FX(j) = FX(J) - FXIJ
                                FY(j) = FY(J) - FYIJ
                                FZ(j) = FZ(J) - FZIJ
                        END IF
                END IF
                IF (KIND1==2 .AND. KIND2== 1)  THEN !interaction is between fe-b
                        IF (DIST .LT. RCUT) THEN
                                FIJ = FORCE_FE3B(DIST)
                                VIR  = VIR + FIJ*DIST
                                FXIJ = FIJ*(DX/DIST)
                                FYIJ = FIJ*(DY/DIST)
                                FZIJ = FIJ*(DZ/DIST)
                                PE = PE + POT_FE3B(DIST)

                                FX(I) = FX(I) + FXIJ
                                FY(I) = FY(I) + FYIJ
                                FZ(I) = FZ(I) + FZIJ
                                FX(J) = FX(J) - FXIJ
                                FY(J) = FY(J) - FYIJ
                                FY(J) = FY(J) - FZIJ
                        END IF
                END IF
                IF (KIND1==2 .AND. KIND2== 2)  then     !interaction is between b-b
                        IF (DIST .LT. RCUT) THEN
                                FIJ = FORCE_B(dist)
                                VIR  = VIR + FIJ*DIST
                                FXIJ = FIJ*(DX/DIST)
                                FYIJ = FIJ*(DY/DIST)
                                FZIJ = FIJ*(DZ/DIST)
                                PE = PE + POT_B(DIST)
                                FX(I) = FX(I) + FXIJ
                                FY(I) = FY(I) + FYIJ
                                FZ(I) = FZ(I) + FZIJ
                                FX(J) = FX(J) - FXIJ
                                FY(J) = FY(J) - FYIJ
                                FZ(J) = FZ(J) - FZIJ
                        END IF
                END IF
        END DO
END DO
DO I=1,N
CALL KIND_DETERMINATION(I,M,M_FE,M_B,ID)
AX(I) = FX(I)/M
AY(I) = FY(I)/M
AZ(I) = FZ(I)/M
END DO
CLOSE (UNIT=6)
CLOSE (UNIT=7)
RETURN
END
```

```
SUBROUTINE ORDER(X,Y,Z,A,N,T)
! This routine is intended to calculate Verlet's translational order
! parameter. For solids it is of order of unity whereas for liquids
! it oscillates around zero
DOUBLE PRECISION, DIMENSION(1001), INTENT(IN):: X, Y, Z
DOUBLE PRECISION:: LX,LY,LZ, ORD
DOUBLE PRECISION, INTENT(IN):: A
INTEGER, INTENT(IN):: N,T
DOUBLE PRECISION, PARAMETER:: PI=3.14159265358979

OPEN(699, FILE='ORDER.OUT')
LX=0; LY=0; LZ=0

DO I= 1, N
        LX = LX + DCOS(4*PI*X(I)/A)
        LY = LY + DCOS(4*PI*Y(I)/A)
        LZ = LZ + DCOS(4*PI*Z(I)/A)
END DO

ORD = (1.0D0/(3.0D0*N))*(LX+LY+LZ)
WRITE(699,*) ORD
END SUBROUTINE


SUBROUTINE RDF(N,X,Y,Z,L_,W_,D_,A,T)
INTEGER:: MN, L, I
INTEGER, DIMENSION(30):: BIN
INTEGER, INTENT(IN):: N,T
DOUBLE PRECISION , INTENT(IN)::L_,W_,D_,A
DOUBLE PRECISION:: DR,RO,DIS, K, XIT, YIT, ZIT
DOUBLE PRECISION, DIMENSION(30):: RADIAL
DOUBLE PRECISION, DIMENSION(864), INTENT(IN):: X,Y,Z
DOUBLE PRECISION, PARAMETER:: PI=3.14159265358979

! the central atom is determined
DIS=0; K=1
RO=N/(L_*W_*D_)
MN= 30                                  ! number of radial bins
DR = L_/(2*MN); DR1 = 0; DR2 = DR       ! width of  M radial bins

DO I=1,N
        DIS = DSQRT( (X(I)-0.5D0*L_)**2 + (Y(I)-0.5D0*W_)**2 + (Z(I)-0.5D0*D_)**2 )
        IF (DIS<= K) THEN
                K = DIS
                J = I                   !index of the central atom
                XIT = X(I)
                YIT = Y(I)
                ZIT = Z(I)
        END IF
END DO
DO L=1,MN
BIN(L)=0
END DO
DO L=1,MN
```

```
        DR1 = (L-1)*DR
        DR2 = (L)*DR
        DO I=1,N
                DIST= DSQRT((XIT-X(I))**2+(YIT-Y(I))**2+(ZIT-Z(I))**2)
                IF ((DR1 < DIST) .AND. (DIST <= DR2)) THEN
                BIN(L) = BIN(L) +1
                END IF
        END DO
END DO
DO L=1,MN
DR1 = (L-1)*DR
DR2 = (L)*DR
RADIAL(L)= BIN(L)/(RO*(4.0/3.0)*PI*(DR2**3-DR1**3))
END DO
OPEN (51,FILE = 'RADIAL.OUT')
WRITE (51,*) 'TIME STEP',T
DO l=1,MN
        WRITE (51,*) L*DR*1.0D10,RADIAL(L)
END DO

END SUBROUTINE RDF
```

B. BINARY PHASE DIAGRAMS FOR FE-MO, FE-W, FE-ZR, B-MO, B-W AND B-ZR SYSTEMS

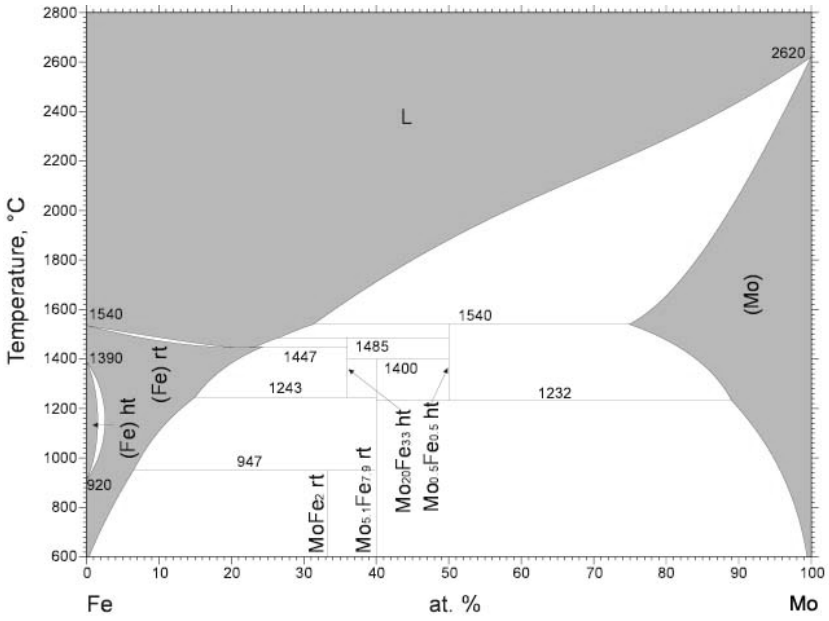

Figure A.1 Binary phase diagram for Fe-Mo system.

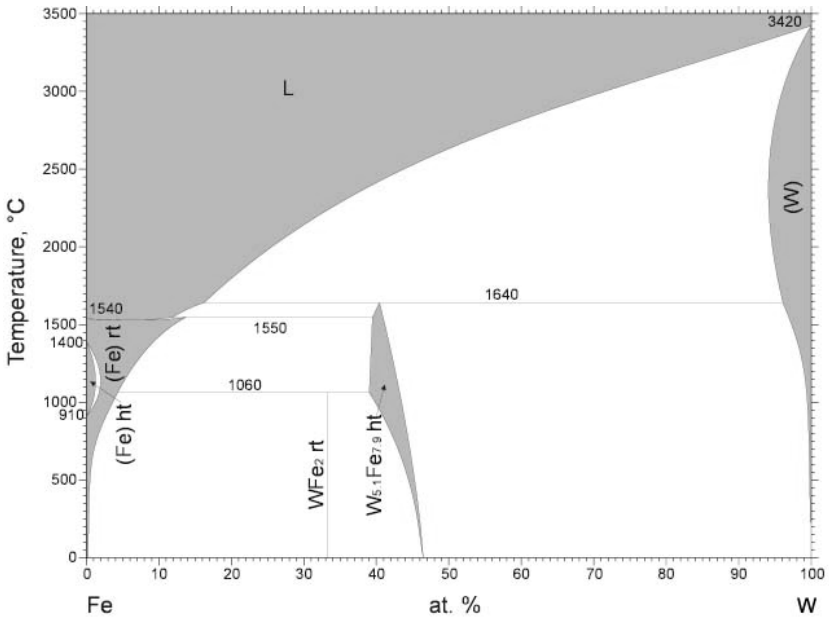

Figure A.2 Binary phase diagram for Fe-W system.

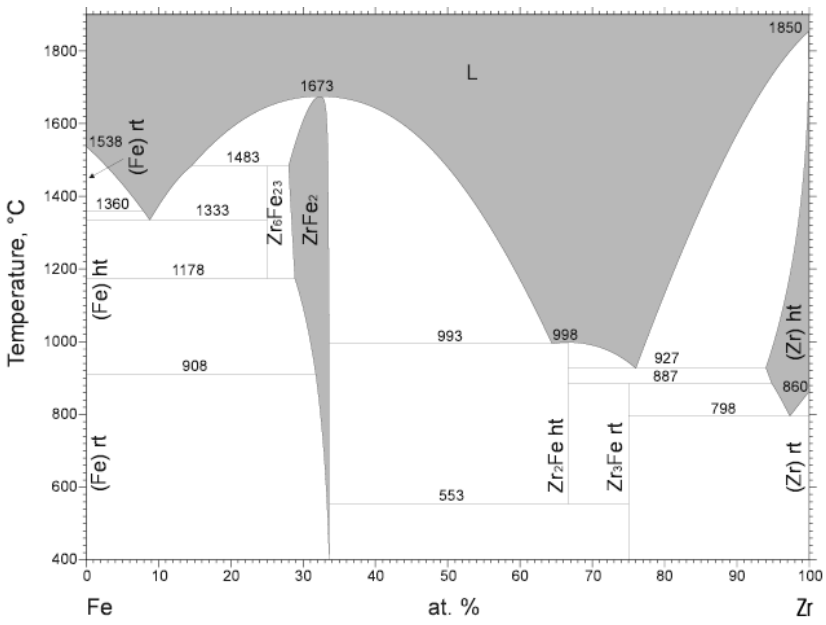

Figure A.3 Binary phase diagram for Fe-Zr system.

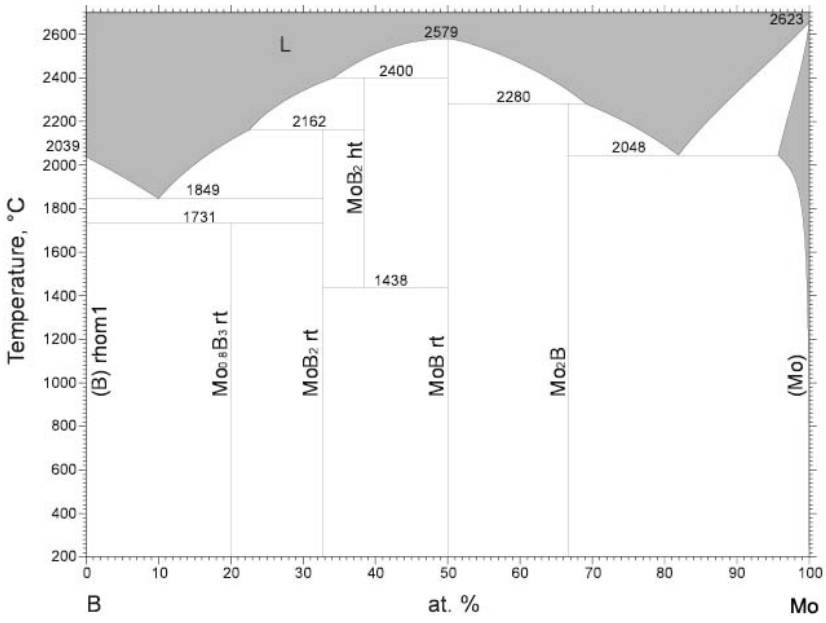

Figure A.4 Binary phase diagram for B-Mo system.

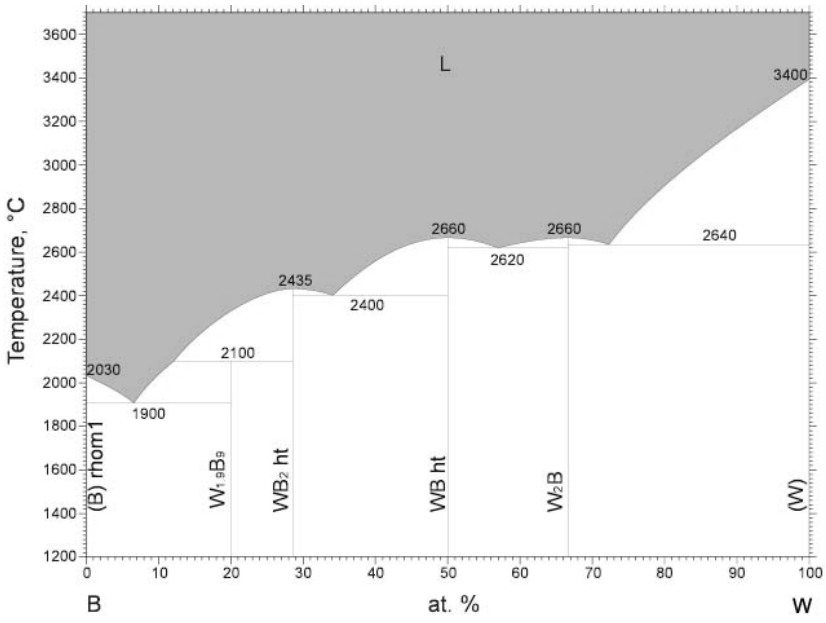

Figure A.5 Binary phase diagram for B-W system.

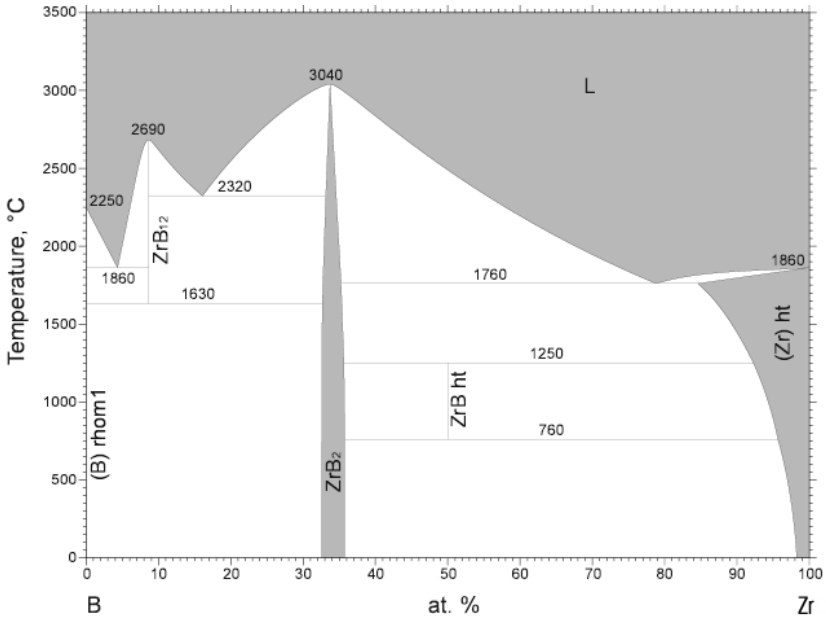

Figure A.6 Binary phase diagram for B-Zr system.